Fall 2023

Design and Fabrication of a Low Power 7.2 Terabit Transmitter for Exascale Computing

Scott McWilliams
Southern Methodist University, rubianlonestar@gmail.com

DESIGN AND FABRICATION OF A LOW POWER 7.2 TERABIT TRANMITTER FOR EXASCALE COMPUTING

Approved by:

_____
Dr. Gary A. Evans, Professor

_____
Dr. Jerome Butler, Professor

_____
Dr. Ping Gui, Professor

_____
Dr. Jennifer Dworak, Professor

_____
Dr. Ralph Johnson, Principal Investigator

_____
Dr. Paul Pinsukanjana

DESIGN AND FABRICATION OF A LOW POWER 7.2 TERABIT TRANMITTER FOR EXASCALE COMPUTING

A Dissertation Presented to the Graduate Faculty of School of

Engineering

Southern Methodist University

in

Partial Fulfillment of the Requirements

for the degree of

Doctor of Philosophy

with a

Major in Electrical Engineering

by

Scott McWilliams

B.A. Physics, Sonoma State University, Rohnert Park, CA
M.S. San Jose State University, San Jose, CA
MBA SUNY Oswego, Oswego, NY

December 16, 2023

ACKNOWLEDGMENTS

Without question, my biggest supporter is my wife Neusa, a very special person and the love of my life. She is the one that makes it so joyful to accomplish goals because I get to share it with her. I also want to thank my mother Dorothy, who had the patience to teach me to read and know the multiplication tables before I went to school. It was very special for me to go through this PhD program while my son Ruben was a student at Rensselaer Polytechnic Institute and my son Julian was a student at Columbia University. I don't think it's supposed to work this way, but it was my sons who taught me to work hard in school. Thank you! To my brother Doak, you were always there, taking care of me, protecting me, my true best friend, and being the most constant of mentors in my life.

My advisor Dr. Gary Evans is the most generous person I know. I have learned a great deal from him, not just in technical matters, but in being a better person. I would like to thank Dr. Dinesh Rajan, who granted me enough flexibility in my job to allow for coursework, research, and travel that led to this thesis.

I would like to thank Dr. Jerome K. Butler for his keen insights into grating theory and the development of key modeling software used for this work, and Dr. Nai-Hsiang Sun for creating a grating simulation software that was also used in this work. I often think of Dr. Ralph Johnson as my co-advisor, who patiently shared his vast wealth of knowledge with me and the other graduate students and was instrumental in securing the funding that enabled this research. I was

very pleased that Dr. Gui and Dr. Dworak agreed to be on my committee, it was really a pleasure to work with you during my time at SMU. Last but not least, I have known Dr. Paul Pinsukanjana since 2002 and have greatly valued his technical expertise and friendship over the years and his willingness to support the epitaxial laser growth and characterization for this thesis work.

It has been a pleasure working with my fellow graduate students Freddie Castillo, Maryam Dezfuli, and Weida Zhang. I am sure that I learned more from them than they ever learned from me, and I wouldn't have known where to start if it wasn't for all their quality work.

McWilliams, Scott

B.A., Sonoma State University, 1991
M.S., San Jose State University, 1999
MBA, State University of New York, Oswego, 2016

Design and Fabrication of a Low Power 7.2 Terabit Transmitter for Exascale Computing

Advisor: Professor Dr. Gary A. Evans

Doctor of Philosophy conferred Dec 16, 2023

Dissertation completed Oct 31, 2023

Enhanced Coupled Strength (ECS) gratings fabricated into III-V based devices offer high reflected power per unit length and broad band reflectivity as compared to conventional 1st order gratings, desired qualities for short-haul high speed transmitters that can be implemented without the need for chip-level temperature control, contributing to the low power per transmitted bit. For commercial DBR lasers, the grating reflectivity results in an extremely narrow reflectivity spectrum, which is highly desired for most/many applications, but requires a power hungry thermo-electric cooler to maintain a fixed frequency. The proposed LEAM (laser electro-absorption modulator) requires a broad reflectivity spectrum, which, by Fourier Transform theory, means the gratings have to be very short, which only ECS gratings allow.

By integrating the ECS gratings, laser, and electro-absorption modulator (EAM) into the same III/V epitaxial layers, the shift in wavelength due to temperature changes of the laser region will be identical to that of the electro-absorption modulator section, therefore eliminating temperature control requirements, contributing significantly to a low power per transmitted bit for data communications systems. A novel laser and integrated electro-optic

modulator will be described, that when coupled with CWDM and 12 channel ribbon fiber, can enable a total of 7.2 Tbps connectivity, with calculated operating speeds of >100 Gbps per channel non-return-to-zero (NRZ or PAM2). VCSEL based systems have shown signs of speed limits to significantly exceed 28 GBd (Gigabaud) PAM (4-level pulse amplitude modulation).

Additionally, short 2nd order outcoupling gratings can be designed into the transmitter device to efficiently outcouple power into a single mode fiber. From a manufacturability point of view, fabricating the devices with both p and n metal pads on the same side of the wafer as the out-coupler allows wafer level testing, which has been a key advantage of VCSELs (Vertical Cavity Surface Emitting Lasers). VCSEL epitaxial growth can contain on the order of thousands of discrete layers with a thickness of ~10 microns. By contrast, the epitaxy grown for this thesis work contains ~ 30 layers not including doping changes.

The transmitter is designed to leverage mostly existing mature semiconductor process methods with a few exceptions. Challenging process development work included methods to fill and planarize a low optical index material in the grating teeth spaces such that a higher index material can be deposited on top of the planarized low index layer and precisely coincide with the top of the grating teeth.

TABLE OF CONTENTS

LIST OF FIGURES

LIST OF TABLES

LIST OF ABREVIATIONS

GBd	Giga Baud - One GBd is equivalent to one billion symbols per second
ECS	Enhanced Coupling Strength
EAM	Electro-Absorption Modulator
LEAM	Laser Electro-Absorption Modulator
VCSEL	Vertical Cavity Surface Emitting Laser
NRZ	non-return-to-zero
QW	Quantum Well
PIC	Photonic Integrated Circuit
EPI	Epitaxial material layers
Tbps	Tera bits per second
SOI	Silicon On Insulator
QW	Quantum Well
QCSE	Quantum-confined Start Effect
ER	Extinction Ratio
CMOS	Complementary metal-oxide-semiconductor
BCB	Benzocyclobutene
LEAM	Laser – Electro-Absorption Modulator
CMT	Coupled Mode Theory
ECSNL	Enhanced Coupling Strength No Liner
ECSL	Enhanced Coupling Strength w/Liner
FWHM	Full Width Half Max
DFB	Distributed Feedback (laser)
DBR	Distributed Bragg Reflector

FDTD	Finite-difference time-domain
MOCVD	Metal Organic Chemical Vapor Deposition
MBE	Molecular Beam Epitaxy
MQW	Multi-Quantum Well
SCH	Separate Confinement Heterostructure
PECVD	Plasma Enhanced Chemical Vapor Deposition
SOG	Spin-On-Glass
SMF	Single Mode Fiber
SBIR	Small Business Innovative Research
BA	Broad Area (Laser)
LED	Light Emitting Diode
LOR	Lift-off Resist
RIE	Reactive Ion Etch
ICP	Inductively Coupled Plasma
HDP	High-Density Plasma

GLOSSARY

Out-Coupler	A optical components designed to allow light to leave the device, for example, to be collected in an optical fiber
Terabit	A terabit is a unit of digital information storage or transmission. It is equivalent to 1 trillion bits or pieces of binary data
Short-Loop	Intentionally processing only sections of the full process traveler in order to expedite learning or develop process steps
Full-Loop	Processing the wafers/devices through the entire process flow to produce completed devices
Facets	The ends of the laser cavity typically created by cleaving the crystal planes

CHAPTER 1

1.1 Introduction

In this dissertation, the design, fabrication, and testing of a short-haul high-speed, low power per bit telecommunication device will be explored. The monolithic integration of a device with the attributes described in this introduction is a novel solution to the limitations of the commercially dominant VCSEL based systems. With knowledge of the current performance specification of VCSEL based systems and understanding of the needs of the Department of Energy and NASA, who funded this work, the device is designed towards performance specifications that would result in a commercially competitive device. Initial work focused on a 1310 nm device, and the most recent funding from NASA is focused on a 1602 nm low power, low latency, 100 Gbps, NRZ (non-return-to-zero) Laser-EAM for a 7.2 Tbps transmitter. The fabrication of the devices has been quite challenging, with twelve or thirteen photo mask levels, ion implant, grating fabrication, BCB, spin-on-glass, etc. For this reason, the approach was to use short-loop process flows to develop the process and provide test data for subsequent designs. Sufficient success in the fabrication and testing was achieved to provide validation of the concept and to warrant the long-term goal of eventually working with a commercial foundry service for full-loop fabrication. Process work started at SMU and then shifted to UCSB because of the need to use photolithography stepper tools to achieve our design rules for alignment, the ability to process 3-inch wafers, and needed process tool capabilities such as laser end point in the plasma etch tools.

Optical-Fiber dispersion and loss have minimum regions at wavelengths near 1.3 and 1.55 μm and the goal to is to design efficient uncooled semiconductor lasers near these wavelengths. We can use an $Al_xGa_yIn_{1-x-y}As$-InP material system that has the advantage of reduced carrier leakage from the QW section in comparison to non-Al containing systems such as In-Ga-As-P [1,2,3]. This reduced carrier leakage results from having a larger band offset at the heterojunctions ($\Delta V_c = 0.72\Delta E_g$). This is important because the effective mass of electrons in the conduction band is significantly less than the effective mass of holes in the valence bands. This means that the design focus should be to provide a strong barrier to electrons in the conduction band instead of a strong barrier to holes in the valence band to prevent carrier leakage at elevated temperature [3]. A key design goal for the devices in this thesis is to comply with channel frequency constraints over a wide-temperature range such that at the system level, no active cooling of the device is required. The modeling detailed in [3] provides insight in what is considered to design to a specific wavelength such as 1.3 μm. Photonic software programs used to solve for optical gain energy band levels, wave functions, I-V and optical power as a function of drive current includes commercial software Harold (Photon Design) and LaserMod (Rsoft/Synopsis). A complete modal analysis resulting in the complex modal effective index, near fields, far fields, and confinement factors for all epitaxial layer are derived using Southern Methodist University developed WAVEGUIDE [4] software based on an algorithm developed by Robert Smith at the University of Washington [5].

ENERGY GAP OF $Al_xGa_yIn_{1-x-y}As$

E_g =	0.526+1.516x (1-x-y =0.82)	2% compressive-strain
	0.572+1.517x (1-x-y =0.74)	1.5% compressive-strain
	0.638+1.532x (1-x-y =0.67)	1% compressive-strain
	0.75+1.548x (1-x-y =0.53)	lattice matched
	0.79+1.568x (1-x-y =0.38)	1% tensile-strain
	0.81+1.578x (1-x-y =0.307)	1.5% tensile-strain
	0.83+1.588x (1-x-y =0.225)	2% tensile-strain

a)

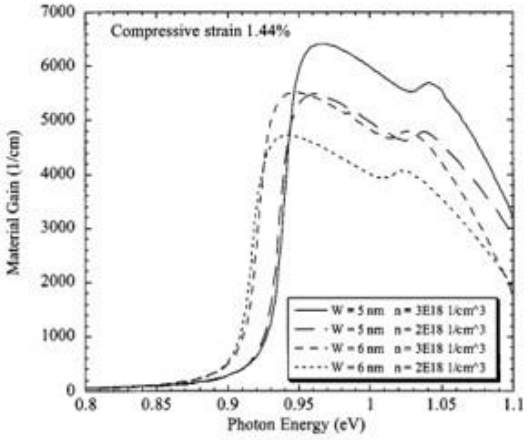

b)

Figure 1 a) The relation between energy gap and Al mole fraction x for the AlGaInAs material system for different values of strain and b) Material gain versus optical energy for 1.44% compressive strain in a single QW structure, for different QW width and carrier concentrations. The barrier energy gap is 1.16 eV [3].

A convenient formula for converting nm wavelength to energy is:

$$E = 1240/\lambda \qquad (1)$$

In Figure 1a, the relationship between energy gap and Al mole fraction for AlGaInAs material and the resulting strain is provided. 1.3 μm wavelength corresponds to the 0.95 eV on the graph (1b). In this case, an acceptable strain of the QW of about 1.4 % with a well-width between 5 and 6 nm with a QW quaternary composition of $Al_{0.16}Ga_{0.10}In_{0.74}As$ was determined to be the target specifications to meet the 1.3 μm wavelength device specifications. If we choose the correct QW width, we can get close to the peak energy of 1.3 μm. Further design choices are the number of QW to grow into the epitaxial structure. A well-known logarithmic relationship between the model gain $G_m(J)$ and the current density J for QW lasers is shown in equation 2 [6], where G_0 and Jo are the coefficients that depend on the material and width of the QW, and Γ_w is the QW mode confinement factor.

$$G_M(J) = \Gamma_w \cdot G(J) = \Gamma_w \cdot G_0 \left[\ln\left(\frac{J}{J_0}\right) + 1 \right] \quad = G_{0\text{modal}} \left[\ln\left(\frac{J}{J_0}\right) + 1 \right] \qquad (2)$$

By using this equation at the highest end of the device temperature operating range, the optimum gain per QW can be derived. This is followed by dividing the total required threshold gain G_{th} (equation 6) by the optimum gain per quantum well G_0 to get the optimum number of quantum wells for laser operation. The 1310 nm epitaxial structure designed and grown as part of this thesis work used 11 QWs of composition $In_{0.625}Al_{0.205}Ga_{0.17}As$, a number chosen to optimize EAM performance. Tensile strain was intentionally introduced into the barrier layers to balance the compressive strain from the QWs. Because of growth thickness and composition tolerances in the MBE (molecular beam epitaxy) growth tool, and the uncertainty in electronic and photonic parameters in the modeling software, the exact intended lasing wavelength at a given temperature will not be achieved. As an initial process step after epitaxial growth, a BA (broad area) laser is fabricated from a section of one of the wafers to determine what the wavelength actually is at given temperatures.

There are four viable economic-technological options for Photonic Integrated Circuits (PIC) [7]; 1) Attempting to fabricate a high density of photonic components in the InP or GaAs compounds themselves, an approach implemented by the Infinera Corporation for example[8]; 2) silicon photonics-silicon on insulator (SOI/BOX) [9], where light is injected into the silicon photonics by a separate discrete light source (such as an III/V based laser diode, either edge- or surface-emitting)[10]; and 3) heterogeneous integration of III-V on SOI, typically accomplished by growing the laser EPI QW layers on relatively small InP or GaAs wafers, cleaving them into small pieces and then bonding to large SOI wafers (by Intel Corporation for example)[11]. In

this case, the optical complexity is fabricated into the silicon on relatively large diameter SOI wafers. This approach has the advantage of using the direct bandgap properties of InP or GaAs compounds for light production, and the low cost, mature, high component density, and high index contrast waveguides of CMOS processing. Finally, 4) epitaxial growth of III-V on silicon. Commercializing such an approach offers a huge advantage for next generation photonics for obvious reasons, justifying continued research into this area.

1.2 Key attributes of proposed device

The hypothesis for this thesis is that the following monolithically integrated devices will have performance specifications that are grounded in sound theory and the elements making up the integrated device will combine to possess the following attributes: 1) a high absorption, compact, low capacitance electro-absorption modulator (EAM); 2) tracking of the peak lasing wavelength with the peak modulator absorption spectrum over temperature [12]; 3) a high quantum well confinement factor (reduces laser threshold and increases EAM efficiency); 4) broad-band, compact ECS (Enhanced Coupling Strength)[13] first order distributed Bragg reflector mirrors; and 5) a (future, optional for now) low back reflection, high efficiency enhanced coupling strength (ECS) second-order grating output coupler with a narrow vertical beam [14,15]. Additionally, design for radiation tolerance was a key component of the early DOE funding, for both the silicon drive circuitry as well as the III/V based laser/EAM. A novel laser and integrated electro-optic modulator will be described, that when coupled with a WDM and 12 channel ribbon fiber, can enable a total of 7.2 Tbps connectivity, with calculated operating speeds of >100 Gbps per channel non-return-to-zero (NRZ or PAM2). VCSEL based systems have shown signs of speed limits to significantly exceed 28 GBd PAM4 [16,17].

The design effort described in this thesis focused on the ECS first order gratings that act as front and rear mirrors with targeted bandwidths, and efficient coupling from a second order out-coupler to a single mode fiber. The device and EPI structures were designed around tradeoffs towards a satisfactory ridge laser and an efficient electro-absorption modulator that is based on the quantum confined Stark effect that possesses very high speed, a high extinction ratio and a low drive voltage. The design efforts started with optimizing the EAM, then considered some compromising of the EAM design to ensure the needed laser performance. The design challenge, and the primary reason that the DOE and NASA provided funding for this work, is towards a device that can significantly outperform the dominant VCSEL technology for this application mainly in the long wavelength region in terms of modulation speed, energy/bit, and un-cooled temperature operating range. To achieve such a device requires developing a fabrication process flow to fabricate the full device as envisioned.

The device (Figure 2) consists of a transmitter where the laser ridge and EAM are patterned and etched at the same time in the same EPI. The first order grating sections serve as the back and front mirrors of the laser cavity and a second order grating is used to couple the transmitted pulses of light out of the surface of the device, 10 element array shown in 2A, and the full device cross-section shown in 2B. The photolithography mask layout for a single element is shown in 2C.

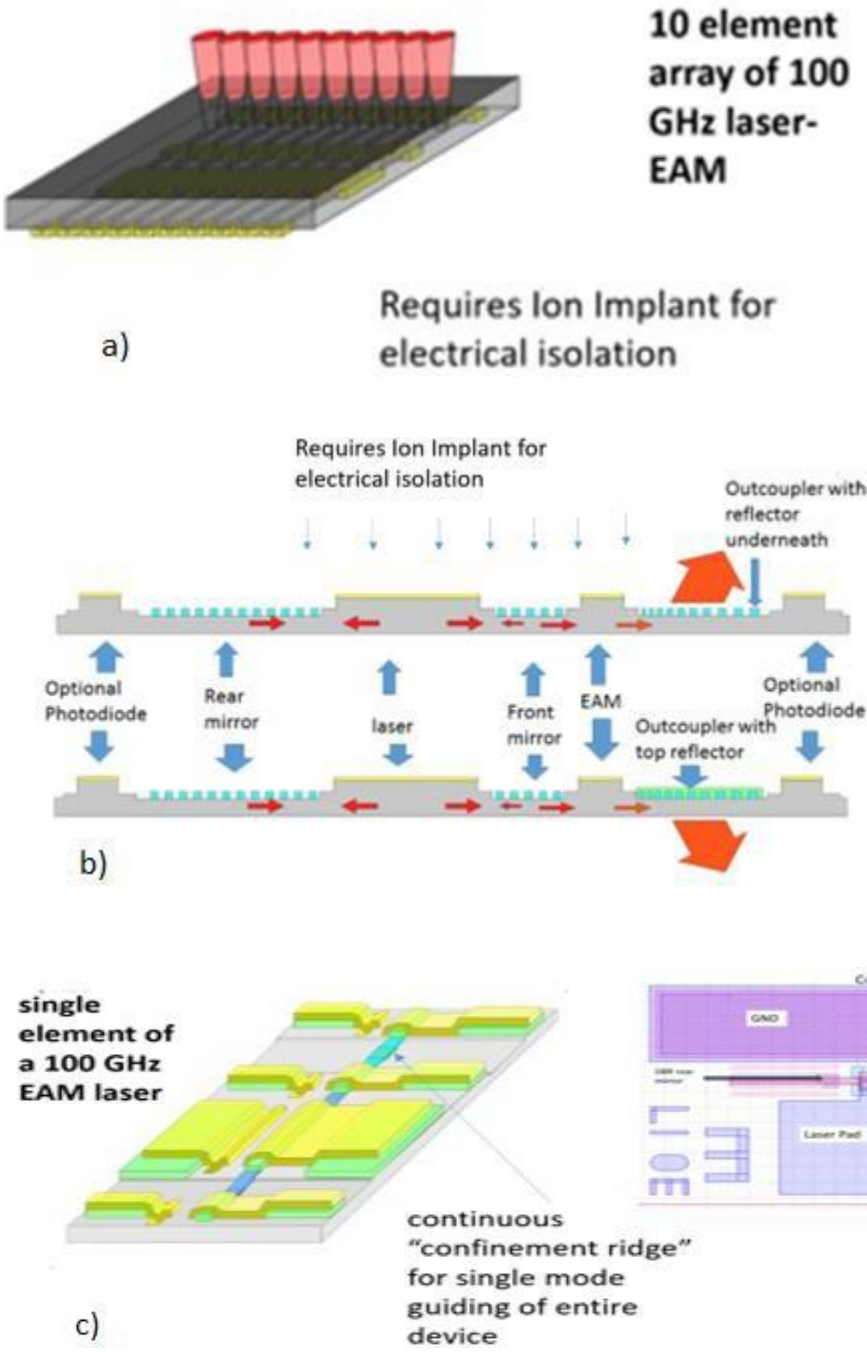

Figure 2. 7.2 Terabit Transmitter Concept A) Array concept B) Cross-section view of device showing outcoupled light C) Device layout and Photolithography Mask Layout of one element

For purposes of lower capacitance and therefore higher modulation speed, the probe pads were designed with the minimal area that the probe could contact. As shown in Figure 3, the contact metal was deposited on top of the low dielectric constant Dow BCB material (Benzocyclobutene). Lastly, the confinement ridge concept is illustrated, where the needed lateral index step for modal control is fabricated by patterning the dielectrics and etching on the device surface. The white colored ridges on either side of the gratings are "dummy" ridges used to aid in the resist flow uniformity during the gratings process. The basic geometry and location of these dummy ridges were developed by Dr. Gary Evans and Jay Kirk in work at RCA Labs. Because of gain induced index depression [18], the laser region needs a lateral index step of > 0.01. In the connecting regions, the delta can be ~0.001 or less, where the concern is obtaining sufficient mode overlap.

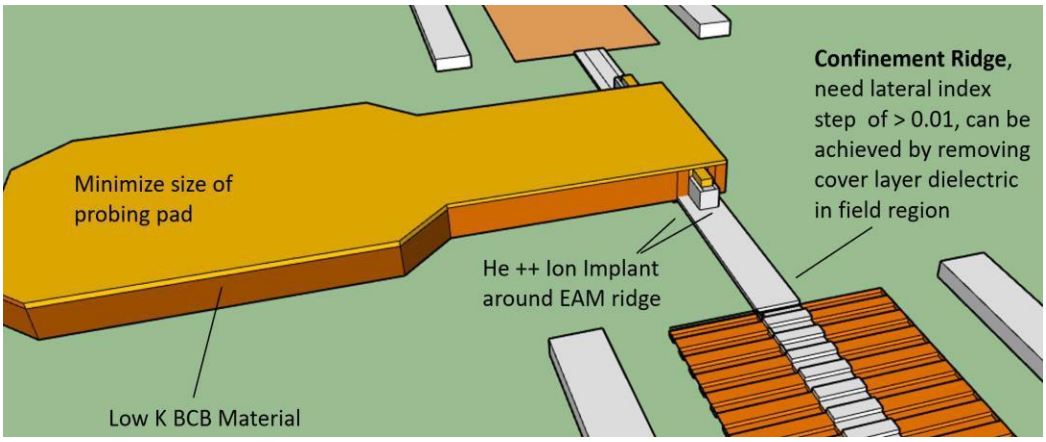

Figure 3. Bonding pad on BCB, Isolation Ion Implant, and Confinement Ridge.

To summarize the key technology attributes of the proposed device:

- Can operate without temperature control
- Compatible with SMF (1260 to 1675 nm);

- Modulation speed is limited by capacitance of the modulator (BCB film thickness has a significant role in modulation speed and the "speed calculator" and is described in section 3.5). The formula for capacitance of a capacitor C =electric constant*area/distance indicates that C decreases as d is thicker. BCB has a relatively low electric constant.
- ECS gratings enable a wide bandwidth and relatively short gratings
- Device can be designed for vertical or end coupled light emission.

1.3 Compound Semiconductor Light Emitters

Researchers have been working for decades on the possibility of using silicon based light emitters that would be ideal for manufacturing optically based products that possess high optical component density and low-cost manufacturing [19]. Over 50 years ago, it was predicted that a silicon-germanium alloy with a hexagonal crystal structure could possess a direct band gap. At normal ambient conditions, both silicon and germanium have a diamond-like crystal structure, so research focused on producing a hexagonal structure with a nanowire approach. But today, silicon still cannot be used as an efficient light emitter for silicon photonics and therefore direct bandgap III/V compound light emitters need to be incorporated in silicon photonics or used as standalone GaAs or InP based devices.

The wavelength is determined primarily by the band gap energy (Eg) of the quantum well active region material and can be fine-tuned by adjusting the width and composition of the quantum wells [3]. The band gap is an intrinsic property of materials which is defined as the difference between the lowest quantum level of the conduction band and the highest (lowest from the hole point of view) quantum level of the valence band. For direct bandgap semiconductors, an electron in the conduction band can combine with a hole in the valence band and emit a photon with an energy that is approximately equal to the band gap energy and both

energy and momentum (= $\hbar$*k) are conserved. Therefore, the wavelength and frequency f of the photon is related to the bandgap by

$$E_g = E_{photon} = hf = \frac{hc}{\lambda} \quad (3)$$

If the energy has units of electron volts (eV), the wavelength of light in micrometers is given by

$$\lambda(\mu m) \simeq \frac{1.24}{E_g\ (eV)} \quad (4)$$

Figure 4 illustrates an optical difference between direct and indirect laser materials. We can think about a single electron traveling through a lattice of perfect periodicity such that the wave function is in the form of a plane wave in the x-direction with a propagation constant **k**. The space dependent wave function of the electron modulated by U($\mathbf{k}_x$,x) in the lattice.

$$\psi_k(x) = U(k_x, x)e^{ikx} \quad 5)$$

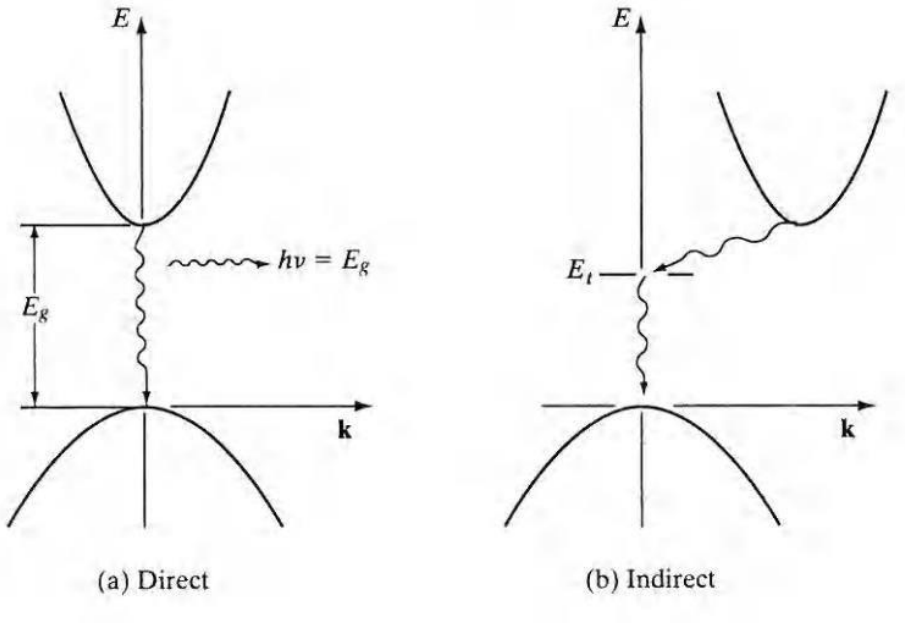

Figure 4 a) Direct electron transitions where momentum ($\hbar$*k) is conserved and b) indirect electron transitions that does not converse momentum [20].

Referring to Figure 5, if we made a laser diode out of GaAs based materials, such as the material system along the tie line for GaAs-AlAs, we have a range of compositions that are direct gap material, latticed matched to GaAs, and can provide a range of bandgap energies (and thus wavelengths). Such a GaAs based device would have a direct bandgap and electrons in the conduction band would drop to an empty state in the valence band, giving off the energy difference Eg as a photon. But for silicon, such a trip from the conduction to the valence band would require a momentum change as well as a change in energy. Such transitions mainly occur non-radiatively and the recombination energy heats up the lattice.

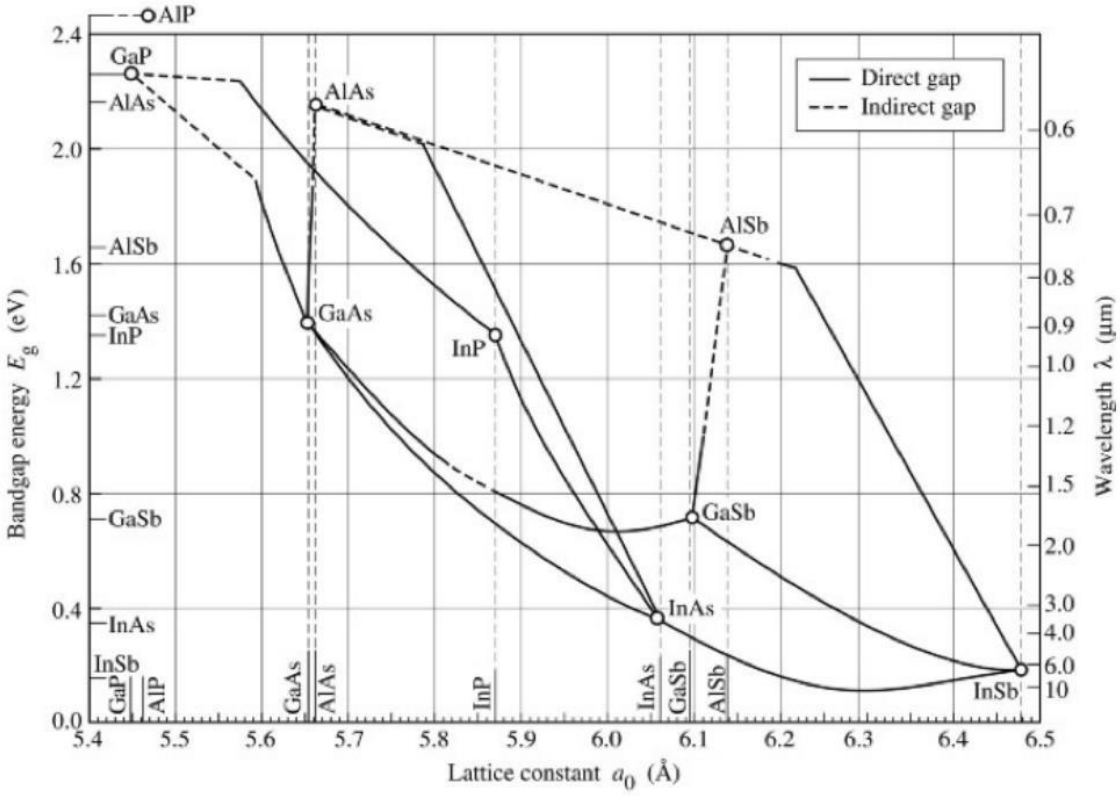

Figure 5 Band gap vs. lattice constant for some III/V semiconductor materials [21].

1.4 Laser and EAM

Like other types of lasers, semiconductor lasers require a population inversion that results in gain. This gain for semiconductor lasers is driven by current injection, and at low current levels, the electrons find their way to the conduction band and holes to the valence band in the quantum wells. The holes and electrons will combine in the quantum wells and produce photons. In stimulated emission, the emitted photons have the identical λ, direction, and phase of the stimulating photons, and reflecting cavity ends are required to provide the feedback required for any oscillator. Typically, laser diodes use cleaved facets for this purpose, forming a Fabry Perot cavity. Cleaved facets have a reflectivity of ~ 32%. To capture all the light produced out one end and to improve reliability, facets can be coated with dielectric stacks [22] to provide ~100% reflectivity on the back facet and a low reflectivity (1% to ~50%, depending on laser length and desired performance) on the front facet. Often, photo diodes are used to detect light from the back facet and provide feedback to power control circuits. In the case of the work in this thesis, the feedback is controlled by first order gratings, whose properties are discussed in Chapter 2. When the difference between the quasi-fermi level in the conduction band (E_{fc}) and the quasi Fermi level in the valence band (E_{fv}) is greater than E_g, a transparency current is generated and the laser experiences net gain due to the current injection.

$$g_{th} = \Gamma_{active} G_{mat} = \alpha_{int} + \frac{1}{2L} ln \frac{1}{R_1 R_2} \qquad (6)$$

R_1 and R_2 is the mirror reflectivity (due to cleaved and coated facets or to gratings) and the cavity length is L. Γ_{active} is called the quantum well confinement factor and is the fraction of the total modal power that is contained in the quantum wells. The internal loss α_{int} is driven by many factors, primarily the material quality, p- and n-doping of each layer, variations in layer

thicknesses and layer compositions, and interface roughness/irregularities that cause scattering [23].

The integrated QW laser and electro-absorption modulator design examined in this thesis operates on the principle of the Quantum Confined Stark Effect (QCSE), whereby an applied field shifts the absorption spectrum. In a general case, the absorption of photons with energy > bandgap results in an electron-hole (e-h) pair, generating electrons in the conduction band and holes in the valance band. An exciton is described as a weakly bound state created by coulombic forces between the pair. But with QWs present, these otherwise weakly bound excitons are further bound and exhibit higher binding energies [24], enough for a highly absorbing EAM device. If we compare the room temperature absorption spectrum of bulk GaAs to a QW GaAs-AlGaAs epitaxial structure, shown in Figure 6, we see that the MQW structure exhibits relatively narrow peaks (at different energies for heavy and light holes), evidence of excitons.

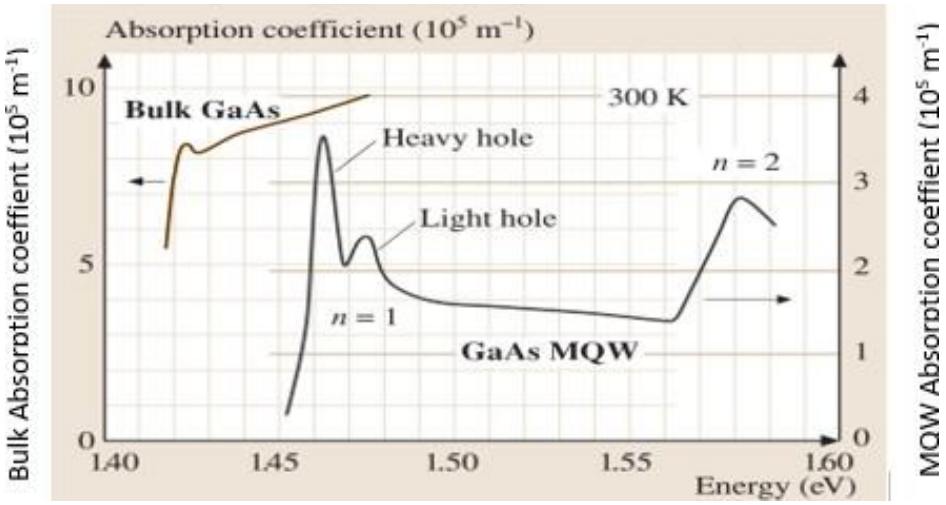

Figure 6 Comparing the absorption spectrum of bulk GaAs to a MQW epitaxial structure of GaAs-AlGaAs [24].

For an MQW EAM device, we are interested in how the excitons respond to applied electric fields (due to a rapidly changing applied voltage). Figure 7a shows that when an electric field is applied, the well tilt lowers the electron energy level and raises the hole energy level. Additionally, a separation of the electron and hole wavefunctions occur that results in a decreased overlap and thus decreased absorption. The Eg is nominally the same across the well, but the tilt in the well lowers the electron energy level and raises the hole energy level. It also spatially separates the electron and hole wavefunctions decreasing the overlap and thus decreasing absorption. In the absence of the applied electric field, the electrons and holes in the QW region must exist within energy sub-bands, implying that only a light wavelengths in the allowed bands can be emitted or absorbed. The applied field shifts the electrons to lower energies and holes to higher energies, restricting the permitted emission or absorption wavelengths. Referring to Figure 7, the applied field also has the effect of reducing the recombination efficiency by decreasing the overlap integral as the field moves electrons and holes to opposite sides of the well.

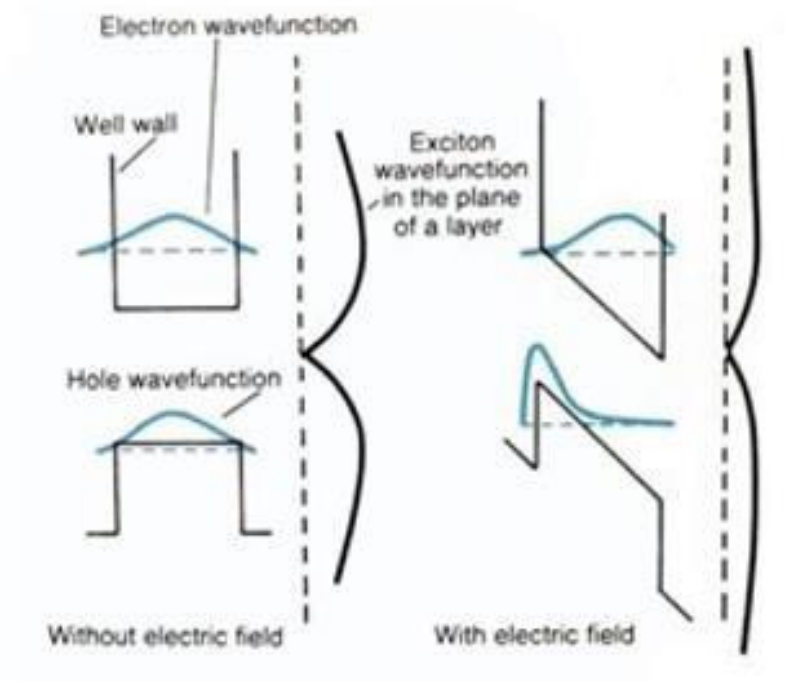

Figure 7 Exciton wavefunction without and with applied fields

The relationship of the optical intensity going into an EAM to that going out of the EAM is:

$$I_{out} = I_{in}e^{-\alpha d} \qquad (7)$$

Where α is the absorption coefficient with typically units of cm^{-1} and d (also called Lmod), is the length of the modulator. The total thickness of all the quantum wells is incorporated in alpha. The modulator extinction ratio (ER) is defined as the ratio of transmitted on/transmitted off power.

CHAPTER 2

2.1 Grating Theory

Maxwell's equation describes the propagation of optical waves in various media [26], with four fundamental laws that apply to electromagnetic waves:

$$\nabla \times E + \frac{\partial B}{\partial t} = 0 \tag{j8}$$

$$\nabla \times H - \frac{\partial E}{\partial t} = J \tag{9}$$

$$\nabla . D = \rho \tag{10}$$

$$\nabla . B = 0 \tag{11}$$

Where E has units of volts per meter (V/m) and H with units of amperes per meter (A/m). The electric displacement vector D has a unit of coulomb per square meter (C/m^2) and the magnetic flux density vector B has the unit of Tesla. B and D values can change according to what material the electromagnetic waves are propagating through. The scaler electric charge density equation

includes ρ, with a unit of coulomb per cubic meters (C/m^3), and the electric current density vector where J has units of ampere pe squared meters (A/m^2).

Equations 12 provides the relationship between the electric displacement and the electric field and Equation 13 provides the relationship between the magnetic flux density vectors and the m

$$D = \epsilon E \tag{12}$$

$$B = \mu H \tag{13}$$

Where $\epsilon = \epsilon_r \epsilon_0$ is the permittivity of the media in (F/m) and $\mu = \mu_r \mu_0$ is the permeability of the media in (H/m). The relationship between the refractive index n and ϵ is stated as $\epsilon = n^2 \epsilon_0$ and the dielectric constant $\kappa = n^2 = \epsilon/\epsilon_0$.

Layered waveguides in the form of long rectangular slabs with the propagating media sandwiched between symmetrical or asymmetrical layers of lower index material are studied to understand what modes (guided modes) will propagate and where the cut-off frequency is. Using boundary conditions, Maxwell equations are applied to solve the eigenvalue equations for the guided modes.

The longitudinal propagation constant for such a slab waveguide defined as:

$$\beta = k_0 n_{eff} \tag{14}$$

Where k_0 is the propagation constant $k_0 = \frac{2\pi}{\lambda_0}$, λ_0 is the free space wavelength, and n_{eff} is the effective index.

The propagating mode can be guided (transverse), leaky, or radiative (longitudinal). Waveguide modes can be either transverse electric (TE) or transverse magnetic (TM) [27]. With the coordinate system shown in Figure 8, TE modes only have E_y, H_x, and H_z components and TM modes only have H_y, E_x, and E_z components.

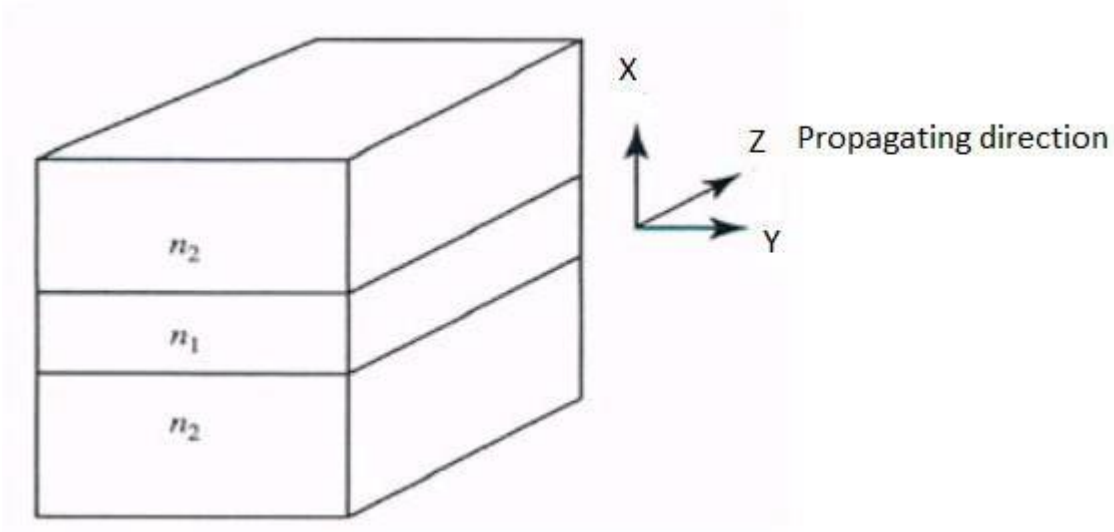

Figure 8 Symmetrical slab waveguide where $n_1 > n_2$

For simplicity, we let the yz plane be infinite and assume a periodic time-dependent wave $e^{j\omega t}$ is propagating where ω is the angular frequency. We identified that the propagating direction is z, so the waveguide varies as $e^{-\gamma z}$ where $\gamma = \alpha + j\beta$ is the complex propagation constant, α is the attenuation constant and β is the phase constant. Then:

$$\psi = e^{j\omega t - \gamma z} \tag{15}$$

If we also simplify by stating that the waveguide has no losses, then the field distribution as a can be stated as:

$$\psi = e^{j\omega t - j\beta z} = e^{j(\omega t - \beta z)} \tag{16}$$

Figure 9 is a $\omega - \beta$ diagram that illustrates the various mode regions and their relationship to the speed of light. Is this generic diagram, c/n_2 defines the cut-off region.

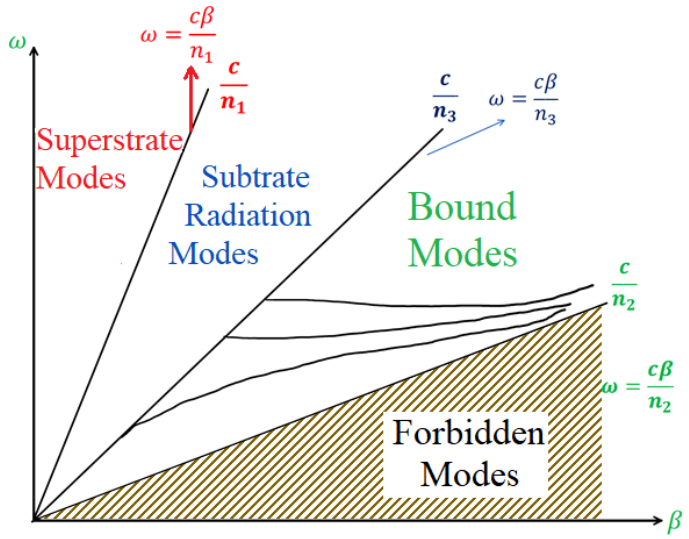

Figure 9. $\omega - \beta$ diagram for a generic dielectric waveguide

The laser EAM employs first order gratings that can be tailored to select the needed frequency at the desired bandwidth and reflectivity. We desire the first order grating region of the waveguide to remain non-radiating and single mode. For these conditions, a relatively straightforward thin-film effective index method is accurate [28,29]. A simplified high index contrast Si waveguide structure is shown in Figure 10, where above the gratings is air (index ~ 1),

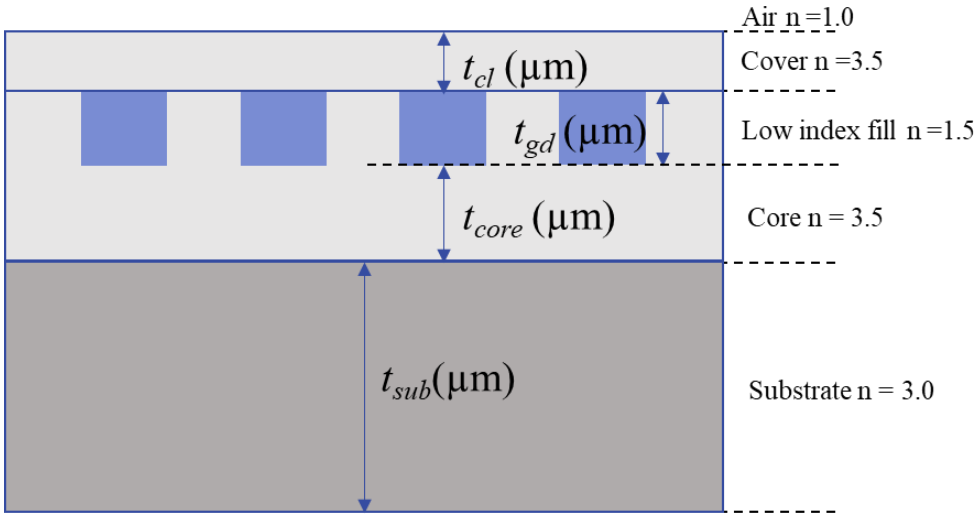

Figure 10 Simplified grating structure used to explore the parameter space to design the full 11QW EPI telecom device.

and in Figure 11a, where a lower-index liner layer is introduced. For Figure 11c, the grating teeth are filled with a lower index material (in the case of this thesis work, spin on glass with an index of ~ 1.36), and a higher index cover layer on top of the gratings. [30, 31]. Figure 11d is a diagram of an equivalent thin-film model of these waveguides where n_1 and n_2 are the effective indices. The effective index is defined as the ratio of the longitudinal β propagation constant in the waveguide to the free space propagation constant k, and in our case, we are assuming single mode. Additional modes would each have different effective indices. Throughout this thesis, the structure in Figure 8b is called the ECSL (Enhanced Coupling Strength w/Liner), where the liner is a conformal layer deposited on the gratings, and Figure 8c is called the ECSNL (Enhanced Coupling Strength No Liner) case where there is no liner.

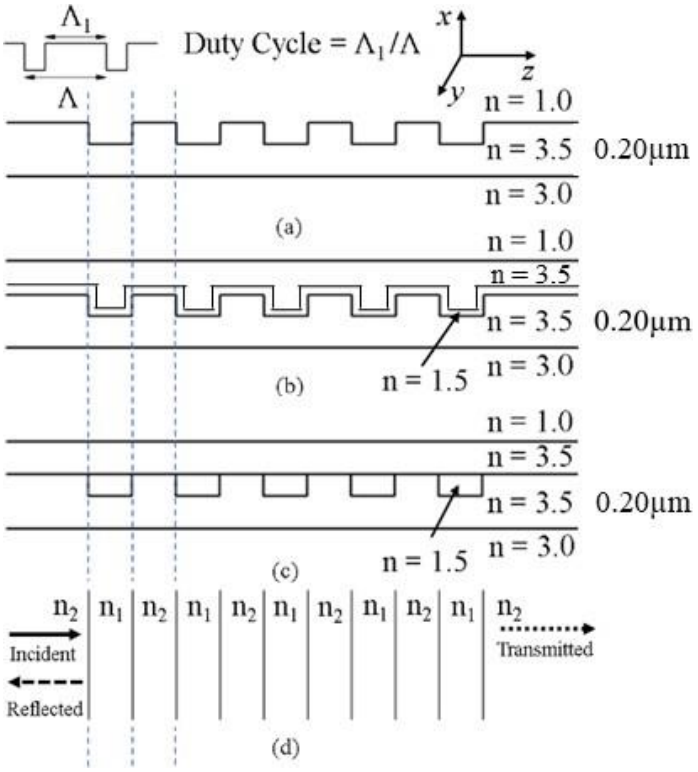

Figure 11 Simplified grating structure a) with only air above gratings b) with conformal low index layer c) with low index grating fill and cover layer d) equivalent thin film model

The laser/EAM employs ECS gratings that can achieve the required device specifications for reflectivity, spectral width, or outcoupling with gratings lengths from ~ 10 – 40 μm when integrated into an InP-based laser + EAM design. Such a design, with the identical epitaxial structure for both the laser and the EAM allows wide temperature range operation (tracking of temperature driven wavelength shifts between the laser and EAM sections).

A simplified structure is one that does not include the actual laser MQW epitaxial structure but includes minimal structures that allow deep understanding of the design approach to achieve the desired specifications. We are interested in understanding the reflective properties of first order gratings close to $2\beta = K$, where β ($\beta = 2\pi/\lambda_g$). β is the longitudinal propagation vector, K

= $2\pi/\Lambda$, λ_g is the wavelength of the propagating mode inside the waveguide ($\lambda_g = \lambda_o/n_{eff}$), k_o = $2\pi/\lambda_o$, λ_o is the free-space wavelength, $n_{eff} = \beta/k_o$, and $k_o = 2\pi/\lambda_o$. With m being the grating order,

$$\Lambda = \frac{m\lambda_0}{2n_{eff}} = \frac{m\pi}{\beta} \tag{17}$$

The coupling strength κ_{pq} between forward (mode p) and backward propagating (mode q) of a first order grating with the grating teeth etched to a depth of a is given by

$$\kappa_{pq} = \frac{\omega\epsilon_0}{4} b_m (n_1^2 - n_2^2). \int_{-a}^{0} E_p^*(x) E_q(x) dx \tag{18}$$

The integral expression is the grating confinement factor Γ_g, which is the fraction of modal power in the grating layer, b_m is the Fourier coefficient corresponding to the first order, ω = angular frequency, n_1 and n_2 are the indices of the layer above and below the gratings, respectively. Figure 12 shows the normalized intensity modal profiles for the various structures provided in Figure 11. As will be shown in proceeding sections, filling the space between the grating teeth with a low index material, or by using a liner layer, causes an increase of $(n_1^2 - n_2^2)$. Depositing a high index material on top of the gratings has the effect of pulling up the mode into the grating region (increasing Γ_g). For first order mirrors, ECS gratings enable a short grating length with high and broad spectral reflectivity. For 2nd order out-couplers, ECS enables a short grating length with low back reflection. Several simplified structures are analyzed in this thesis, mainly, the liner structure shown in 12d, where a low index liner is deposited conformally on top of the grating teeth, and no-liner case 12e, where a low index material is fabricated in the grooves of the teeth and planarized to the top of the gratings. The use of a thin, low-index liner layer over a surface grating covered by a high-index cover layer in an III-V alloy waveguide was shown to significantly improve the coupling efficiency of grating

out-couplers, thereby enabling length of such couplers to be an order of magnitude shorter than conventional gratings for similar laser waveguide applications [32]. This paper also describes that the same low-index liner and high-index cover layer can also reduce losses between transition sections of photonic integrated circuits (PICS), or between a laser region and a Distributed Bragg Reflector (DBR).

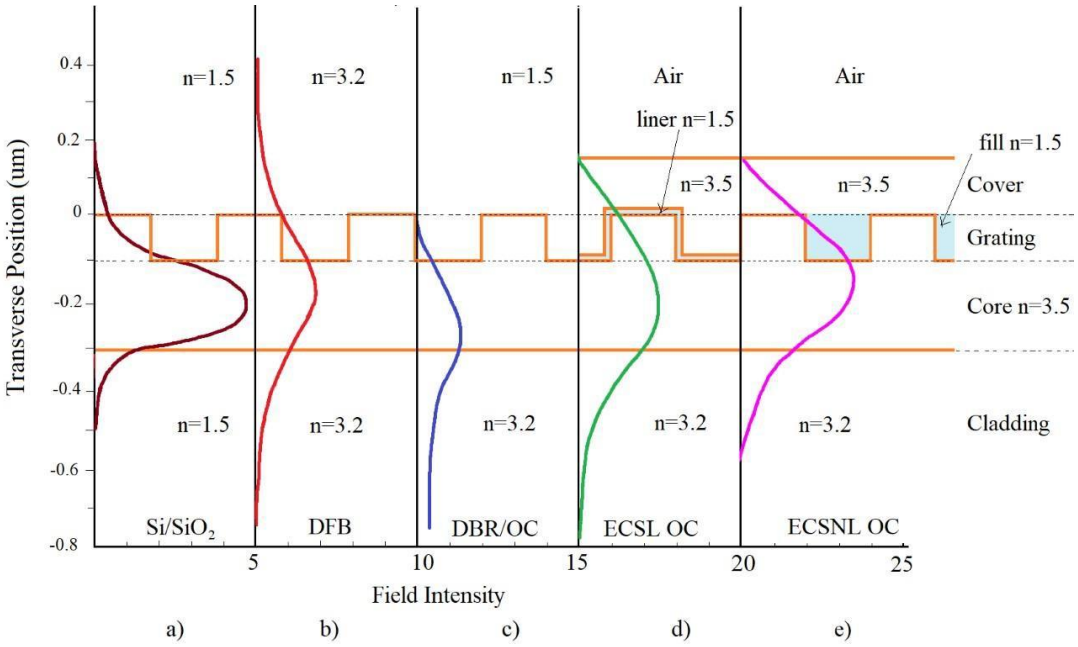

Figure 12 Normalized intensity modal profiles for (a) Si/SiO_2 photonic Waveguide, (b) conventional DFB, (c) a conventional DBR, (d) an ECS grating with a thin liner (ECSL), and (e) an ECS grating with no liner (ECSNL). Each waveguide has the identical core thickness (0.3 micrometers), core index (3.5), and grating depth [32].

Using Couple Mode Theory (CMT), the reflection and transmission amplitude coefficients, r and t are derived [33], where L is the length of the gratings and $S = \sqrt{|\kappa|^2 - (\Delta\beta)^2}$, $\Delta\beta = \beta - \frac{\pi}{\Lambda} = 2(\beta - \beta_0)$ is the detuning parameter, and κ is the coupling coefficient defined in (pt).

$$r = \frac{-\kappa * sinh(SL)}{\Delta\beta sinh(SL) + iScosh(SL)} \tag{19}$$

$$t = \frac{iS}{\Delta\beta sinh(SL) + iScosh(SL)} \tag{20}$$

By examining equation 18, we see that the coupling strength depends on the grating confinement factor Γg and the magnitude of the difference of the index of refraction on either side of the gratings. For the conventional DFB (Figure 9b) and DBR (Figure 9c) laser/grating structures, such coupling is increased by increasing the depth of the etched gratings, but this also pushes down the waveguide mode towards the substrate and thereby eventually reduces Γg.

If we compare the modal profile for Figure 9a and 9b, we can design ECS gratings in III/V waveguides that possess similar Γg enjoyed by silicon photonics. This ECS design includes carefully choosing the index of refraction of grating liners, fills, or cover layers.
Figure 9e is the structure we ultimately chose to apply for this thesis work, and Figure 10 provides a layout of a simplified structure to study with the aid of the Floquet-Bloch based software. We will explore the parameter space for the various thickness layers, duty cycles, and grating depths and the resulting reflectivity, transmission, and outcoupling performance. The goal of this exercise is to apply what we learn to the funded telecom MQW laser device. A thorough investigation of the parameter space for the structures is shown in 12c, 12d, and 12e for first and second order gratings are provided in the thesis dissertations of Mary Dezfuli [34] (SMU 2022) and Freddie Castillo [35] (SMU 2022), research group colleagues of the author of this thesis. The research group, in collaboration with Photon Sciences' engineers, applied this learning to help design the transmitter device described in this thesis.

2.1.1 Floquet-Bloch Theory

The grating analysis work in this thesis leveraged two different SMU developed Floquet Bloch based software programs. One program is developed by Professor Nai-Hsiang Sun as part

of his graduate work at SMU, and the other program was developed by Professor Jerome Butler. Ongoing work is to compare the results of these two programs with commercially available FDTD software such as Rsoft.

Grating analysis becomes more complex when we are also concerned about radiating structures, and ones with deeper gratings [36, 37, 38]. Hence, the SMU developed software is used for exploring reflection, transmission, and radiation of a wide range of structures. The software allows the number of terms denoted as space harmonics to be calculated, with increased accuracy in choosing a higher number of harmonics.

The y-component of the electric field in the i^{th} layer can be written as:

$$E_y^{(i)}(x,z) = \mathrm{f}^{(i)}(x,z)e^{-\gamma z} \tag{21}$$

where $\gamma = \alpha + j\beta$ is the complex propagation constant of the mode with α as the attenuation constant, β as the longitudinal propagation constant, and $f^{(i)}(x,z)$ is a periodic function defined as $f^{(i)}(x, z+\Lambda)$, which can be expanded into a Fourier series and define the electric field:

$$E_y^{(i)}(x,z) = \sum_{n=-\infty}^{\infty} f_n^{(i)}(x)e^{-jk_{zn}z} \tag{22}$$

By substituting (21) into (22), the electric field can be written as:

$$\begin{aligned} E_y^{(i)}(x,z) &= \mathrm{f}^{(i)}(x,z)e^{-\gamma z} \\ &= \sum_{n=-\infty}^{\infty} f_n^{(i)}(x)e^{-jnKz}e^{-j(\alpha+j\beta)z} \\ &= \sum_{n=-\infty}^{\infty} f_n^{(i)}(x)e^{-jK_{zn}z} \end{aligned} \tag{23}$$

where $f_n^{(i)}(x)$ is the amplitude of the electric field for the nth space harmonic in the ith layer. The complex propagation constant of the nth space harmonic is denoted by K_{zn} defined as:

$$K_{zn} = ß_n + j\alpha = (ß_o + nK) + j\alpha \tag{24}$$

where ß$_n$ is the longitudinal propagation constant of the nth space harmonic, K is the grating wavenumber, and α is the attenuation coefficient. The complex effective index is defined by:

$$n_{eff} = \frac{\beta}{k_o} + j\frac{\alpha}{k_o} \tag{25}$$

For 1st order gratings, the Bragg condition occurs when ß equals 2K and for 2nd order gratings, the Bragg condition occurs when ß equals K.

2.2 Enhanced Coupling Strength Gratings 1st order grating parameter space

The structures to be studied all possess a 0.3 um thick waveguide, the high index deposited layers will be fixed to an index of 3.5 (silicon), an index of 1.5 is chosen for the low index material (silicon dioxide, but in the actual fabrication, we used spin on glass (SOG) with an index of 1.36). Figure 13 details the abovementioned indices and material choices for the simplified structure, with the liner structure in the top figure and the no-liner structure in the bottom.

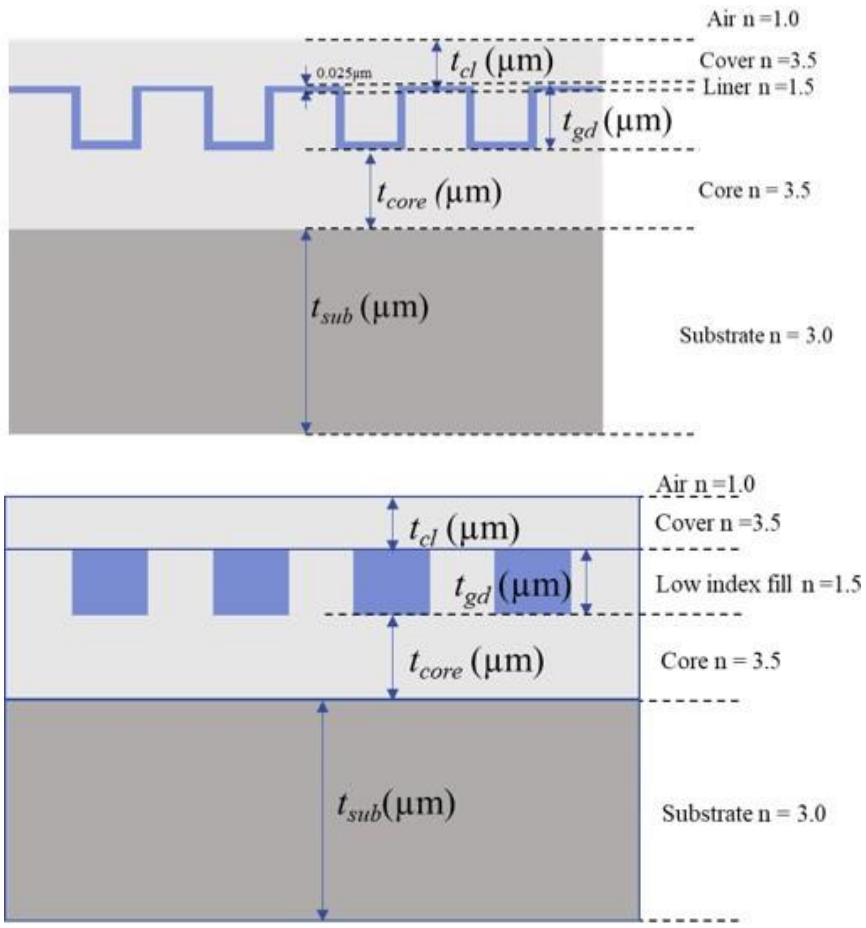

Figure 13 Simplified structure for 1st and 2nd order grating space exploration, Top = Liner, Bottom = no-liner

There are several approaches to perform calculations for this grating structure. If we only want to analyze reflection, and not power up and down, we can use a straightforward effective index approach. If we want to analyze transmission, reflection, coupled up, and coupled down power (into the substrate), we can use the Floquet-Bloch method with the SMU software, or FDTD software such as Rsoft. Figure 14 overlays reflection verses wavelength results for the effective index, Floquet-Bloch, and FDTD methods and the agreement is good. The deviation of the effective index method is not surprising since is doesn't use the modal effective index in the calculations.

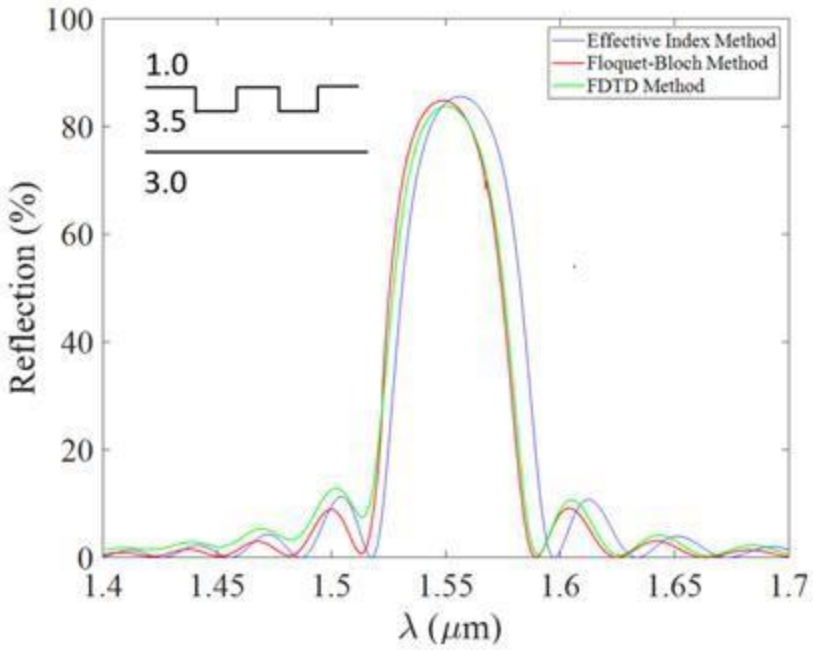

Figure 14 Comparing Effective Index, Floque-Bloch, and FDTD methods for reflection verses wavelength. Grating is 10 microns long with 50% duty cycle/100nm deep gratings

2.3 Parameter Space of 1st Order ECSNL Gratings in Basic Waveguide Structures

As mentioned earlier in this thesis report, the full parameter space for ECSL and ECSNL structures are reported in the dissertations of fellow PhD students Freddie Castillo and Mariam Dezfuli in 2022. Here, only a summary of the ECSNL approach is given, the approach that was ultimately used for the fabrication of the 11QW devices.

2.3.1 Variations in the cover layer thickness

We will fix the grating depth to 100 μm and the duty cycle to 50%. Figure 15 reveals the increased coupling due to the addition of the high index cover layer as compared to conventional gratings (air above the grating teeth). In this case, the maximum grating coupling factor is achieved with a cover layer thickness of 0.24 μm.

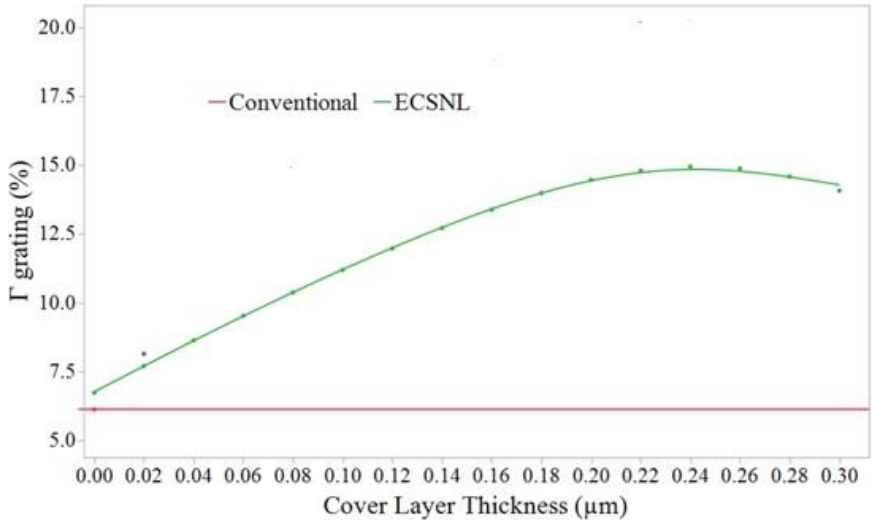

Figure 15 Grating Confinement Factor for various cover layer thicknesses compared to conventional gratings

Figure 16 gives the normalized complex effective indices β/k_0, and α/k_0 as a function of wavelength with the duty cycle (DC) fixed at 50% and the grating etch depth fixed at 0.1 µm.

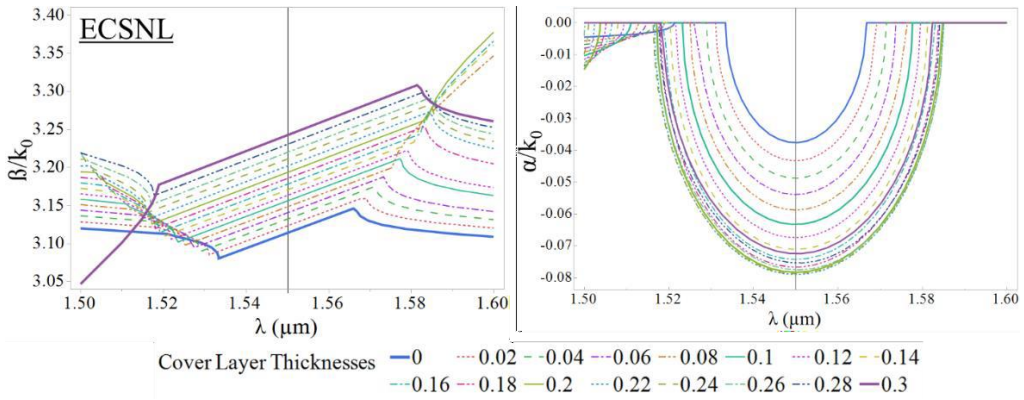

(a) (b)

Figure16 a) Normalized Longitudinal propagation constant, β/k0, as a function of wavelength for, b) α/k0

The maximum value of α corresponds to the 1st order coupling coefficients κ [39]. The grating periods were chosen such that the 1st Bragg condition is about 1.55 µm. At the lower wavelength

regions, where there is a sudden deflection of β/k0 or α/k0, indicates that the structure is radiating (not all the power is accounted for by summing reflection and transmission).

It is important to consider the reflection spectrum of the gratings design. For example, we may desire a certain bandwidth that maintains a flat high reflectance across these wavelengths. Figure 17 indicates that the ECSNL design can enhance these desired characteristics compared to conventional gratings. A key advantage of ECS gratings is that they achieve high reflectance and bandwidth with relatively short gratings. With a 10 μm long grating, the ECSNL achieves nearly total reflection with a dramatically larger full with half max (FWHM) compared to the conventional gratings approach.

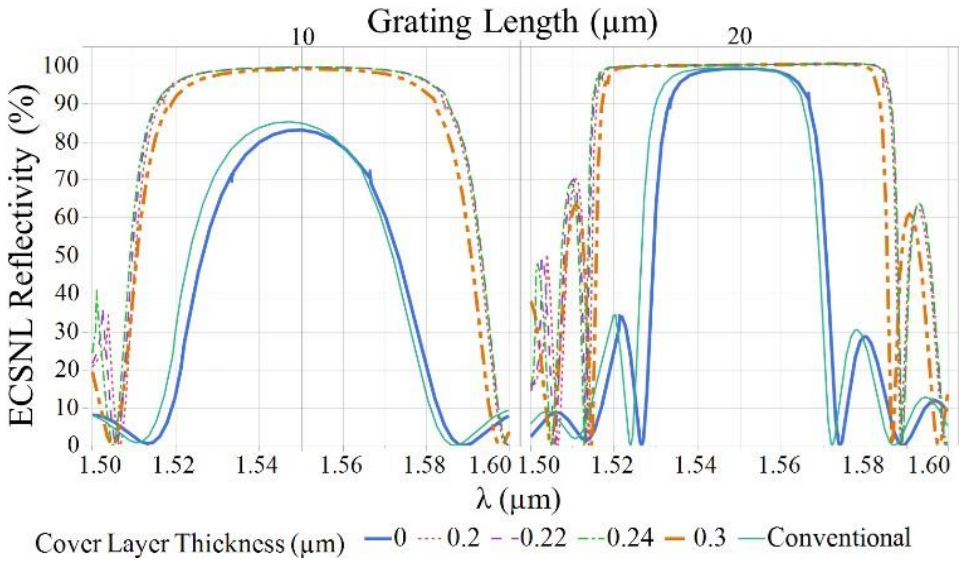

Figure 17 Reflection verses wavelength at different cover layer thicknesses compared to conventional gratings

2.3.2 Variations in the Duty Cycle

In Figure 18, we fix the grating etch depth to 0.1 μm, the grating length to 10 μm, and vary the duty cycle from 5% to 95%. The normalized attenuation is maximum at the 60% duty cycle and 200 nm cover layer combination. At shorter wavelengths and thicker cover layers, higher order modes can be supported, visualized in the α/ko plot for these conditions. The plot gives the

normalized effective index ß/ko and normalized attenuation α/ko as a function of wavelength for different duty cycles and different cover layer thicknesses. For cases with cover layer thickness of 0 and 0.1 µm, the gratings start to radiate at wavelengths shorter than ~ 1.52 µm, but if the cover layer is too thick, undesired higher order modes are supported. As a result, additional first-order Bragg resonances can occur at shorter wavelengths for a cover layer thickness of 0.2 µm.

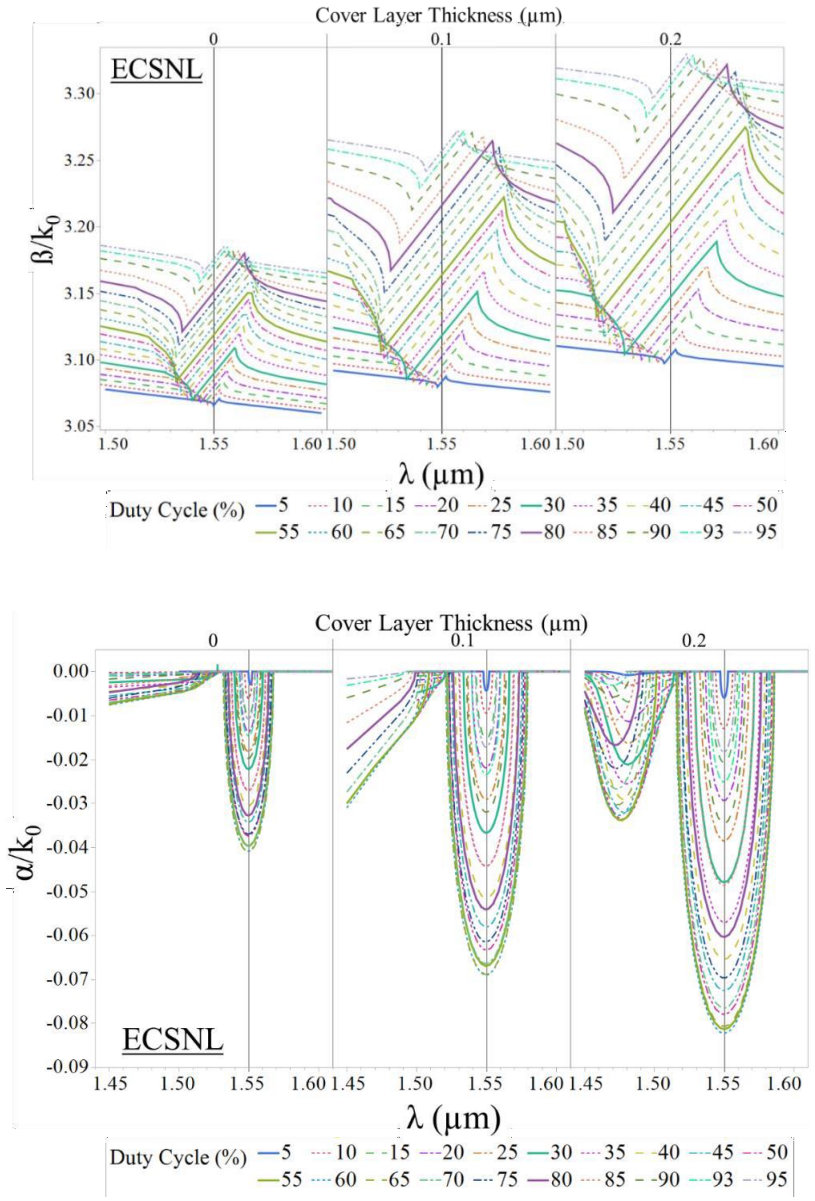

Figure 18 β/k0 (top) and α/k0 (bottom) as a function of wavelength for ECSNL structures for wide range of duty cycles for 0, 0.1, and 0.2 µm cover layer thicknesses.

Next, we examine the influence of grating length. Figure 19 shows that at duty cycles in the 50-60% range very high reflectivity and wide FWHM can be achieved for a short 10 μm long grating. The spectral width significantly increases as the cover layer increases.

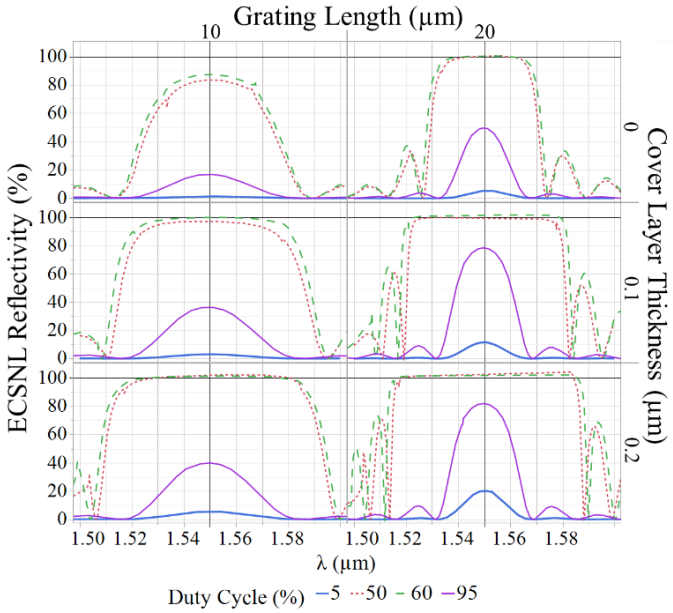

(b)

Figure 19 Plot of Reflectivity as a function of wavelength for specific duty cycles analyzed at various cover layer thicknesses for different grating lengths for the a) ECSL and b) ECSNL grating structure.

2.3.3 Variations in the grating depth

Next, we examine the simulations at gratings depth of 50, 100, and 150 nm. Figure 20 shows the real and imaginary parts of the normalized complex effective indices β/ko and α/ko verses wavelength. A cover layer of 200 nm produced the maximum normalized attenuation values. In Figure 21, a 200 nm cover layer and 100 nm etch depth gratings are used. The summation of transmission, reflection, up, and down power should equal 100% for all wavelength in the

chosen range. Clearly, the summed power does not equal 100% in the shorter wavelength region. This is explained by understanding that the SMU developed software used in this simulation is not able to process TE_0-TE_0 and TE_1-TE_0 coupling simultaneously (TE_1-TE_0 resonance at ~1.46 microns).

As grating depth increases to 150 nm in the ECSNL structure encroachment on the TE_0-TE_0 resonance from the TE_1 -TE_0 progresses when the cover layer thickness is 0.2 microns until they overlap

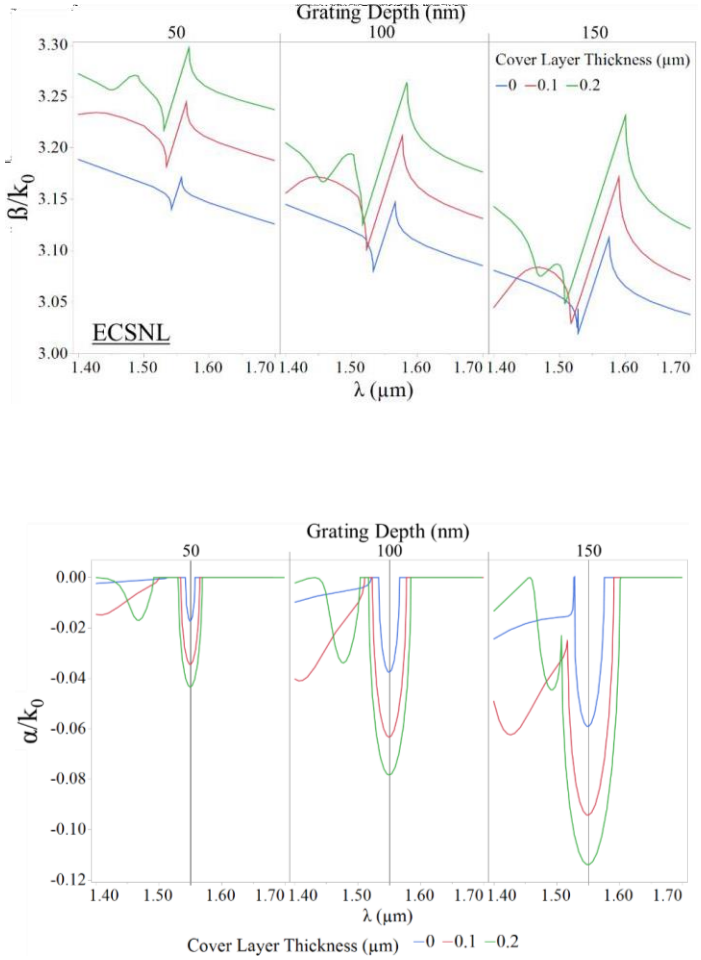

Figure 20 Plots of the normalized complex effective index as a function of wavelength for an ECSL (a & b) and an ECSNL (c & d) structures for various grating depths with cover layer thicknesses of 0 (blue), 0.1 (red), and 0.2 (green) microns at a 50% duty cycle.

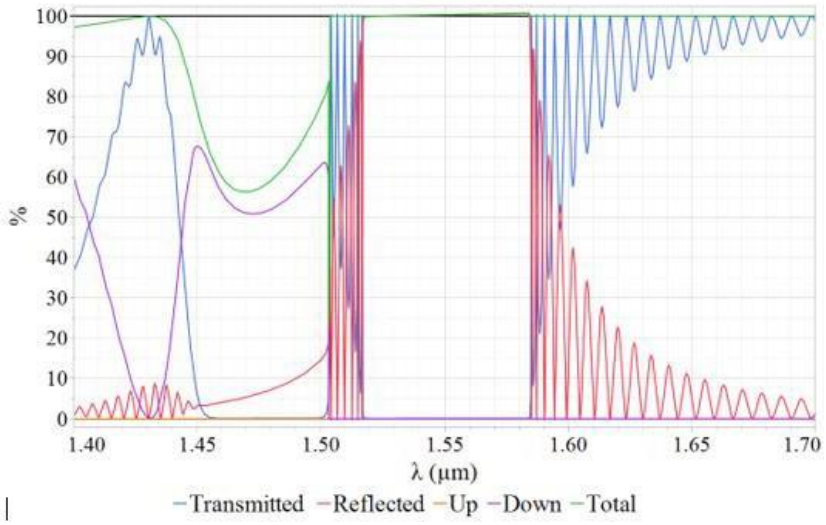

Figure 21 Plot calculating power of light Reflected (red), Transmitted (blue), radiated Upward (orange), radiated Downward (purple), and Total radiated power (green) with a grating depth of 100 nm, and a 0.2 μm cover layer

2.4 2nd Order Out-couplers

Studying out-couplers includes the goal of determining what percentage of power is being reflected back to the light source, absorbed, transmitted through the device, transmitted in the upwards direction, or transmitted in the downward direction (into the substrate) [39]. With a few changes in the epitaxial design and processing, one can choose to design the transmitter to couple light into a fiber optic on the epitaxial side of the device, or choose to collect the light from the back side of the wafer (as illustrated in Figure 2). If we choose to operate near the second Bragg condition for the 2nd order gratings, the attenuation constant will approach zero, as shown in Figure 22 [40]. If we assume an optical waveguide with no material loss, the near 2nd order condition will produce two pairs of modes, denoted as Mode I and II, and Mode III and IV. A 2nd order out-

coupler is designed such that the scattering centers have a period close to the period of the longitudinal propagation constant of the mode, thereby insuring the out-coupling light direction is near-perpendicular to the direction of the waveguide. This paper [40] shows stable numerical solutions for the modes of periodic dielectric structures developed by Floquet-Bloch theory. This paper argues that if we could fabricate a waveguide with an infinitely long 2nd order grating to atomic level precision, that is, perfect thickness, material composition, smoothness, and periodicity, we would not achieve out-coupling at the exact Bragg condition. In practice, fabricated out-couplers (finite length) have shown to efficiently outcouple power in the "up" direction, making them useful for coupling into fiber optics or to enable wafer-level testing [41].

With the same approach as discussed in the 1st grating section of this chapter (the bottom drawing of Figure 13), a simplified structure will be used to understand the parameter space for duty cycle and cover layer thickness variations. The analysis will assume that the grating teeth are square and the grating depth is fixed at 0.1 microns. The simulation software allows for non-square gratings, but as shown in Figure 34, a Scanning Electron Microscope (SEM) image of fabricated gratings during this thesis work, square is a good approximation.

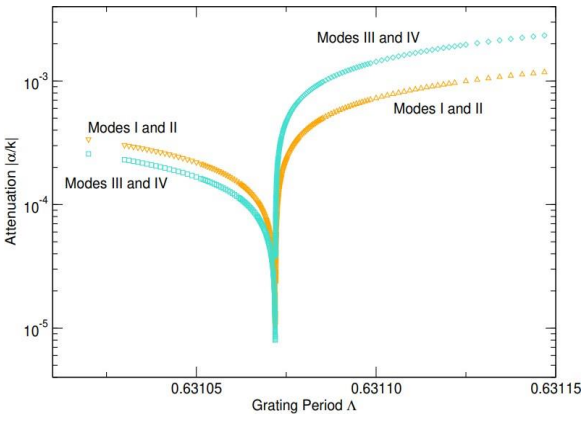

Figure 22 Log Attenuation verses Grating Period showing the attenuation approaching zero At the exact 2nd Bragg condition [40].

As with the case of the first order gratings, focus is on the ECSNL (no liner) case since this is the approach used for the fabrication of the devices for this thesis work. Figure 23 shows α/k_0 (imaginary part of the effective index) and β/k_0 as a function of λ where the exact 2nd order condition is set to $\lambda \sim 1.55 \mu m$. As the cover layer thickness increases, the out-coupler becomes more efficient.

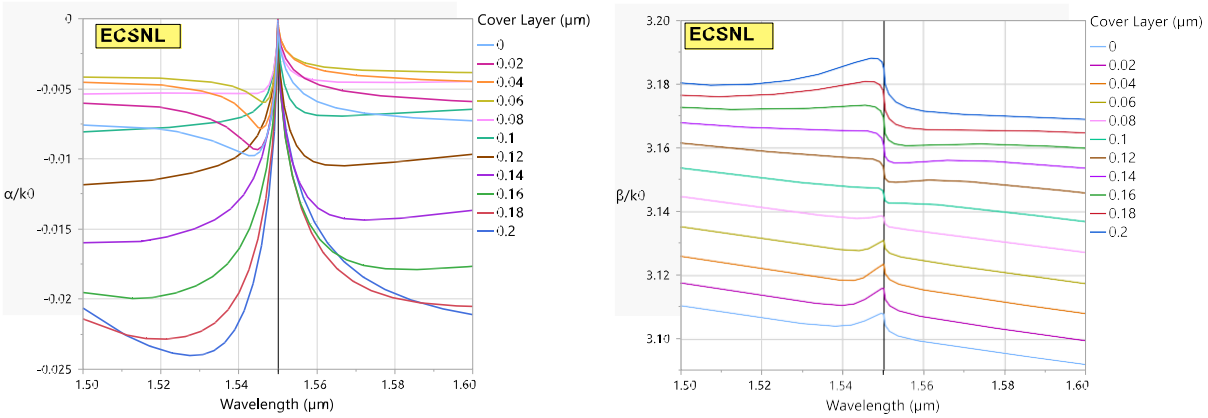

Figure 23 α/k_0 and β/k_0 as a function of λ and cover layer thickness where the exact 2nd order condition is set to $\lambda \sim 1.55 \mu m$

Figure 24 shows duty cycle variations from 5% to 95% for the ECSL structure. Increasing the cover layer thickness increases the propagation constants and lowers the attenuation (Figure 25). The attention is minimized at around 50 % duty cycle, but 50% duty cycle may not be the best condition for a high propagation constant. But in terms of outcoupled power, for both 0.1 and 0.2 μm cover layer thicknesses, near 50% duty cycle appears ideal (Figure 24).

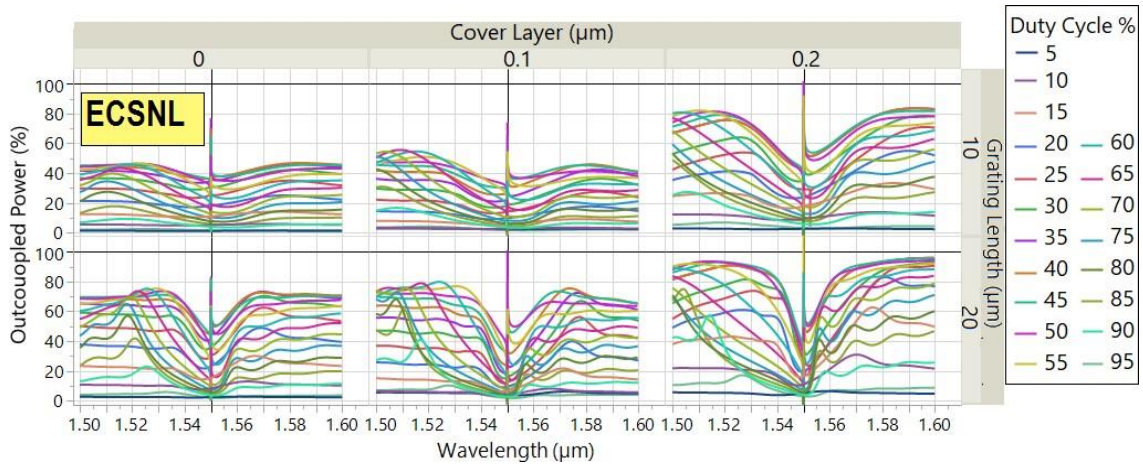

Figure 24 Outcoupled power as a function of wavelength, cover layer thickness, and duty cycle

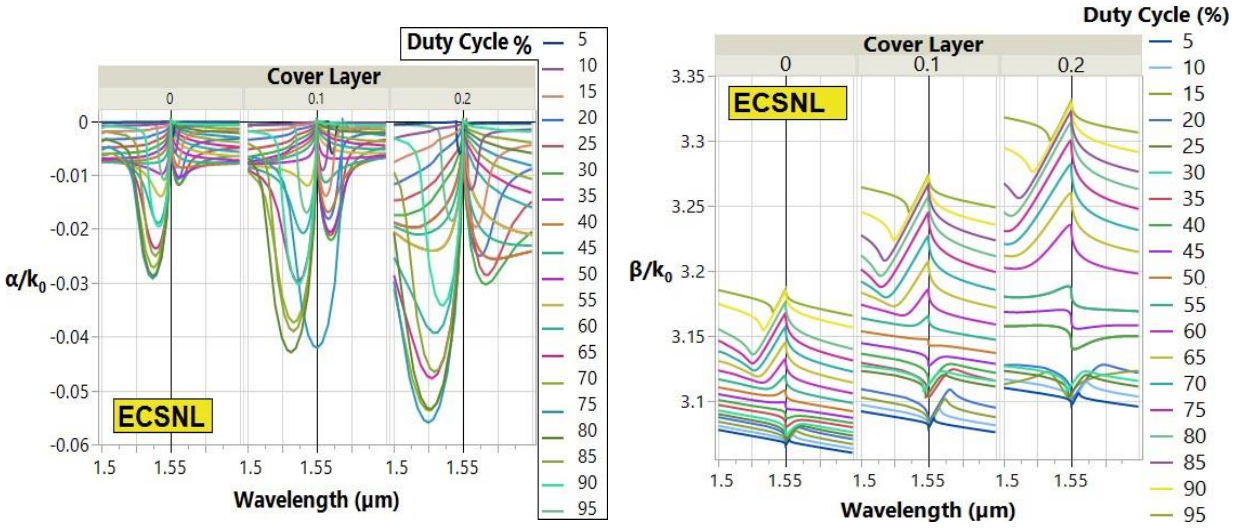

Figure 25 α/k_0 and β/k_0 as a function of λ, cover layer, thickness, and duty cycle variations

An efficient out-coupler will outcouple most of the light and have minimal reflected power at the operating wavelengths of the device. Figure 26 shows that around 50% duty cycle, we get the maximum outcoupling and the minimum in reflectivity. For the 10 μm long grating and 0.2 μm thick cover layer, an ~ 70% outcoupling power is achieved from duty cycles from about 30-

65 %. The 20 μm long gratings achieves close to 90% outcoupling at 40% DC. The fact that a wide variation of duty cycle and cover layer thickness produce efficient out-couplers helps ensure that the device is manufacturable, as it is difficult to fabricate gratings at an exact duty cycle and deposit cover layers with exact thickness.

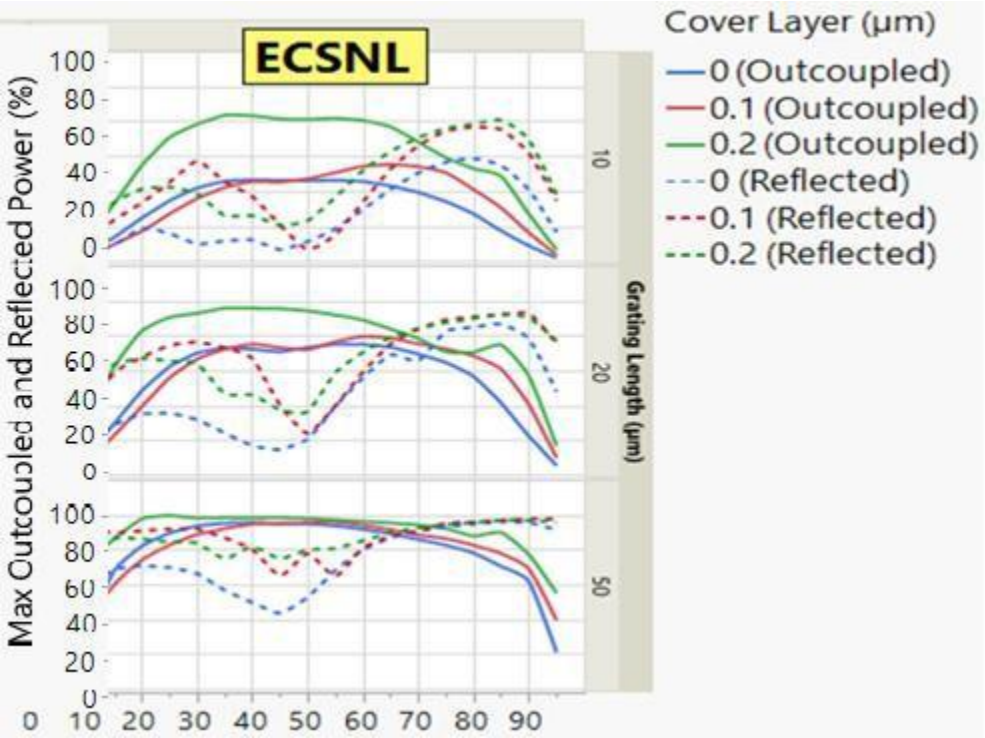

Figure 26 Max Outcoupled and Reflected Power as a function of duty cycle for various grating lengths and cover layer thicknesses

Simulations of this basic structure, varying the duty cycle, cover layer thickness, and fixing the out-coupler length at 10 µm, resulted in an optimized out-coupler with 50% DC and 0.18 µm cover layer thickness. Figure 27 shows the power percentages of such as structure. Note that the total power (transmitted + reflected + up + down) is close to 100% for wavelengths from about 1.53 to 1.6 µm. These are the out-coupler parameters that will be used as the starting point for the full-loop fabricated MQW transmitter device.

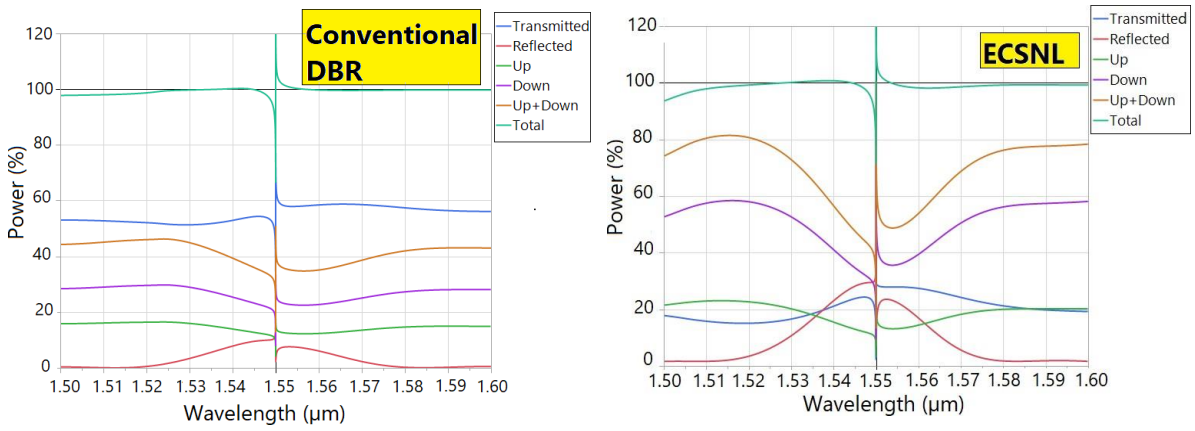

Figure 27 A conventional DBR (left) and ECSNL (right) comparison of Power % as a function of wavelength for Transmitted, Reflective, Up, Down, and Total power.

CHAPTER 3

3.1 Integrated Device Design

Today, the two most commercially viable deposition techniques for growing III/V laser epitaxial multi-quantum well laser structures are with molecular beam epitaxy (MBE) and metalorganic chemical vapor deposition (MOCVD). From a technical point of view, choosing the best growth technique is based on the precise details of the structure and application. Commercially, the choice is impacted by the cost for each technique and the specific capacity profile inherent to a specific product type [42]. General comparative information for MBE and MOCVD are:

- Monolayer deposition for super lattices and quantum wells is possible by both techniques with good precision. In MOCVD reactant gases are fed into the system at high pressure (~ 1 Torr) whereas MBE pressures are below 10^{-8} Torr. For MBE, this condition ensures a molecular regime, as opposed to a viscous one for MOCVD, that is characterized by atoms and molecules not interacting with each other. This enables MBE to use mechanical beam shutters to switch the beams on and off, precisely controlling composition and ensuring abrupt interfaces. The viscous flow of the relatively high pressure MOCVD tools produces boundary layers on the wafer surface that also limits the ability to form abrupt interfaces.
- For many applications, MBE has superior film thickness controls (fraction of monolayers), and better composition control. The ultra-high vacuum level requirement of MBE increases the cost of operation, although the cost of materials for MOCVD is typically higher.

- MOCVD has higher growth rate and more commercially viable for most laser diode manufacturing applications.

For MBE, the substrate and source materials are independently heated in a precise and uniform manner. The mean free path of the source gaseous atoms or molecules are very long due to the very low chamber pressures. The molecules condense on the wafer and arrange themselves in monolayers that can be precisely controlled. A schematic of a generic MBE reactor is shown in Figure 28 [43] where in this case, there are four effusion cells, each with its own mechanical shutter. MBE process tools typically have in-growth material characterization metrology such as electron guns and lasers to ensure the precise composition and thickness of layers.

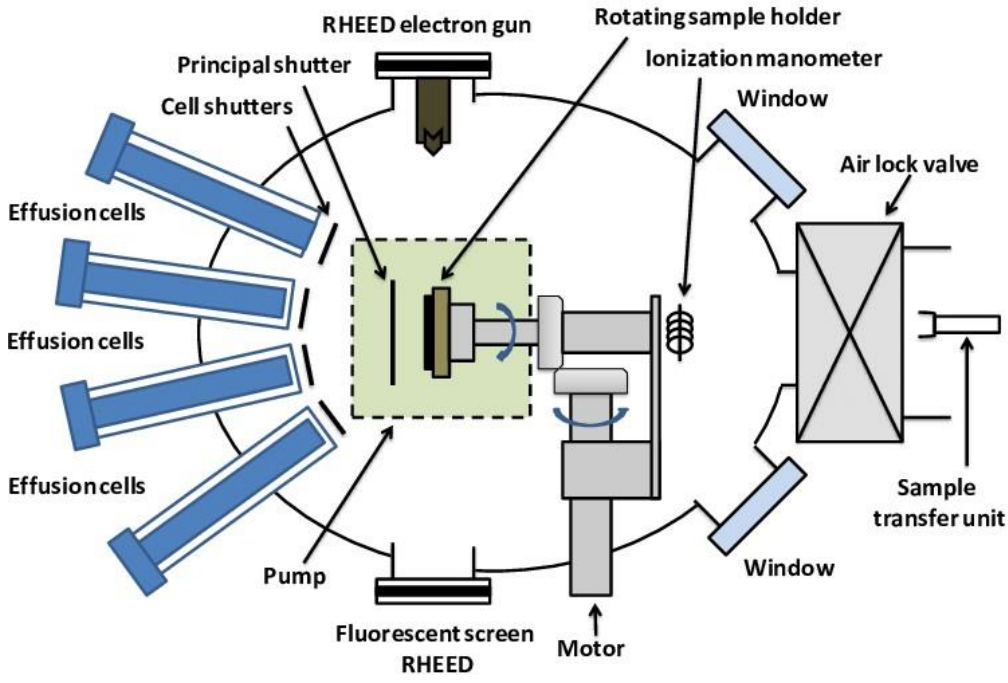

Figure 28 Schematic of an MBE deposition tool with 4 effusion cells [43]

The laser structures for the funded DOE and NASA work for this thesis was grown by MBE on 3-inch InP substrates. Typical growth runs would include 11 wafers, and there are some measured differences in photoluminescence (PL) in intensity and wavelength uniformity from the outer and inner rings. Since effective QWs in QW lasers must be of precisely controlled nano-thickness layers, the MBE and MOCVD techniques require layer by layer control of the grown crystals. Semiconductor QW lasers offer several advantages over non-QW semiconductor layers, such as a reduction in threshold current, ability to tune wavelength by layer thickness rather than relying on the bandgap of the material, extending the wavelength range and operating temperature range [44].

The initial NASA funded work was to target a transmitter with a 1550 nm lasing wavelength, and this was followed by DOE funding to target a 1310 nm device, then a 1550 nm approach for NASA I thought our initial was 1550 at NASA, followed by 1310 DOE and then 1550 nm at NASA. The methodology to arrive at a starting point for the epitaxial design is described in [45], where the design and characterization of a 1.3 μm AlGaInAs-InP MQW laser is described. The design began by leveraging an existing structure for a laser-EAM device [46]. Figure 29 shows the index by depth in the epitaxial growth, revealing an 11-QW design implementing an AlInGaAs/InP material system.

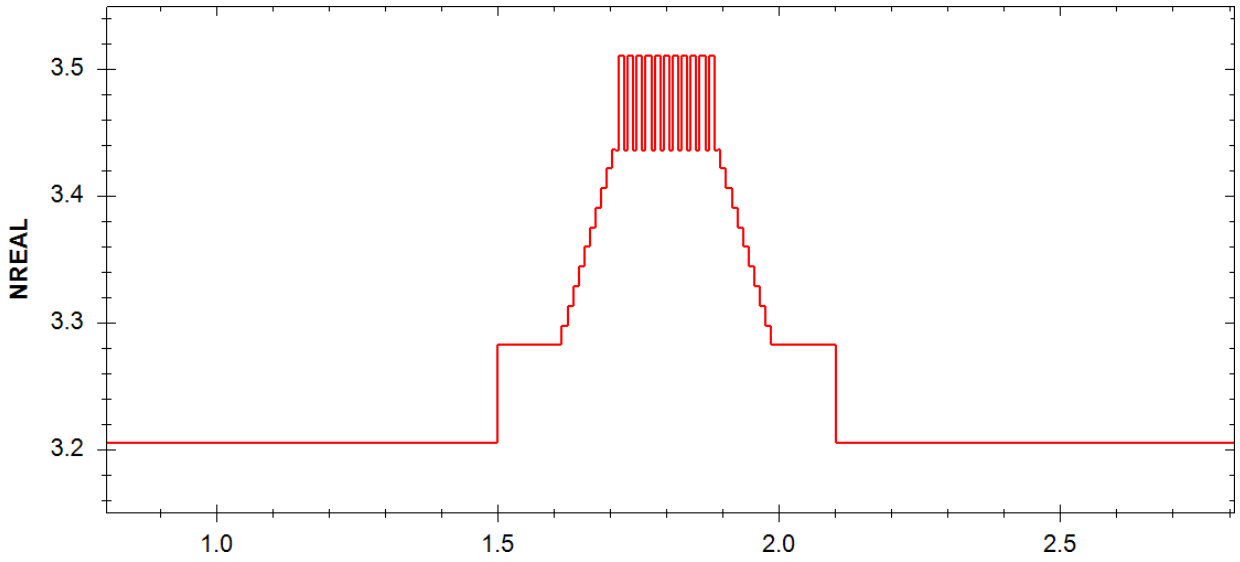

Figure 29 Initial AlInGaAs/InP-based Laser structure

HAROLD commercial software was used to help determine the needed layer thicknesses and material compositions for the design requirements. Table 1 details the resulting epi-stack with 11-QW and using a separate confinement heterostructure (SCH). Appendix B provides the 15xx nm epi-stack that was designed and grown for the second phase of this thesis work. Etch stop layers are grown to make the fabrication of the devices easier (need selectivity between wet and dry etches of the various epitaxial layers). In optimizing the design to achieve the targeted grating reflectivity, the QWs are intentionally off-centered in the SCH layers. An InP sacrificial layer was grown on the p-contact (cap) layer to protect the cap during wafer fabrication and is removed before metallization.

Table 1 Complete epitaxial structure for 1310 nm Laser-EAM Transmitter

Layer		Material Composition	Thickness (Å)	Material Index
25	Sacrificial	InP	500	3.20315
24	Cap	$In_{0.533}Ga_{0.467}As$	1000	3.55187
23		$In_{0.533}$ $Ga_{0.467}As$ to InP	500	3.41879
22	P-clad	InP	5000	3.20367

21		InP	3500	3.20328
20	Etch Stop	$In_{0.977}Ga_{0.023}As_{0.95}P_{0.05}$ to $In_{0.863}Ga_{0.137}As_{0.7}P_{0.3}$	50	3.30515
19		$In_{0.863}Ga_{0.137}As_{0.7}P_{0.3}$	100	3.34056
18		$In_{0.863}Ga_{0.137}As_{0.7}P_{0.3}$ to $In_{0.977}Ga_{0.023}As_{0.95}P_{0.05}$	50	3.30515
17	P-spacer	InP	500	3.20315
16	P-GRIN	$In_{0.526}Al_{0.406}Ga_{0.068}As$ to $In_{0.525}Al_{0.475}As$	100	3.30879
15		$In_{0.525}Al_{0.475}As$	20	3.35846
14		$In_{0.525}Al_{0.475}As$ to $In_{0.529}Al_{0.268}Ga_{0.203}As$	80	3.35849
13	SCH	$In_{0.529}Al_{0.268}Ga_{0.203}As$	1500	3.43238
12			500	3.43238
11			220	3.43238
10			30	3.43238
9	Barrier	$In_{0.433}Al_{0.267}Ga_{0.3}As$	60	3.43096
8	QW (x11)	$In_{0.625}Al_{0.205}Ga_{0.17}As$	100	3.50378
7	Barrier (x11)	$In_{0.433}Al_{0.267}Ga_{0.3}As$	60	3.43096
6	SCH	$In_{0.529}Al_{0.268}Ga_{0.203}As$	30	3.43238
5			220	3.43238
4	N-GRIN	$In_{0.529}Al_{0.268}Ga_{0.203}As$ to $In_{0.525}Al_{0.475}As$	250	3.35606
3		$In_{0.525}Al_{0.475}As$	100	3.32553
2		$In_{0.525}Al_{0.475}As$ to $In_{0.526}Al_{0.406}Ga_{0.068}As$	100	3.30876
1		InP	10000	3.20315
Substrate		InP	--	3.20315

The laser ridge intending to propagate single modes and using this material system, requires a lateral index step, Δn, of approximately 0.015 +/- 0.005. An important design parameter for this is the thickness of the p-spacer (layer 17).

Harold – A hetero-structure laser diode model simulation software from Photon Design was used to optimize the epitaxial design for this thesis. Since the identical epitaxy is used for both the laser gain section and the modulator section, Harold was very useful in the task of determining a design that simultaneously met the performance specifications of both sections. That is, there is a compromise in simultaneously designing for an efficient laser gain section and an EAM that efficiently absorbs and transmits at modest voltage changes over the intended operating temperatures. Harold allows the user to specify the layer thickness, material, alloy composition, and doping levels and to define the periodical MQW layers. All of the epitaxial

sections identified in Table 1 are defined in the simulation model, which includes metal/heatsink layer, substrate layers, bulk layers, QW, and barrier layers. MQW structures can be modelled by determining the energy levels by solving the Schrödinger equation and solved over the whole MQW region to account for coupling between wells. For the EAM, Harold can calculate electron, light-hole and heavy-hole eigenvalues and eigenfunctions in the quantum-wells.

3.1.1 Simulations of the 11-QW full epitaxial stack

With the epitaxial design fixed, simulations are used to determine where the top and bottom of the gratings should reside to achieve the reflectivity and bandwidth specifications of the reflectors. For the outcoupling specifications for the 2nd order out-couplers, the design goal is to couple as much as the available power as possible into a single mode fiber. Additionally, simulations are used to ensure mode matching between device sections.

Simulations will produce α/k_0 or $\alpha\Lambda$ and β/k_0 or $\beta\Lambda$ as a function of $k_0\Lambda$ plots and power as a function of wavelength plots. The purpose is to learn enough to be able to create the mask design and process flow, knowing where in the process flow to begin etching the gratings and how deep to etch them, and what material choices we have for the gratings engineering and transition areas between the device sections. The epitaxial design needs to consider how the device will be processed, such as inserted etch stop layers for wet etching steps.

With the requirement to maintain single transverse mode propagation through all sections of laser, EAM, gratings, and the transition waveguiding to connect these sections, we need to methodically exam the field profiles of these various sections. The design goal is to minimize power losses between to device sections. To do this, we need to perform intensity overlap integral analysis:

$$\kappa_x = \frac{\left|\int_{-\infty}^{\infty} E_g(x)E_w^*(x)dx\right|^2}{\left(\int_{-\infty}^{\infty} E_g(x)E_g^*(x)dx \int_{-\infty}^{\infty} E_w(x)E_w^*(x)dx\right)} \quad (26)$$

$$\kappa_y = \frac{\left|\int_{-\infty}^{\infty} E_g(y)E_w^*(y)dy\right|^2}{\left(\int_{-\infty}^{\infty} E_g(y)E_g^*(y)dy \int_{-\infty}^{\infty} E_w(y)E_w^*(y)dy\right)} \quad (27)$$

Where κ is the overlap integral of the modes Eg and Ew in the y and x directions (refer to Figure 8 for the coordinate system). The goal is to choose materials and process deposition/etch techniques that provide a controllable index of refraction and film thickness to enable κ to approach a value of unity.

For the laser ridge, we have a narrow window of possible lateral indices due to the need for a sufficiently high lateral index to compensate for gain-induced index suppression but not too high as to permit high order modes. The p-spacer in Table 1 largely determines the lateral index step, designed at about 0.0137 (3.3632 for the effective index of the ridge – 3.3495 for the area just laterally outside of the laser ridge). Device processing includes defining the laser ridge and EAM by dry and wet etching and using Si_3N_4, amorphous silicon, low refractive index spin-on-glass, and BCB materials to build the device illustrated in Figure 3. It is instructive to visualize the cross-section of these Laser/EAM, connecting waveguides, and the DBR gratings sections with their respective resulting lateral (y-direction) mode profile. For the waveguide connecting sections shown in Figure 30, the lateral index step in very sensitive to the amorphous silicon thickness, where calculations show that the lateral index step is 0.0055 (assuming there is no silicon layer in this region). The goal is to then match the lateral index of the connecting regions to that of the grating regions. Calculations show that the lateral index of the grating region is quite sensitive to the silicon thickness, such that with no silicon, the index step is about 0.003 at

100 nm, 0.002 at 150 nm, and providing the matched index step of 0.0055 at a thickness of 225 nm. Therefore, 225 nm silicon thickness was used when fabricating the devices.

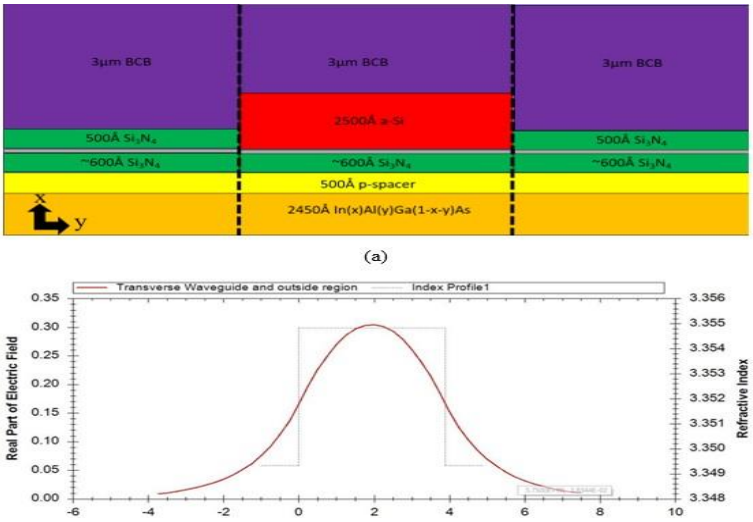

Laser/EAM Waveguide cross-section drawing and resulting lateral (y-direction) mode profile

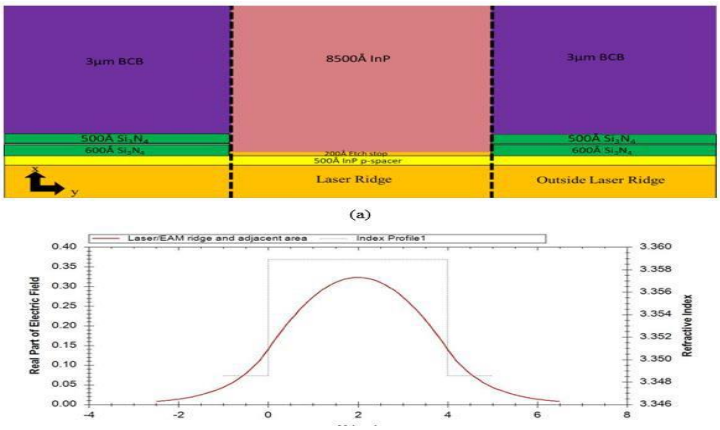

Connecting waveguides cross-section drawing and resulting lateral (y-direction) mode profile, with 2500 Å e-beam deposited amorphous silicon and 1000 Å deep gratings.

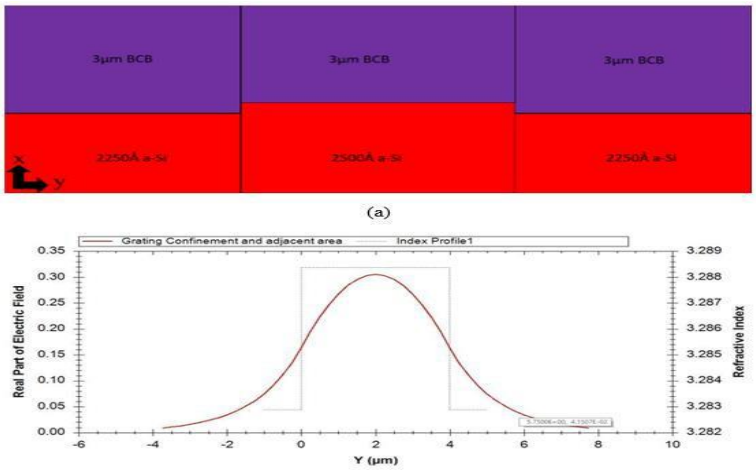

DBR gratings region cross-section drawing and resulting lateral (y-direction) mode profile

Figure 30 Cross-section diagrams for the waveguide connecting regions

The intensity overlaps for the vertical (x) and horizontal (y) for the device sections are provided in Table 2.

Table 2 Waveguide Intensity Overlap Values

Waveguide Junction	κ_x	κ_y
The Laser/EAM Ridge section to the connecting waveguide	0.9902	0.986
The connecting waveguide section to the DBR Gratings	0.927	0.9994

3.1.2 Device architecture

The DOE supported the initial work for this thesis [2], with the goal of designing, fabricating, and testing a 100 Gbps Radiation Tolerant Optical Transceiver. Because of the relative maturity of silicon-based semiconductor design and manufacturing, the knowledge base is much greater for designing for radiation tolerance and compared to III/V devices [47]. For III/V based opto-devices, in general, gamma radiation (ionizing radiation) is not an issue but neutron and proton

radiation (particle) cause significant increases in laser threshold [48,49]. The light output of a laser diode is directly related to the recombination rate or, alternatively, the lifetime of the excess minority carriers. If the light emission originates on the p-side of the laser diode junction, then the minority carriers are electrons. Lifetime damage [50] can be described by

$$\frac{\tau_0}{\tau} = 1 + \tau_0 K\Phi \qquad (28)$$

τ_0 is the pre-irradiation value of the minority carrier lifetime

τ is the post-irradiation lifetime value

K is a damage constant in cm^2, Φ is the radiation fluence in cm^{-2}

The increase in the threshold current due to radiation is proportional to $\tau_0 K\Phi$

$1/\tau_0 K$ can be interpreted as a threshold fluence at which a shift in threshold current becomes noticeable. The high-energy photons of gamma rays and x-rays are types of ionization radiation, and energetic neutrons are examples of particle radiation. By and large, the main effect of ionization in materials is the production of electron-hole pairs, and the primary mechanism of particle radiation is atomic displacement. Reported results for MQW laser diodes are complicated by annealing effects, how or if the devices are biased during the radiation, and material choices in the active region. For example, Al containing quaternary layers may influence the radiation tolerance [51].

A summary of the Sandia National Labs report [52] is given below

• The major effect of irradiation on laser diodes is the increase in threshold current density, Jth, through the creation of nonradiative recombination centers that compete with radiative recombination sites.

• Gamma irradiation does not cause major problems at doses lower than 107-108 rads, especially if the irradiation is carried out under lasing conditions.

• Annealing of gamma radiation effects occurs 1) over time at room temperature, 2) at elevated temperatures, and 3) in response to lasing.

• Very high dose rates of ionizing radiation (10^{11}-10^{12} rad·s-1) can adversely affect the electrical properties of laser diodes. These effects can be mitigated by shielding.

• Neutron irradiation causes significant damage in laser diodes at doses higher than 10^{13}-10^{14} $n \cdot cm^{-2}$.

• Partial annealing of neutron damage can be achieved by operating in lasing mode after irradiation. Thermal annealing occurs at moderately elevated temperatures.

• To minimize radiation effects, a laser diode should have a low threshold current and a very high maximum operating current.

Many aspects of the design of the devices in this thesis work tend to increase radiation tolerance; 1) low threshold currents so that the difference between Jth and the maximum current is large 2) minimal dependence on temperature 3) low minority carrier lifetimes (Lasers and EAMs have very different carrier lifetimes) 4) and short cavity lengths.

3.2 Photolithography Mask Design

Mask design used Klayout software and the set of 5-inch photomasks were fabricated by Photosciences, Inc. A GCA Autostep 200 I-line stepper lithography system was used for all photolithography steps except to define the gratings. Figure 31 shows the mask layout of one

of the devices on the left and a micrograph of a fabricated device on the right. This device does not include the out-coupler section.

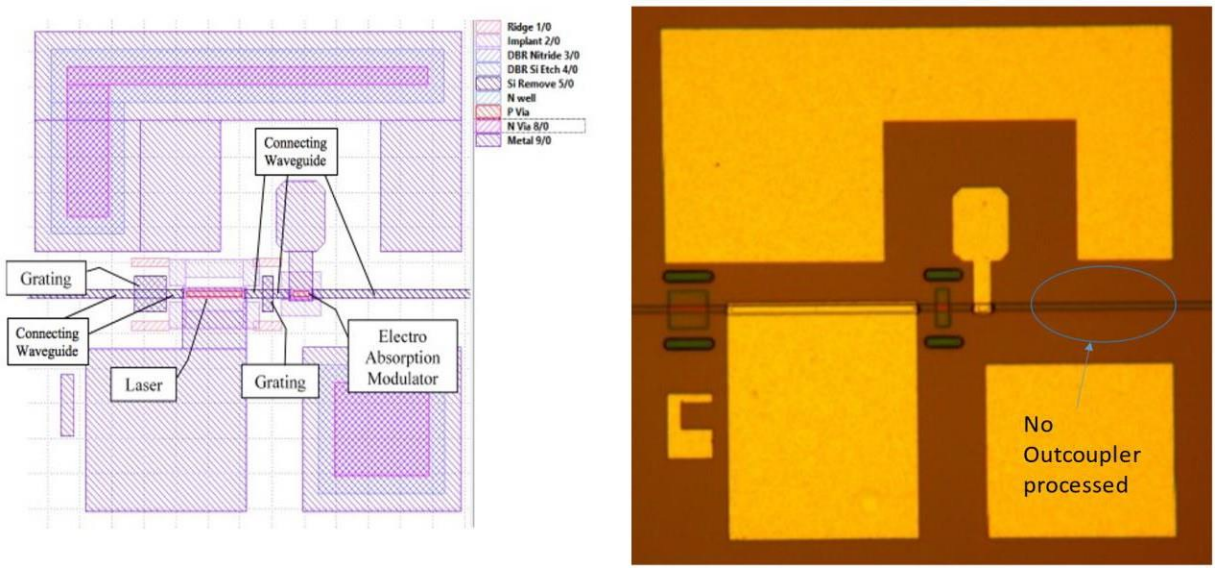

Figure 31 Mask layout of a single device (Left) and partially fabricated device (right)

The mask set included variations in laser length, EAM length, grating lengths, and ridge widths. Another process variable that was determined by processing is the exact location of the gratings in the epitaxial stack. Two cases that were explored during device fabrication is Case 6 and Case 8. Table 3 provides the mask variations and the details of the two Cases.

Table 3 Photolithography mask variations and gratings positions

Row	Ridge width μm	Laser length μm	EAM length μm	DBR rear μm	DBR front μm
1	4.5	150	20	16,23	5,10
2	3.5	150	20	16,23	5,10
3	4.5	75	20	14,30	6,12

4	4.5	150	15	16,23	5,10
5	3.5	150	15	16,23	5,10
6	3.5	75	20	14,30	6,12
Grating Cases	Grating position	Depth of gratings nm	Rear DBR lengths nm	Front DBR lengths nm	
Case 6	Bottom of layer 9	10	23/30	10/12	
	Top of layer 9	12	14/16	5/6	

Test structures for the purpose of measuring contact resistance and implant isolation were included in the mask, along with a large area photodiode. The mask layouts are shown in Figure 32. The cross-bridge structure is used for measuring the n-metal and p-metal contact resistance. For the p-metal, devices have a wide range of resistivity ρ_c**(Ω-cm²)**, from 3.75E-06 to 1.75E-08.

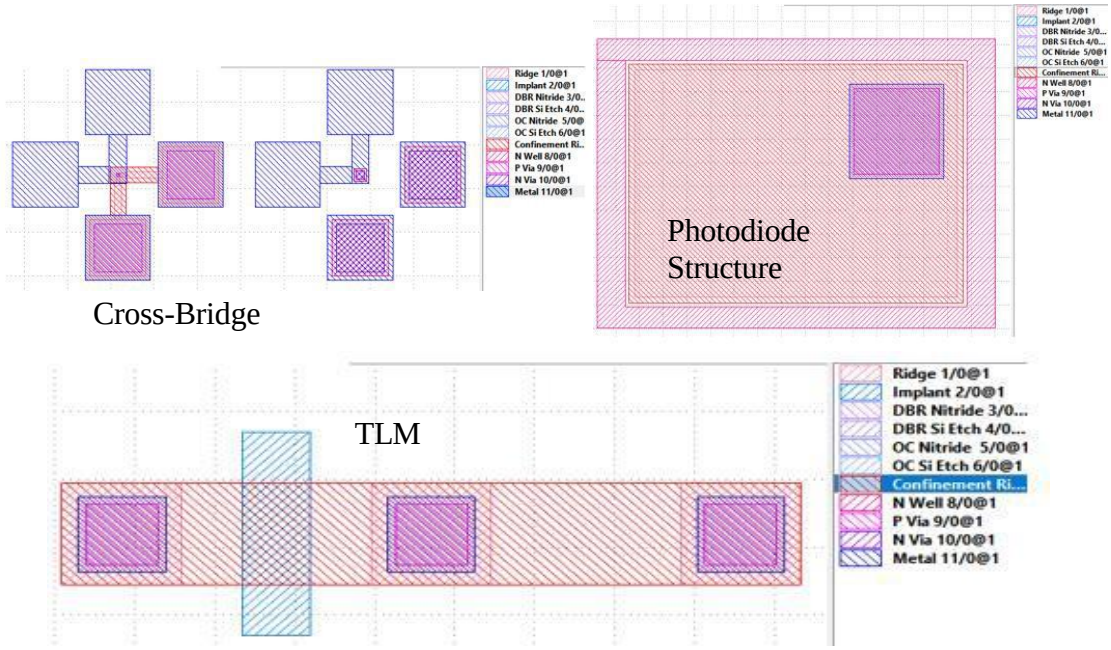

Figure 32 Test Structures

I-V curves of the fabricated photodiode are shown in Figure 33

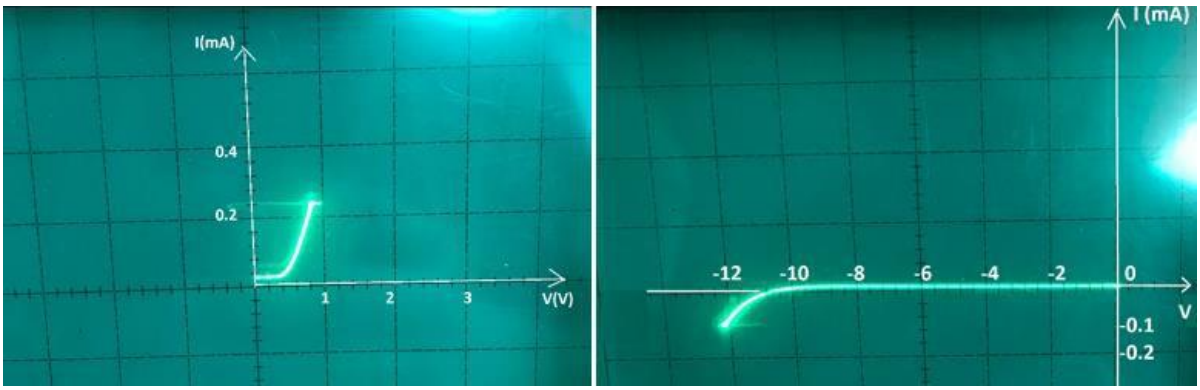

Figure 33 I-V curves of the fabricated photo detectors left) forward bias right) reverse bias

3.3 Fabricating Ridges and Gratings

Plasma etching is widely used to etch laser ridges, waveguides, and gratings in III/V compound materials. For laser ridges, process specifications are determined that ensure a controlled slope and critical dimensions, low surface damage, minimal notches or slope changes when etching through an EPI stack of varying compounds, smooth sidewalls, minimal trenching, and desired selectivity to the mask and remaining layer that is not intended to be etched. Early etch tool designs were capacitively-coupled and could not control the plasma (ion and electron) density independently of ion bombardment energy. Research accelerated in the 1980s – 1990s that led to commercially available etch tools and process recipes targeted for III/V manufacturing that employed High Density Plasma (HDP), and one particular design called Inductively Coupled Plasma (ICP) that is used to define the devices fabrication during this thesis work.

Relative to the possible ranges of plasmas, we are interested in weakly ionized (degree of ionization 10^{-6} – 10^{-1}), low pressure (0.1 mTorr±20 Torr), and cold (gas temperature around 300 K), [53,54,55]. A drawing of an ICP reactor is shown in Figure 34 [56], which shows the use of chlorine gas to etch silicon wafers.

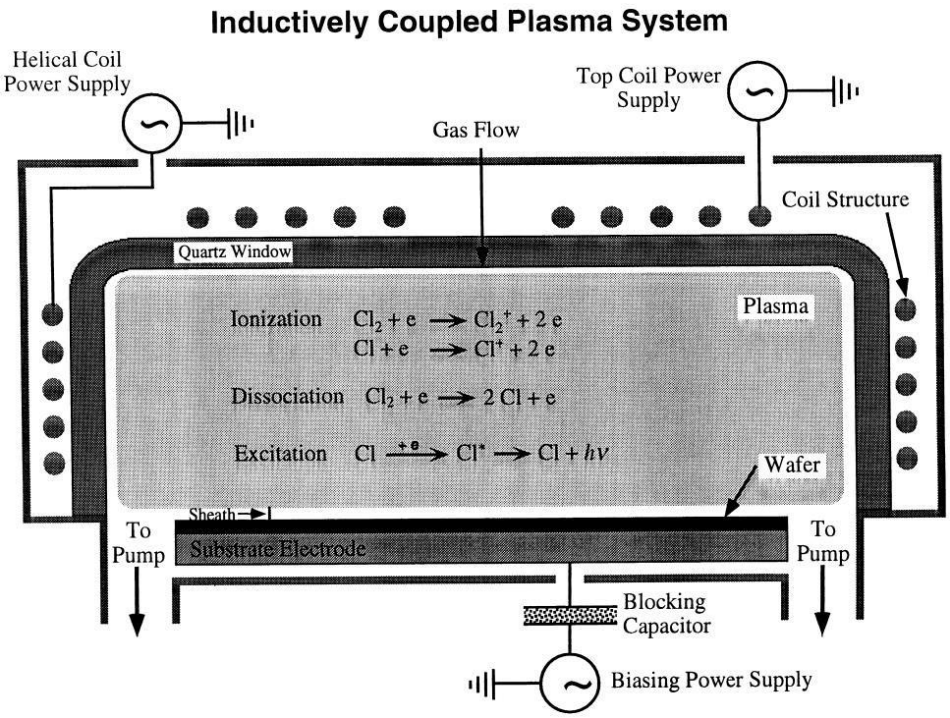

Figure 34 ICP etch diagram example with chorine gas [57]

Typically for RF etchers, the plasma is created by applying power at a frequency of 13.56 MHz to electrodes that interface with a low-pressure chamber of feedstock gas (in this case Cl_2) to create electrons, Cl radicals, Cl_2^+ ions. Radicals diffuse towards the wafer and are absorbed, and the ions are accelerated by the electric field. The key to this design is that "antenna coils" can control the ion density in the plasma (and hence the chemical component of the radicals/neutrals) independently of the second "biasing power supply" that accelerates the ions towards the sheath and wafer. The chamber flow gas is chosen very carefully so that a volatile etch product can be pumped out of the chamber, in this example, silicon is ultimately removed from the wafer by forming $SiCl_4$ and pumped out of the chamber.

To etch the waveguides in InP, InGaAs, InAlGaAs, GaAs, etc., of varying compositions and doping levels that meet all the specifications mentioned earlier, process chemistries that include combinations of Cl_2, N_2, CH_4, Ar, H_2, BCl_3, HBR, etc. have been developed [48]. For this thesis work, Cl_2/N_2 and CH_4/H_2 based chemistries were used to etch the ridges and gratings in the ICP etch configuration.

3.4 Photomask Layout, test structures, and process flow for UCSB/SMU processing

As discussed in section 3.11, the EPI structure was grown on 3-inch InP wafers. Because of the high cost of the EPI structure wafers and process tool limitations, initial work focused on processing on ¼ wafer sections that are compatible with process tools at SMU. With the knowledge gained from this work and additional funding from NASA, process work proceeded by processing on 3-inch wafers at the University of California Santa Barbara (UCSB) Nano-Fab facility, a facility with considerable capability to process 3 inch III/V wafers. This initial work at UCSB was performed by SMU graduate students, where short-loop devices were fabricated that enabled basic device testing that was instrumental in securing additional funding. The next phase was to contract a foundry service to fabricate the full-loop devices. Gratings development and the gratings for the initial funded work were fabricated by using the holography lab setup at SMU, shown in Figure 35. This system was developed at SMU and employs a DPSS 532 nm laser and frequency doubled to 266nm. The 5MHz linewidth, 60 M coherence length, > 200 mW power, and the use of bottom anti-reflection layers in the photolithography, enabled first order gratings useful for this work. SMU developed a novel dual mirror/prism approach that enabled uniform grating patterns over the 3-inch wafers. Typically, holographic gratings systems employ a corner mirror, located very near the wafer, to produce the interference holographic patterns, but

these systems suffer from significant period and duty cycle variation across a 3 or 4 inch wafer area.

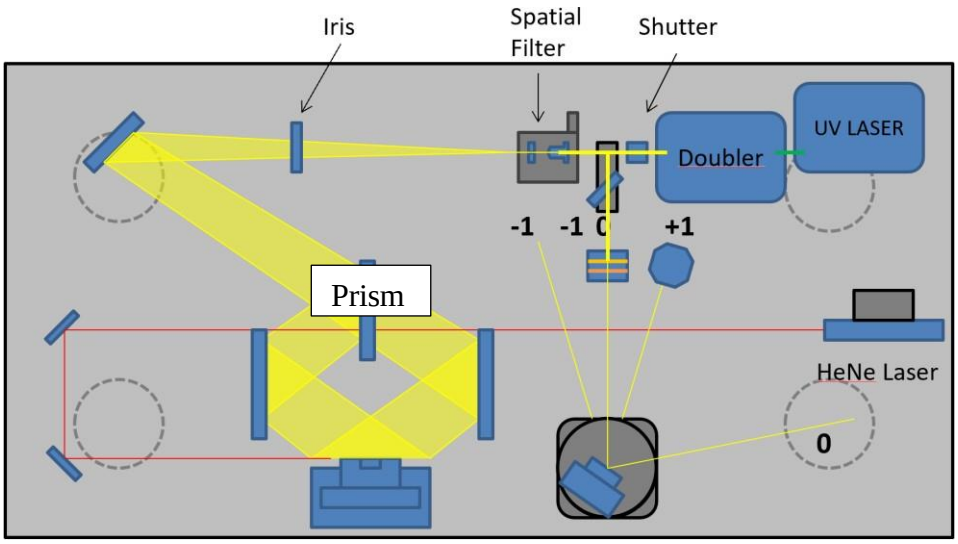

Figure 35 SMU Holography system for gratings fabrication

The process flow includes an ion implant step. This is necessary to electrically isolate the reverse biased EAM section from the forward biased laser section. SRIM software is used to design implant species/conditions making sure there are more vacancies than dopants. The SRIM libraries are limited for the relevant materials of the proposed device. The density of the material layers and proportion of elements are the most important factors in the model. An approach was taken to use averaging of material layer parameters to avoid interface effects in the model. Helium isolation implants in III/V based devices has been extensively investigated and has been used in production for VCSEL and other devices [58]. Leveraging this knowledge, simulations started by using a 7-degree implant angle, plotting the total vacancies, and using full damage cascades. The implant process was chosen to be performed as the next step after the laser and EAM ridges are dry and wet etched to the etch stop layer. A He implant dose of

$10^{13}/cm^2$ at 23 keV and 7-degree title angle will provide sufficient isolation. A diagram of the EAM ridge and epitaxial layers are shown in Figure 36. Implant simulation gives us confidence of protection of the ridges from implant damage if we have > 1.7 micron of photoresist on top of the ridges during the implant step. For this reason, we used a ~ 3 um thick photoresist to insure at least 1.7 microns on the ridge tops.

EAM Ridge Top

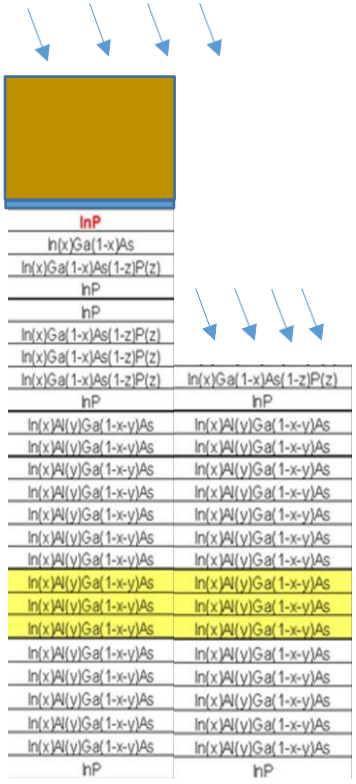

Figure 36 Diagram of implant mask and epi structure with 7-degree ion angle to surface

The fabrication of the proposed devices was challenging and required a learning curve. Early attempts were performed on ¼ wafer sections and primarily using the SMU cleanroom. The starting point for the process flow was to leverage existing process travelers developed by SMU for DBR laser fabrication. The 12 and 13 mask level process for the proposed device required process development and experience in BCB processing, spin on glass (SOG), lift-off

techniques, front side N-metal, and Ion Implant. Early attempts on ¼ wafer sections helped to establish these processes, realizing some key limitations available at SMU in process equipment and metrology for completion of the devices. Essential to continuing this work, we needed a stepper aligner for the photolithography. It was not possible to align the mask levels with the required accuracy with a contact mask aligner, for example, aligning the p-contact open mask to the laser ridges. Therefore, and for other reasons, we continued the work using the UCSB facility, where I-line steppers, III/V etch tools with laser endpoint systems, BCB processing modules, dielectric PECVD (plasma enhanced chemical) deposition tools, metrology, and the ability to process 3-inch wafers were available. In 2022, NASA funded a two-year SBIR Phase II effort that is leveraging III-V foundry services to complete the device processing. The process traveler provided in Appendix I was used for the NASA Phase I work.

The main process modules are described below with mask layout and corresponding SEM micrographs of processed devices

Ridge Etch

The laser and EAM ridges are fabricated by using silicon nitride mask and using a combination of methane/hydrogen dry etch and wet etch to the epitaxial etch stop layer. Figure 37 shows the ridge photomask pattern.

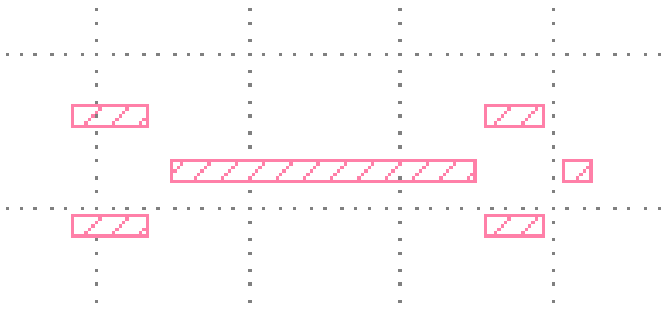

Figure 37 Photomask layout of the laser ridge

For the DOE phase I, the first step in the process was to cleave the 3-inch wafers into ¼ wafer sections. Next, a Plasma Enhanced Chemical Vapor Deposition (PECVD) with a SiH_4/N_2 process was used to deposit silicon nitride on the wafers to serve as an etch mask. Silicon nitride deposition at UCSB used a cyclical (changing RF frequency) NH_3/N_2/He PECVD process. This approach allows an additional process know to control film stress. After patterning the ridge, the non-masked nitride areas were etched with a CF_4/O_2 plasma etch process. At SMU the laser and EAM ridges were etched with a CH_4/H_2 process in a reactive ion etcher (RIE) to 80% of the total ridge height to the etch stop layer. At UCSB, a Cl_2/N_2 etch process in an inductively coupled plasma (ICP) was used. The remaining 20% of the ridge was wet etched and stopped on the etch stop layer using a 12:3:5 HCl:DI water: H_3PO_4 solution in an ice bath.

Ion Implant Step

Figure 38a shows the photomask layout of the laser ridge, EAM, and the ion implant regions, and Figure 38b shows a micrograph of a processed device at the ion implant step.

Figure 38 a) Photomask layout of laser ridge and ion implant mask b) Micrograph of processed device at the ion implant step.

In order to electrically isolate the EAM from the laser section, a selective He ion implant is used.

After patterning with ~ 2.7 µm thick resist, the clear areas in the micrograph will be exposed to the He implant with a dose of $5 \times 10^{13}/cm^2$ at 30 KeV at 7 degrees angle.(different than above?) The implant was

completed at an ion implantation facility foundry.

DBR Window

Silicon nitride is patterned such that the opening in the nitride defines the areas where the DBR gratings will be fabricated. Figure 39a shows the addition of the DBR window and Figure 39b shows a processed device. The white rectangular is after the window dielectric is opened.

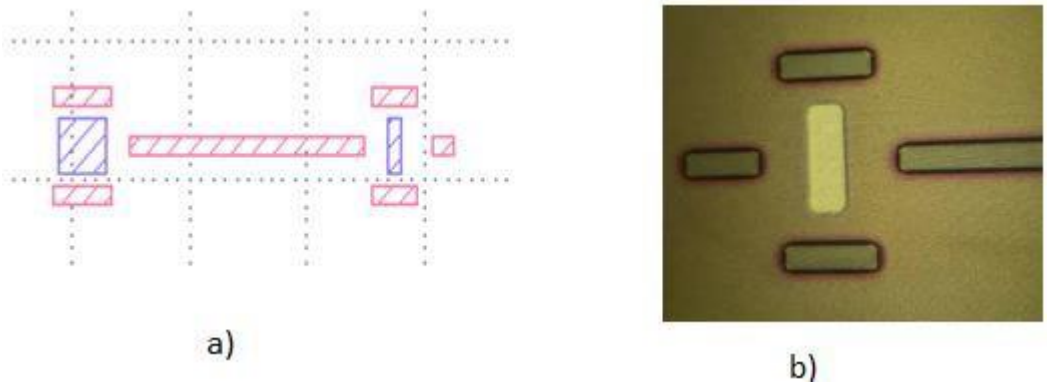

Figure 39 a) DBR photomask and b) Micrograph of processed device

Silicon Nitride was used to define the grating windows where two mask sets (corresponding to case 6 and case 8) were designed for DBR gratings of different lengths. The length of the grating is $6\mu m$ and $12\mu m$ for the front mirror and $14\mu m$ and $30\mu m$ for the back mirror for case 6 and case 8, respectively.

Gratings and connecting dielectric waveguide

A holography process is used to pattern the gratings in the DBR region. The holographic process using BARC layer (bottom anti-reflection layer) and a laser wavelength of 266 nm. The

gratings are dry etched to a depth of about 1000 Å with a methane/hydrogen etch process. At SMU, gratings are fabricated by holographic patterning. At UCSB, gratings are fabricated by E-beam writing. For the holographic method, DUV42P-6 BARC was spun at 2250 RPM for 30 sec for a target thickness of 600 Å and baked on a hotplate at 200°C for 60 seconds. This is followed by spinning a diluted UV6 resist to target 1700 Å thickness, then baked at 130 °C for 60 s. With the holographic gratings table aligned for the correct grating period, the wafers are exposed, then a post exposure bake (PEB) is done on a hotplate at 140 °C, then developed in MF26A developer. The gratings were dry etched with the same CH_4/H_2 process. For Case 6 (one of the many cases considered from the simulations), etch depth was to layer 14 and Case 8 was to layer 13.

Figure 40 shows the photomask pattern of the grating opening and the connecting waveguide. To connect the gratings, laser, and EAM sections, connecting sections are fabricated by depositing e-beam deposited silicon, patterning, and dry etching with the same CF_4/O_2 etch used from previous dielectric mask open steps.

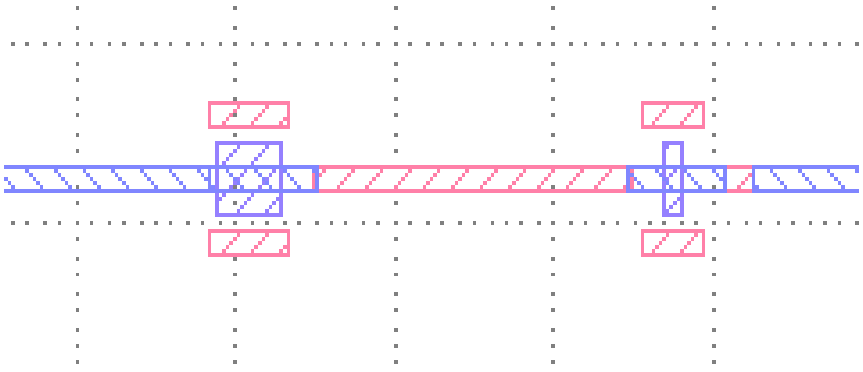

Figure 40 Photomask of grating opening regions and connecting waveguide

The etched gratings were planarized with a Spin on Glass (SOG) material of refractive index of 1.36-1.39. Then silicon is sputtered on top of the gratings. Accuglass 312B spin on glass (SOG)

was used to target a cured thickness of about 2000 Å and an index of refraction of about 1.35 for the lasing wavelength. The SOG was etched back by using a CF_4/O_2 dry etch process. The annealed SOG was measured to have an index of 1.36 using an ellipsometer that used a 632 nm He laser. Since no endpoint system was available, this was an iterative etch using SOG coatings on silicon coupons as the etch monitor. The goal is to have the grooves between the grating teeth filled but not above the grating tooth (planarized). The SEM micrograph in Figure 41b shows that this was accomplished.

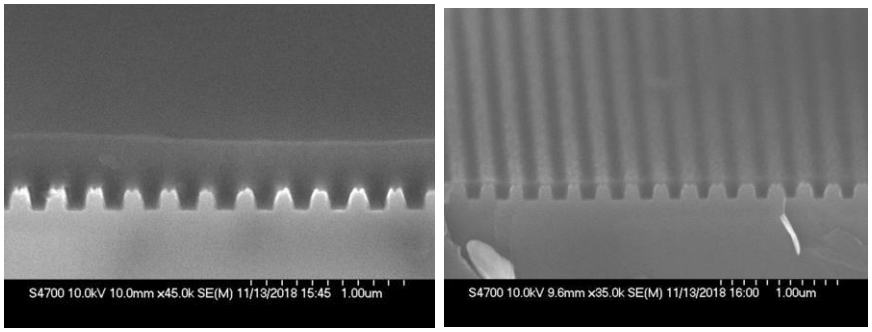

(a) (b)

Figure 41 SEM images a) gratings with SOG before etch back b) after etch back

Then a high index amorphous silicon was sputtered to form the cover layer. For case 6, the target was 5000Å, for case 8, the target was 3500Å. Then the DBR Si Etch mask was used to pattern resist to cover only the grating regions, and the remaining dielectrics etched with a semi-isotropic (500 mT) CF_4/O_2 RIE etch process to ensure dielectrics are also removed from the ridge sidewalls. Increasing the etch pressure to ½ Torr ensures the ion directionality is reduced and the isotropic chemical etch component is increased, thus increasing the lateral etching of the sidewalls. The mask layout and the corresponding optical micrograph of the fabrication area is shown in Figure 42.

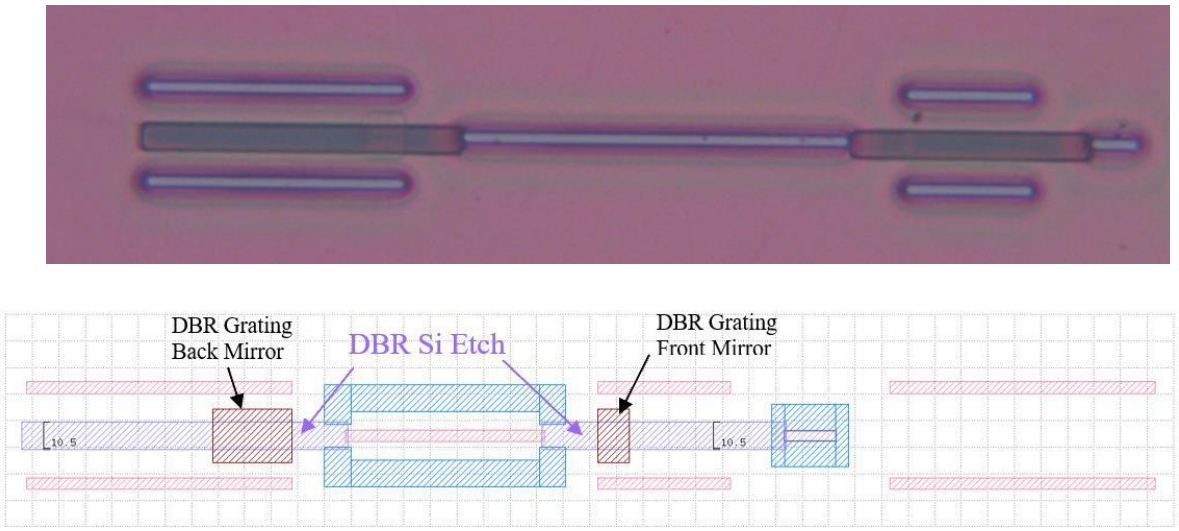

Figure 42 Micrograph of post DBR Si Etch

The next step for the full device would be to pattern the out-coupler windows and pattern the 2nd order gratings for the out-coupler. It was decided, due to budget and complexity for this phase, that we would not pattern the out-couplers and instead used cleaved facets.

The next step was to fabricate the confinement ridge to create a common waveguide for all the components. The confinement ridge is designed to be one micron wider than the EAM ridge to allow for misalignment as shown in Figure 43. For lithography, photoresist Shipley 1813 was spun at 4500 RPM for 30 seconds with a target thickness of 14-16 kÅ. Then a soft bake was performed at 100°C for 60 seconds followed by exposure through the 6th mask layer, Confinement Ridge mask using MJB3 mask aligner at 194 Watts for 5.5 seconds.

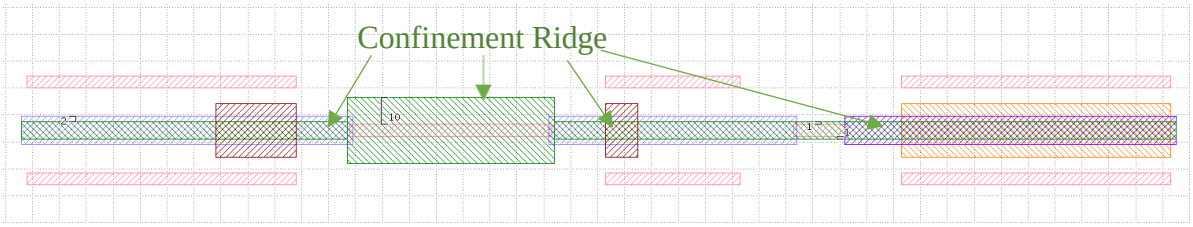

Figure 43 Mask layer 7, Confinement Ridge

Then the photoresist was developed in MF-26A developer for 45 seconds followed by a hard bake hot plate at 100°C for 5 minutes. The confinement ridge was then dry etched in the RIE system. Figure 44 shows the optical microscope image of the confinement ridge after etching after the photoresist was removed.

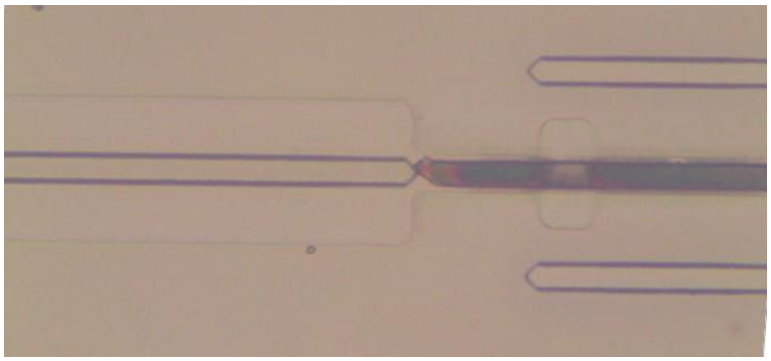

Figure 44 Optical image of the laser area with confinement ridge defined and etched.

N-Well – The N-contact areas are etched down into the substrate

After defining the confinement ridge, the next step is the photolithography for layer 8, N Well. The purpose of N-well pads is to connect the top metal layer to the n-substrate. Therefore, large area recesses are etched down to the substrate, followed by a silicon nitride deposition, then vias are formed using the N-Via layer. N-well pads were designed big enough to allow for probing with small resistance and capacitance. Another criterion to consider when designing the N-well layer is

the need for a good distance between the pads and the sides of the die so that dicing the dies is straightforward, the width of the streets therefore was designed to be 50μm.

Photolithography for this layer followed the same recipe used throughout this project, S1813 was spun at 4000 RPM for 30 seconds. Then wafers were patterned using MJB3 Karl Suss and developed in MF-26A developer for 45 seconds. A hard bake is necessary at this step to harden the photoresist pattern to withstand the wet etch process. After that, the wafer was etched in an InP etchant to etch the InP layer, followed by an InGaAsP etch to layer 2, followed by InP etch all the way down to the substrate.

BCB Processing and P and N Contact

The P-Via and N-Via masks are patterned using a photoactive benzocyclobutene (BCB)-based polymer rather than standard photoresist for reasons of devices speed (discussed earlier).

3.5 Design for high modulation speed

Figure 41 shows a snapshot from an Excel-based device speed calculator developed by Photon Sciences to explore device architecture design choices to influence how fast the transceiver can be modulated. To achieve 100 Gbps, a 3-dB bandwidth of at least 50 GHz is required for the proposed device. If we could fabricate the probe pad and EAM region, shown circled in Figure 38, with an airbridge, where air has a dielectric constant of 1, the device modulation speed would be higher than if we used non-air materials underneath the probing pad area. Airbridges are difficult to implement because of the need to probe on the EAM pad. By using low dielectric BCB material, we can achieve high modulation speed with a manufacturable process and ensuring device testing is straightforward. As shown in the circled region of Figure 45, if we optimize the design choice for speed by choosing a modulator length of 15 microns,

ridges of 3.5 microns wide, and lasers of 150 microns length and use BCB (k = 2.5), then we can obtain speeds to 97 Ghz.

Width pad	Length pad	Pad area cm^2	Runner Length	Runner Width	Runner area cm^2	thk um	Thk cm	Dielectric	Cap	R	RC	Omega	Fc
30	40	1.20E-05	20	20	4.00E-06	3	3.00E-04	1	4.72E-15	50	2.36E-13	4.24E+12	6.74E+11
30	40	1.20E-05	20	20	4.00E-06	3	3.00E-04	1	4.72E-15	50	2.36E-13	4.24E+12	6.74E+11
30	40	1.20E-05	20	20	4.00E-06	3	3.00E-04	1	4.72E-15	50	2.36E-13	4.24E+12	6.74E+11
30	40	1.20E-05	20	20	4.00E-06	3	3.00E-04	1	4.72E-15	50	2.36E-13	4.24E+12	6.74E+11
30	40	1.20E-05	20	20	4.00E-06	3	3.00E-04	1	4.72E-15	50	2.36E-13	4.24E+12	6.74E+11
30	40	1.20E-05	20	20	4.00E-06	3	3.00E-04	1	4.72E-15	50	2.36E-13	4.24E+12	6.74E+11
30	40	1.20E-05	20	20	4.00E-06	3	3.00E-04	1	4.72E-15	50	2.36E-13	4.24E+12	6.74E+11

Length	Width	QW thk	Barrier thl	Number wells	barrier total	Well total	Total Thk	Dielec	Area cm^2	Thk cm	Cap w/o Fringe	1/2*pi*RC
15	4.5	0.01	0.01	11	0.12	0.11	0.23	13.9	0.000001	0.000023	3.61E-14	8.82E+10
20	4.5	0.01	0.01	11	0.12	0.11	0.23	13.9	0.000001	0.000023	4.81E-14	6.61E+10
15	3.5	0.01	0.01	11	0.12	0.11	0.23	13.9	0.000001	0.000023	2.81E-14	1.13E+11
20	4.5	0.01	0.01	11	0.12	0.11	0.23	13.9	0.000001	0.000023	4.81E-14	6.61E+10
20	3.5	0.01	0.01	11	0.12	0.11	0.23	13.9	0.000001	0.000023	3.74E-14	8.50E+10
0	0	0.01	0.01	11	0.12	0.11	0.23	13.9	0.000000	0.000023	0.00E+00	#DIV/0!
50 um dbr	0	0.01	0.01	11	0.12	0.11	0.23	13.9	#VALUE!	0.000023	#VALUE!	#VALUE!
50 um dbr	0	0.01	0.01	11	0.12	0.11	0.23	13.9	#VALUE!	0.000023	#VALUE!	#VALUE!
100um ba	0	0.01	0.01	11	0.12	0.11	0.23	13.9	#VALUE!	0.000023	#VALUE!	#VALUE!
dummy sp	0	0.01	0.01	11	0.12	0.11	0.23	13.9	#VALUE!	0.000023	#VALUE!	#VALUE!

layout number	R	C dev	Cpad-run	RC	1/2piRC	Device Length	Device Width	skip	Laser Length
4	50	3.61E-14	4.72E-15	2.04E-12	7.80E+10	15	4.5		150
3	50	4.81E-14	4.72E-15	2.64E-12	6.02E+10	20	4.5		75
5	50	2.81E-14	4.72E-15	1.64E-12	9.70E+10	15	3.5		150
1	50	4.81E-14	4.72E-15	2.64E-12	6.02E+10	20	4.5		150
2	50	3.74E-14	4.72E-15	2.11E-12	7.55E+10	20	3.5		150

Figure 45 Excel-based device modulation speed calculator

For ease of processing, we decided to spin BCB only once and expose each mask separately, both P-Via and N-Via, then developing. For reasons of capacitance and practical processing, we targeted a cured BCB thickness of about 3 μm. The BCB resist was first spun at a low RPM speed, then step two ramped to 3500 RPM, followed by a soft bake. The average resist thickness was measured at 3.1 μm.

The P-Via alignment was very difficult, having to align a 2.5 um wide contact opening on a 4 μm ridge is very difficult with a contact aligner. This was one motivating factor in processing future lots at UCSB using a UV stepper lithography system that offered ~ 0.25 μm overlay capabilities. The optical micrograph in Figure 46b reveals the very good alignment of the p-contact

open (white area) on top of the ridge. Figure 46a reveals misalignment caused by using a contact aligner.

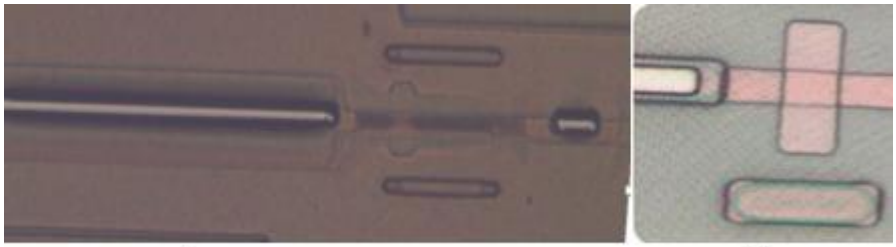

Figure 46 Left-Optical micrograph the p contact opening showing the developed out BCB material with the photolithography done with a contact mask aligner. Right – the processing done at UCSB with a I-line stepper, where the white area is the resist opening on top of the 4um ridge

At SMU, we did not have a low oxygen oven available for the curing of the BCB. A glass flask was rigged with oxygen purging and installed on a conventional hotplate for a 3-step cure process, starting at 150 °C for 15 minutes, and a ramp step from 150°C to 250°C that took 15 minutes, then 250°C for 60 minutes. It was estimated that the oxygen level was about 100 ppm. This was followed by a CF_4/O_2 plasma descum in a parallel plate Technics etcher.

The next steps are the N-Via BCB Etch, N-Via N-metal Lift-off, and the metallization and anneal**.** Figure 47 shows the mask layout for the N and P-metal pattern

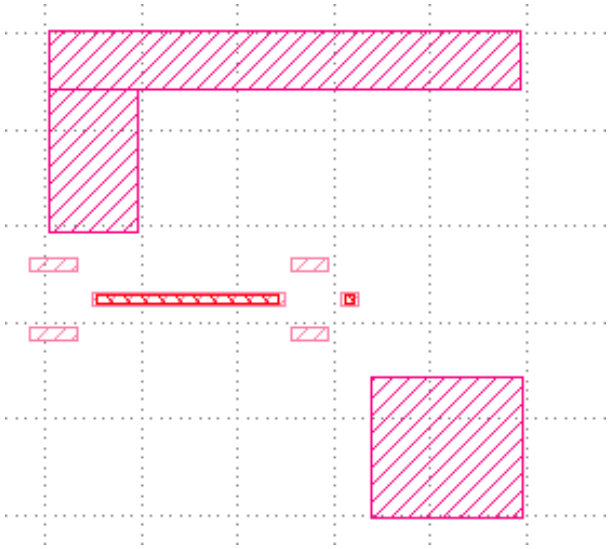

Figure 47 Mask Layout of the N and P metal pattern

3.6 Metal Deposition, Lift-off, Anneal, and Wafer Thinning and Cleaving

P and N metal were deposited by an e-beam tool equipped with a diffusion pump. Lift-off proved to be difficult due to having sloped resist sidewalls. We did not attempt to use a bi-layer lift-off scheme, nor try to make the resist retrograde in profile, resulting in achieving only a partial lift-off as shown in Figure 48. Typically for one-layer lift-off processes, negative imaging photoresist is used in order to achieve a retrograde profile conducive to lift-off (image reversal resist can also be used).

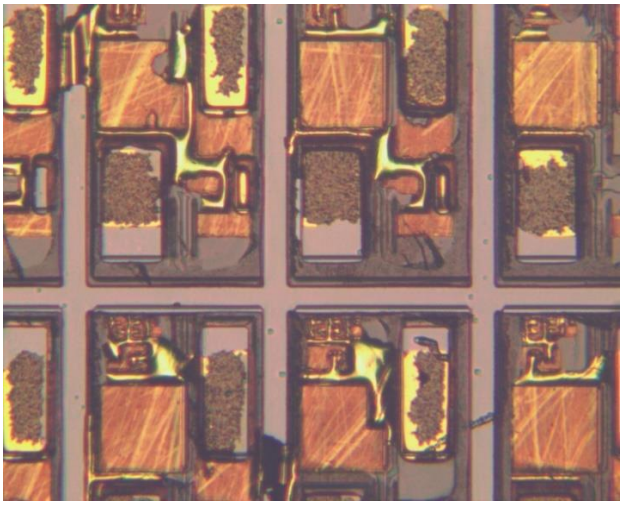

Figure 48 Partial lift-off using a one-layer positive resist process

The N-metal stack was target for Ni 50Å, Ge 50Å, Au 675Å, Ge 275Å, Ni 230Å, Au 2000Å, measured with an acoustic *insitu* crystal monitor during deposition. Such a complicated metal stack is not necessary for these research devices, but this metal stack was used because it was developed at SMU for other similar projects, where device reliability was considered.

For subsequent work, a bilayer lift-off resist (LOR) was used, where upon UV light exposure and developing, the bottom resist layer is undercut, allowing the acetone to contact the resist and lift of the metal. Figure 49 shows the improved lift off with relatively clean metal definition.

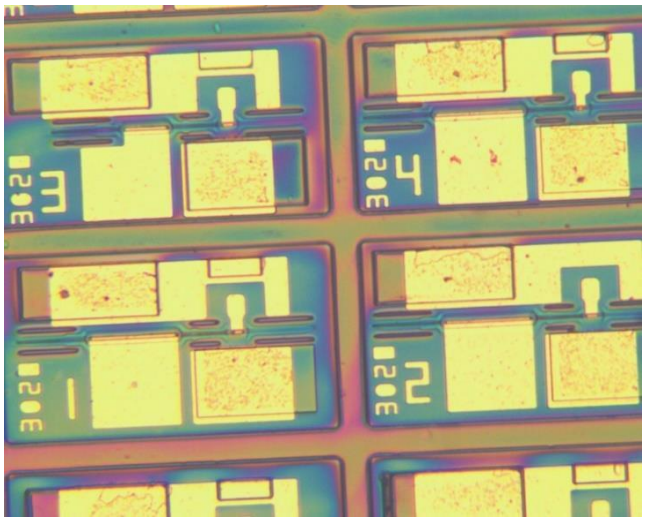

Figure 49 Optical micrograph of the successful lift-off using LOR bilayer resist

Lapping/polishing, N-Metal and cleaving

To produce high quality facet cleaves, the wafer needs to be lapped/polished to about 100-150 μm. A common method is to attach the wafer to a puck and use some type of wax to hold the wafer to the puck, then after thinning the wafer, a solvent is used to remove the wax, or one can put the wafer/puck on a hotplate and gently slide the wafer of the puck when the wax melts. One can improve the wafer removal process by using pucks with small holes bored through them so that the solvent can easily reach the wax, or use an adhesive that can be released by light exposure in addition to heat. For this work, ultra-sol L9 slurry mixed with water was used to thin the wafer to 150 μm as measured by a drop gauge.

As described above, the fully processed device is intended to have the P-metal and the N-metal, as well as 2nd order outcoupling gratings and 1st order reflectors on the EPI side of the wafer. To test these partially processed wafer sections (short-loop), we needed to thin, deposit N-metal on the back side, anneal, and cleave, and measure the light out of the cleaved facets. For ease of handling and testing, bars of ~ 612μm and 1cm long were selected.

CHAPTER 4

4.1 Broad Area results for SMU processed devices

Broad area lasers were fabricated at SMU from the 11QW material and cleaved into lengths of 250, 500, and 750 µm. Table 4 shows the BA parameters with the different lengths measured at room temperature with a pulsed current of 2 µs width and 0.2% duty cycle, giving maximum power, current threshold, slope efficiency, and series resistance. Simulations shown in Figure 50a predicted ridge laser wavelength of 1282 nm at 25°C at the gain peak, and in Figure 50b, 1336 nm at 125 °C, where the integrated device is designed to tolerate this ~ 0.5 nm/°C wavelength increase without the need for temperature control. The actual measured pulsed BA gain peak at 25°C was 1293 nm. It was noted that the p-metal adhesion on the BA lasers was not uniform, some areas showing lifted metal. For this reason, we were not able to measure laser lengths greater than 750 µm long. The adhesion issue may have resulted from excess que time between the pre-metal wafer clean and when the metal was deposited, or possibly oil back-streaming from the diffusion pump on the e-beam metal evaporator (these are known issues from previous process work at SMU). The surface state of the wafer is critical when the first metal layer is deposited in terms of adhesion.

After the epitaxial structure is grown on the 3-inch wafers, it is necessary to take a few quarter sections of one of the wafers and fabricate Broad-Area (BA) lasers. BA test results provide information on the quality of the epitaxial growth and if the target wavelength was achieved. The BA laser stripe was chosen at 100 µm wide and is fabricated by etching the sacrificial InP, the InGaAs/InGaAsP cap layers, and subsequent InP layers down to the etch stop.

The wafer sections are then thinned to about 125-150 µm, n-metal is deposited, and the wafers are annealed. To extract the needed laser parameters, different length of lasers must be used. We chose to cleave at lengths of 250, 500, and 750 µm.

Table 4 Broad Area test results at various cavity lengths

Pmax	Ith_mA	Slope_Eff	Rs	Length
101.1874	485.6709	0.19483	1.213322	250um
129.1738	478.3778	0.178617	1.227747	250um
121.9709	480.8422	0.17056	1.091302	250um
66.46886	747.531	0.148551	0.798603	500um
63.52365	963.7765	0.14854	0.739488	500um
64.03609	769.2888	0.150545	0.812001	500um
25.64742	791.7059	0.147425	1.530931	750um
96.2383	1098.447	0.109329	0.762809	750um
81.86856	1273.356	0.098405	0.555888	750um

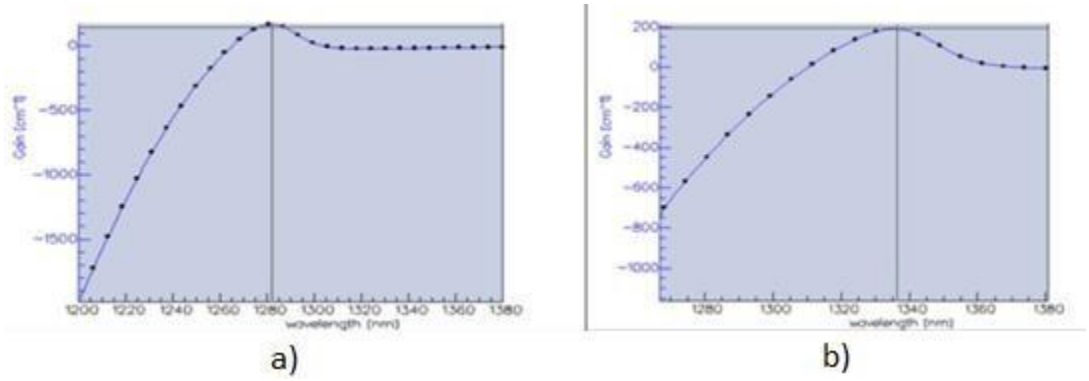

Figure 50 Simulations for Broad Area lasers, a) 25 °C, b) 125 °C

The next round of design and epi growth targeted ~ 1580 nm. Figure 51a gives a maximum optical power of 184 mW at 2.2 A and a threshold current Ith of 523 mA for a 500 µm length laser. Figure 51b shows a 750 µm long laser and the 47c is for a 1000 µm length. Spectral measurements for the 500 um BA lasers give a room temperature potential lasing wavelength from 1568 to 1573 nm.

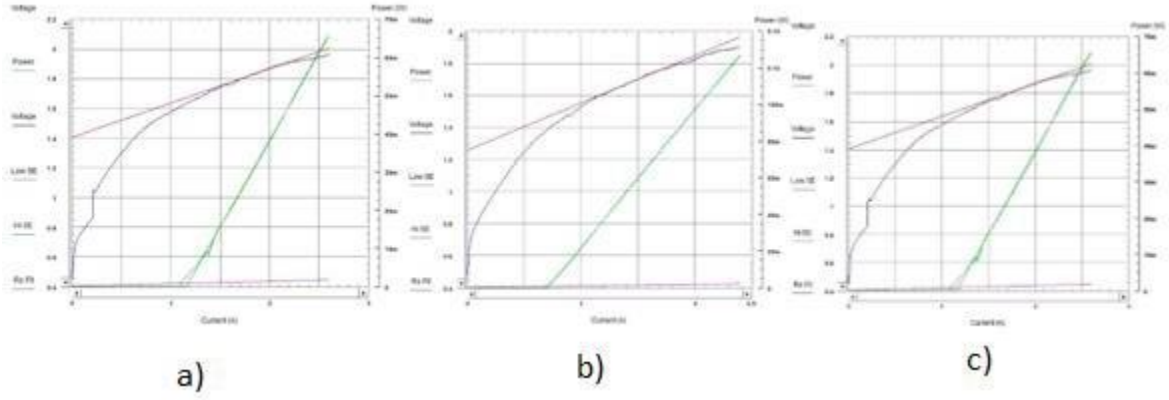

Figure 51 a) ~ 1580 nm wavelength BA LIV curve of 1000 µm length, and b) 750 µm long (middle)and c) 500 µm length (right)

4.2 Device Experimental Results

Through the first two rounds of attempts to fabricate the full devices, we were unable to simultaneously produce useful gratings in both gratings sections and therefore had to cleave the devices to make some useful measurements. The main goal of the testing of the processed devices was for proof of concept, to secure Phase II funding to enable the fabrication of the full device (funding was secured in 2022, largely due to this work).

A long laser section was created by cleaving the wafer, and the rear facet was used as a broad band mirror. We reduced the coupling to the waveguide from the laser to achieve a front broad band mirror so that we could show an actual, but crude functioning of the Laser-EAM operating in the strong absorption region over temperature. As it turned out, the combination of the uncoated back facet and the minimal reflection from the intentional mismatch of the waveguide were not enough to achieve lasing. For the EAM measurements we used the LED emission from the laser section that is integrated with the EAM to show modulation by the EAM, with results shown in Figure 52. We demonstrated both working lasers, and a working EAM independently.

The laser ridge had poor performance, with a threshold current that is about 7X and the slope efficiency of about 1/10 of what is predicted from simulations and BA results. Speculation is that because we had to do a shortcut process, we left silicon sidewalls on the ridge, which would pull the mode out laterally and reduce the effective quantum well confinement factor.

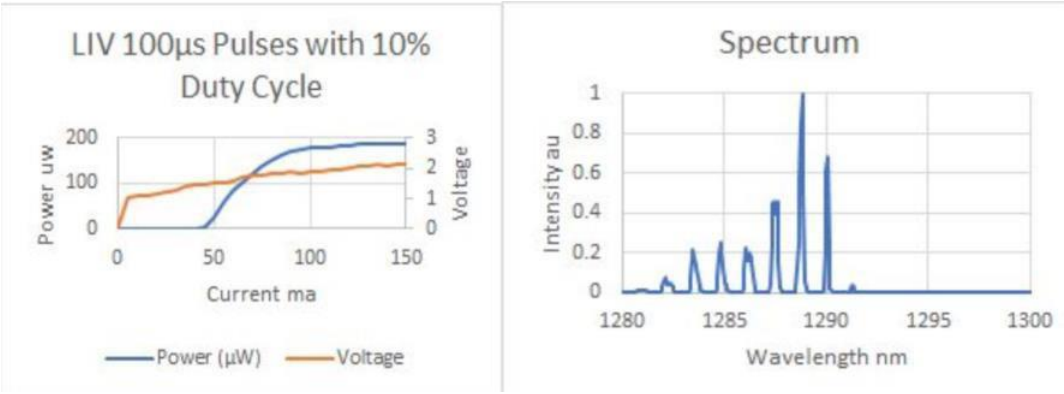

Figure 52 Device measurements in LED mode

The EAM current was measured as a function of reverse bias. The absorption current can be calculated by assuming a spectrum for the LED and convoluting that with the absorption curves. In Figure 53, with the voltage ranging from 0 to about -3V, the absorption current changed substantially, albeit powered by a LED spectrum of very low power.

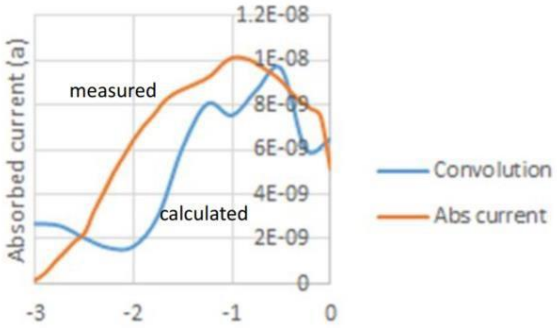

Figure 53 Measured vs. calculated absorption vs. voltage for LED mode device

The EAM and laser sections share the same EPI that is designed towards high absorption response for the EAM. As a key attribute of the device, this ensures that the EAM absorption peak tracks the lasing wavelength through a wide operating temperature range. Figure 54 shows the calculated absorption for the EAM and the extremes of the intended operating range.

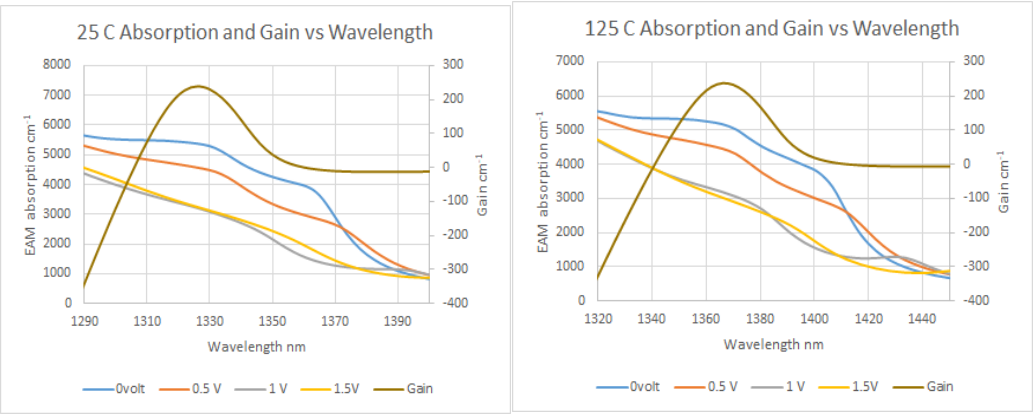

a) b)

Figure 54 Absorption and gain at (a) 25°C and (b) 125°C vs. applied voltage

The voltage influences the absorption due the Stark shift, whereby the absorption edge shifts to longer wavelengths, and the hole and electron wavefunctions overlap to a lesser extent. The QW design approach especially took advantage of the latter absorption mechanism to achieve the desired specification for the temperature and wavelength operating range for available industry applied voltage ranges. Figure 55 shows the measured and simulated current response to applied voltage changes.

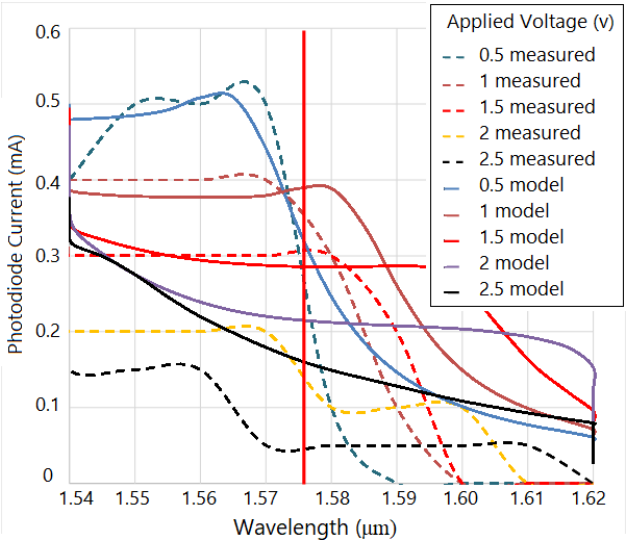

Figure 55 Experimental and simulated photodiode current as a function of wavelength and reverse bias voltage, at ~ 1577 nm wavelength

4.3 1602 nm fabrication progress

As discussed earlier in the thesis, the full-loop fabrication of this transmitter is challenging and phase II funding has allowed working with an III/V foundry company for the processing development. The initial designs are completed, and focus is on a methodical, step-wise process development with look-ahead experiments before processing full-loop lots. The full-loop lots add E-beam, SOG, SOG etch back with look-ahead wafers processed at various steps prior to running the full-loop lots. Look ahead lots showed that many of the process issues have been addressed. Figure 56 shows optical micrographs of a look-ahead lot processed to the P-contact etch and pad metal stage. Very good alignment and metal lift-off, with evidence of all the previous pattern and etching steps being very clean. Following this, shown in Figure 57, the full-loop device lots at the ridge, gratings, and grating etch steps show progressively worse roughness/micro-masking through the etch steps.

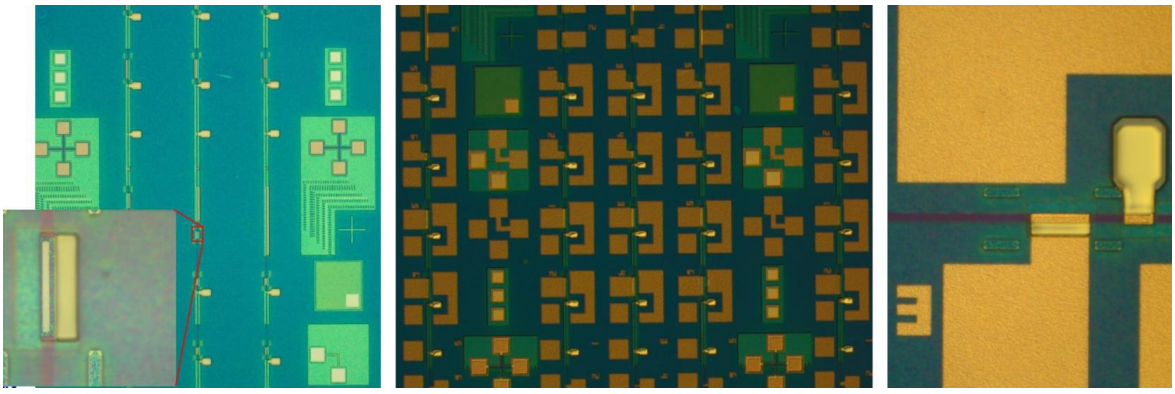

Figure 56 Optical micrographs of look-ahead lot at P-contact and pad metal

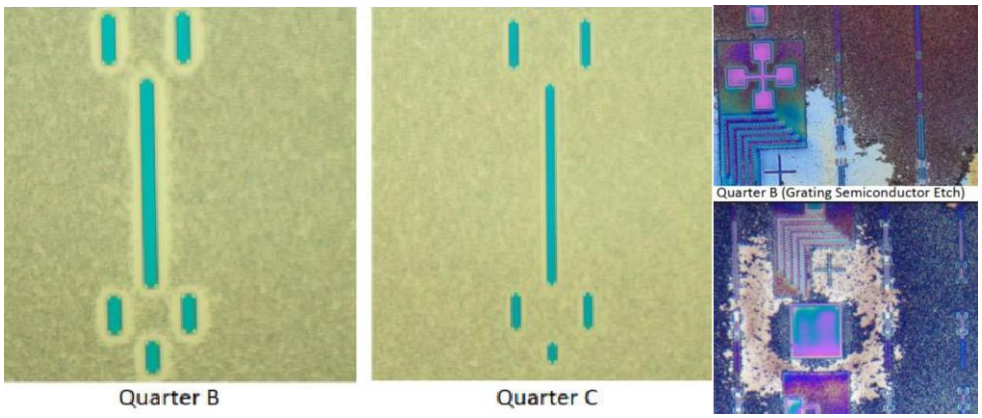

Figure 57 Full-loop lots showing roughness/micromasking during the ridge Through grating etches

Analysis concluded that an alloy-polymer mixture created a micro-masked etch. The second full-loop lot therefore implemented an intermediate cleaning (and to forego the implant step to expedite the lot) and inspection process. Very clean looking optical micrographs quarters A, B, and C are shown in Figure 58.

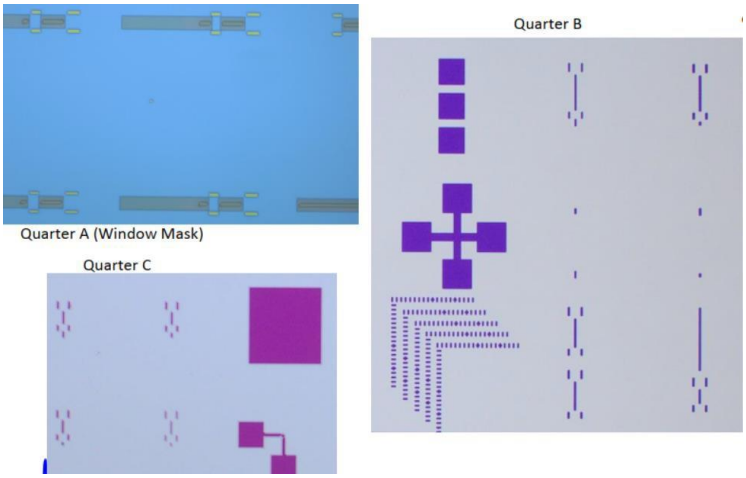

Figure 58 2nd full-loop lots wafers sections though ridge/grating patterning with new clean step

The remaining ¼ wafer section will be processed when satisfactory full-loop results are achieved for sections A, B, and C.

Initial work for this thesis patterned the gratings with holography, but later we decided to develop e-beam patterned gratings. Because of the need to fill the area between the grating teeth with planarized low optical index SOG, a trapezoidal grating etch profile was targeted with a 50% duty cycle. Figure 59 shows a top-down SEM and an optical micrograph image of the e-beam written gratings. Next steps are to optimize the silicon dioxide hard mask and dial in the duty cycle to close to 50%.

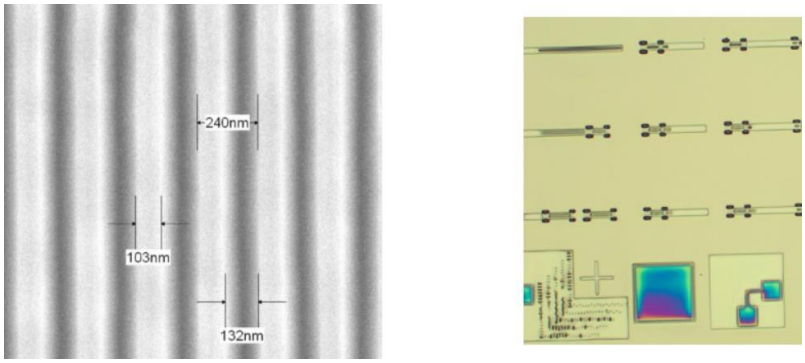

Figure 59 Top-down SEM and optical micrograph of the e-beam patterned resist

An additional photomask was added to the process flow to help in clearing-out the SOG during the etch steps, shown in Figure 60. An *insitu* laser endpoint detector will be used to ensure the correct level of over-etch to completely remove the SOG from the field.

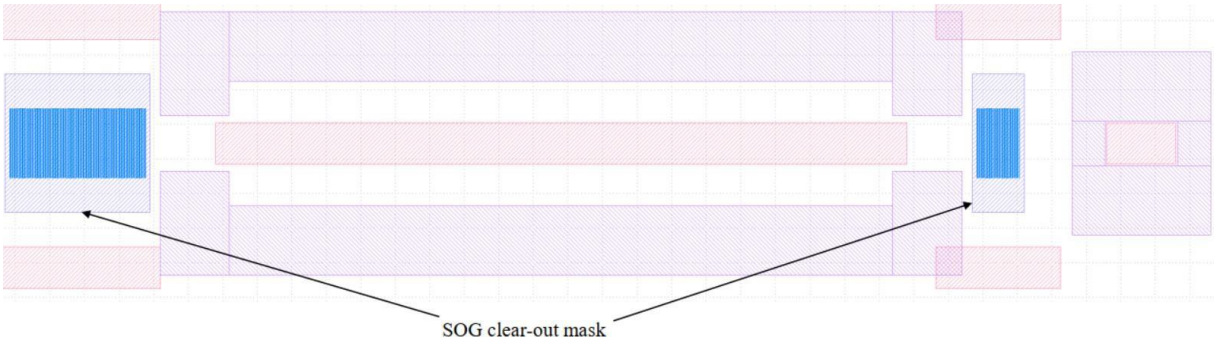

Figure 60 SOG clear-out photomask pattern

Once the SOG is planarized, the Si cover layer needs to be fabricated on top of the SOG. The e-beam evaporated silicon cover layer is patterned by lift-off, with a well-defined silicon pattern shown in the optical and SEM micrographs in Figure 61.

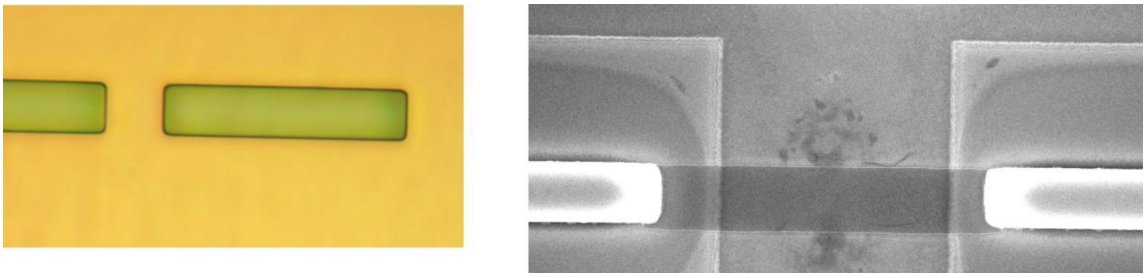

Figure 61 Post-lift off optical and SEM image of the silicon cover layer

4.4 1602 nm 11 QW design considerations

Lessons learned from the previous work in the thesis were incorporated into the latest epitaxial design and MBE growth run. Design changes focused on improving the EAM

performance and ensuring the fabrication is less challenging by incorporating two etch stop layers and layer changes specifically for grating fabrication. The full epitaxial stack in provided in Appendix B. It was decided to start with the optimized absorption and gain design and make changes in the QW region to improve carrier transport, with the goal of improving the EAM current handling capability. Simulations were run where the tunneling of heavy holes to adjacent wells and out of the active region was studied to improve the potential EAM performance. With layer changes to thinner barriers, lower barriers, and lower strain in the wells, Figure 62 shows the wavefunction verses position in the QWs with 0 V applied (worse case. Electrons and light holes tunnel much more easily than heavy holes.

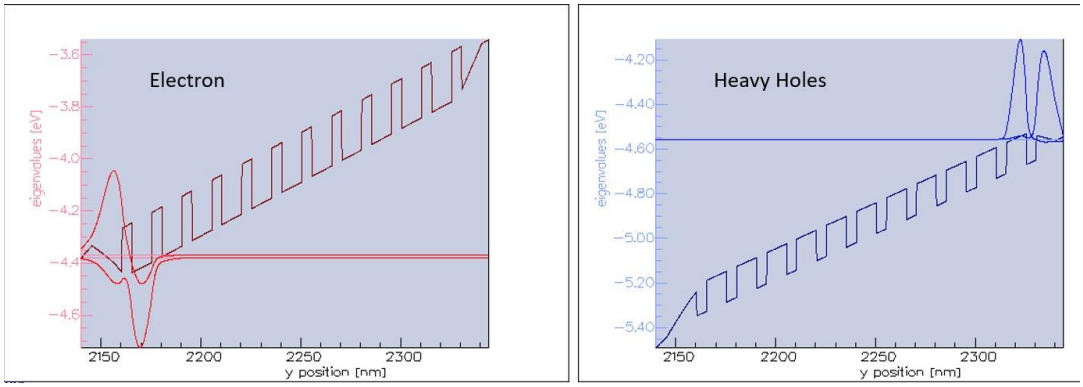

Figure 62 Tunneling out of the active region for both electrons and heavy holes at 0 bias (worst case)

Figure 63 shows the conduction band edge verses position and quasi-fermi levels, exhibiting a slow slope in the electron fermi level on the n-side (purple trace), a substantial slope in the hole quasi-fermi level (red trace), and a low sloped region where there is no mode, allowing for heavier doping in this region (green trace).

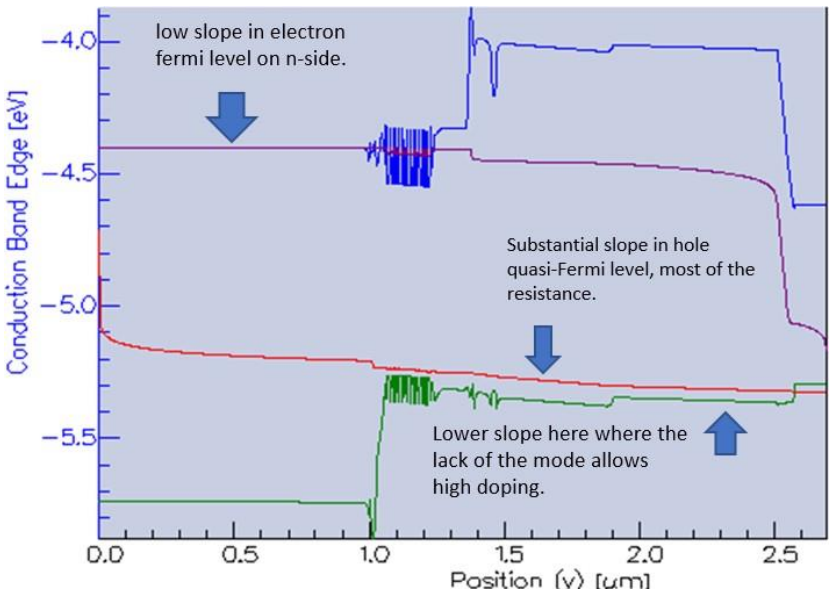

Figure 63 Conduction band edge verses position and quasi-fermi levels

For the new epitaxial design, Figure 64 shows cross-section illustrations at various process steps, showing (not to scale) the relative height in the epitaxy stack of the various device sections.

N-Well

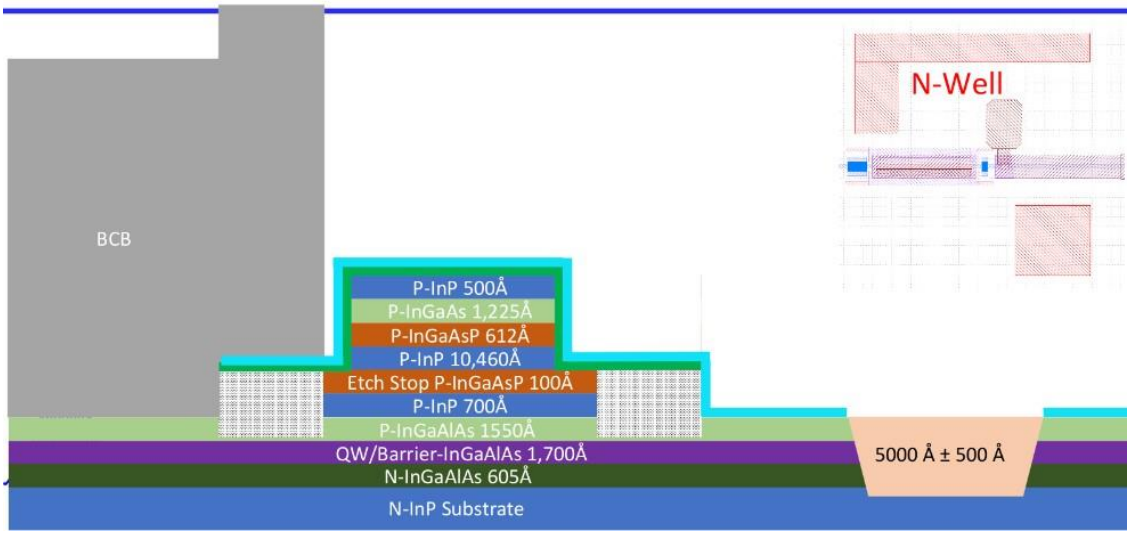

N-Metal

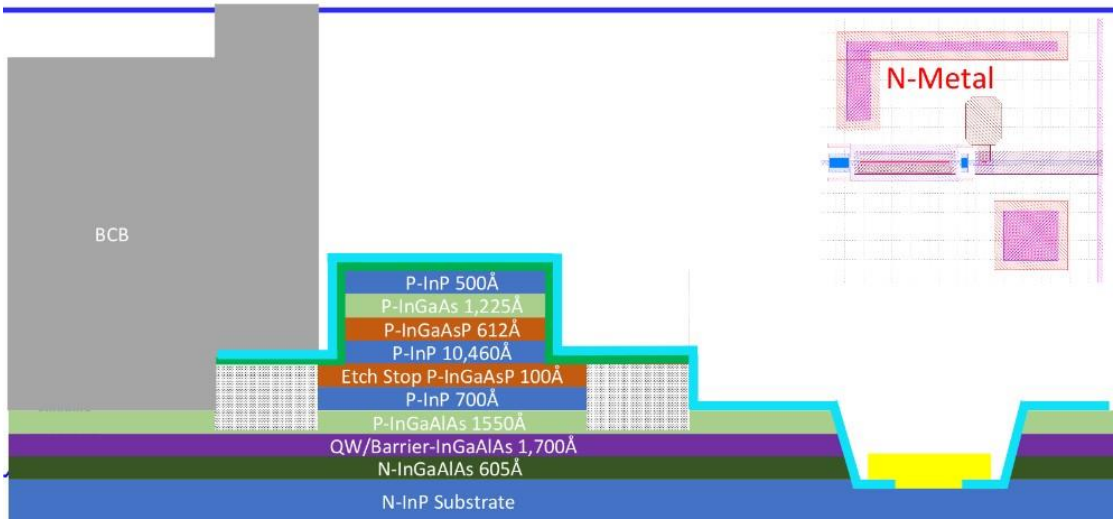

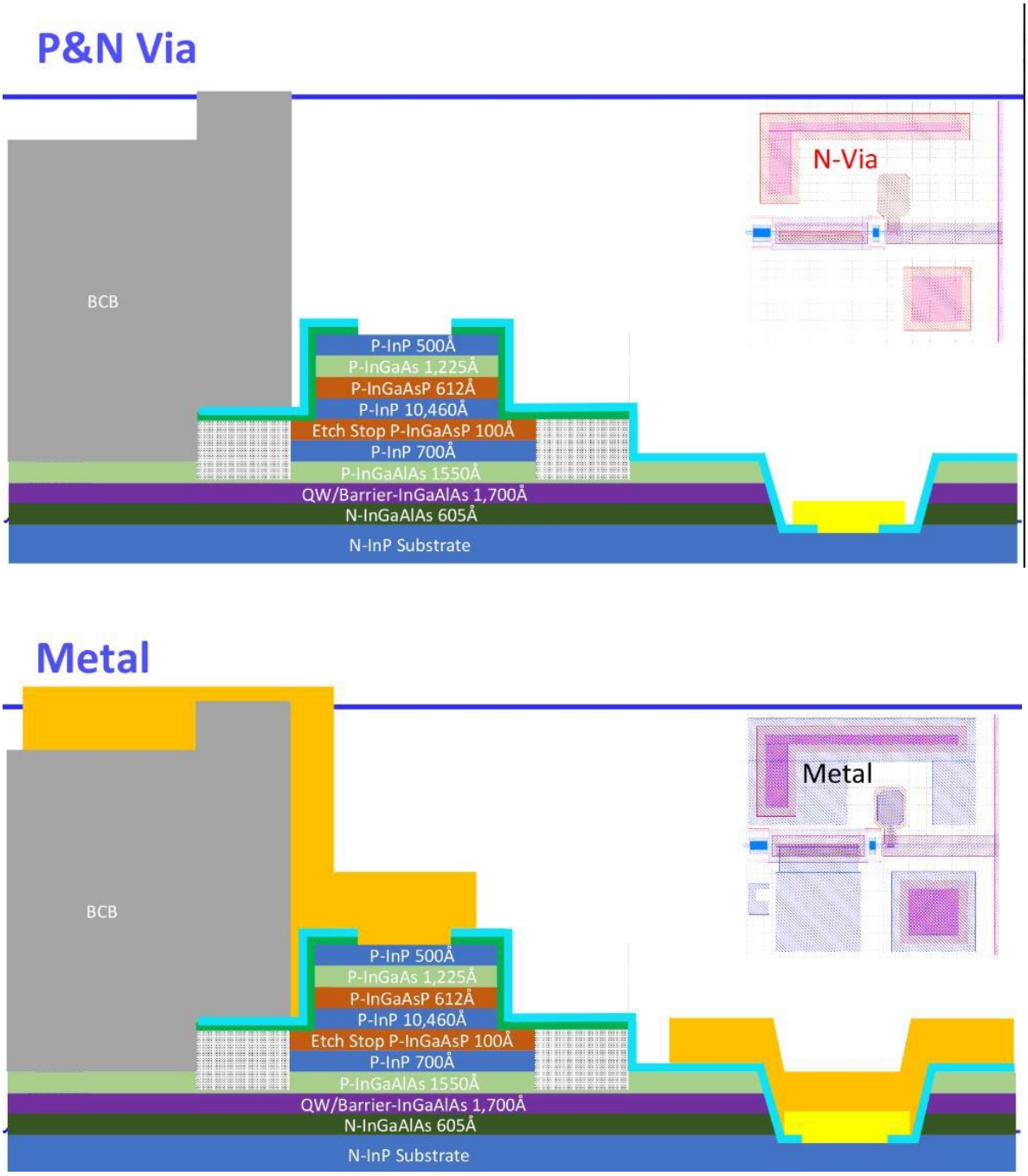

Figure 64 – Cross-section diagrams at various processing stages for the new epitaxial design

CHAPTER 5

5.1 Conclusions and Future Work

The design of a lower power terabit transmitter has been completed. This design included ECS gratings and a monolithic 11 QW laser and EAM. The mask and process flow were completed, with several campaigns to fabricate short-loops devices. These short-loop devices enabled learning of the fabrication process and to show basic electro-optical functionality of the design.

It was anticipated that the fabrication of the proposed device would be quite challenging, and this has proven to be the case. Work has begun to realize the full-loop devices by working with an III/V foundry service company. The new EPI design is provided in appendix B along with the modified traveler in Appendix C. High speed testing is not trivial. Plans are to perform the AC testing to 40 GHz at Photon Sciences, Inc. For higher speed testing, discussions are underway with Georgia Tech

One possible application of the proposed device would require coupling the 2nd order out-coupler power efficiently to a single mode fiber. This would require exploring variations in the duty cycle and grating depth, and other design choices, to approach a gaussian-like beam profile to couple into a 9-micron core of the fiber.

Future work should consider quantum well intermixing mainly to reduce absorption in the passive waveguides, which gives the ability to control the QW bandgap post epitaxial growth. By inducing impurities and vacancies, changes to the refractive index of the QW structures reducing design constraints for monolithic integration, such as the integration of the waveguides,

laser, gratings, and EAM in this thesis work [59]. Impurity-free vacancy disordering (IFVD) has been used to spatially control the absorption band edge of QW structures across a wafer [60], and in this paper, lasers with bandgaps tuned to five different positions have been fabricated on a single chip.

REFERENCES

[1] T. Higashi et al., “Observation of reduced nonradiative current in 1.3-μm AlGaInAs-InP strained MQW lasers,” IEEE Photon. Technol. Lett., vol. 11, pp. 409–411, Apr. 1999.

[2] M. Yamada et al., “High temperature characteristics of 1.3-μm InAsP/InAlGaAs ridge waveguide lasers,” IEEE Photon. Technol. Lett., vol. 11, pp. 164–166, Feb. 1999

[3] S. R. Selmic, T. Chou, J. Sih, J. B. Kirk, A. Mantie, J. K. Butler, D. Bour, and G. A. Evans, “Design and Characterization of 1.3-μm AlGaInAs-InP Multiple-Quantum-Well Lasers,” IEEE J. Quantum Electron., vol. 7, no. 2, pp. 340-349, March/April 2001.

[4] Southern Methodist University Photonics Group website page for WAVEGUIDE software: s2.smu.edu/ee/smuphotonics/WAVEGUIDE/Main_Waveguide.html

[5] Southern Methodist University Photonics Group website page for the PDF of the thesis of Robert B. Smith, University of Washington, 1977, https://s2.smu.edu/ee/smuphotonics/Antenna%20Laboratory/ModeigThesis.pdf

[6] P. W. McIlroy, A. Kurobe, and Y. Uematsu, “Analysis and application of theoretical gain curves to the design of multi-quantum-well lasers,” IEEE. J. Quantum Electron., vol. 21, pp. 1958–1963, 1985

[7] “A Comparison of Four Approaches to Photonic Integration”, J. Bowers, A. Liu, 2017 Optical Fiber Communications Conference and Exhibition (OFC), Date of Conference: 19-23 March 2017

[8] Infinera Corporation, www. Infinera.com

[9] R.H. Dennard, “Past Progress and Future Challenges in LSI Technology”, IEEE Solid-State Circuits Mag. 7[2], 29(2015)

[10] J. Bowers, T. Komlienovic, M. Davenport, “Recent Advances in Silicon Photonics Integrated Circuits, Invited paper, Proc. Of SPIE Vol. 9774 977402-1, 2016

[11] Intel silicon photonics corporate web site: www.intel.com/content/www/us/en/products/details/network-io/silicon-photonics.html

[12] R. H. Johnson and G. A. Evans, "Temperature Insensitive Integrated Electro-Absorption Modulator and Laser". United States Patent 9762025, 12 September 2016.

[13] G. A. Evans, J. K. Butler, J. B. Kirk, R.-H. He, J. Yao, G. Li, X. Zheng, and A. V. Krishnamoorthy, "Enhanced Coupling Strength of Gratings". United States Patent 38453, 5 September 2013

[14] “100 Gbps Radiation Tolerant Optical Transceiver,” DOE FY 2018 Phase 1 STTR Release 2 Topic 27. HIGH-SPEED ELECTRONIC INSTRUMENTATION FOR DATA ACQUISITION AND PROCESSING, Subtopic: d. Radiation-Hard High-Bandwidth Data Transmission for Detectors at High Energy Colliders

[15] “Low power 7.2 Terabit Transmitter for Exascale Computing”, NASA SBIR 2019-I : S5.01-3085: Technologies for Large-Scale Numerical Simulation (SBIR), Exascale Computing. Photonic Sciences, Inc

[16] K. D. Choquette, A. Melgar, W. North, S. E. Ralph, N. Jahan, J. A. Tatum, “Supermode Dynamics for VCSEL Modulation,” IEEE Photonics Conference (2021).

[17] Cheng, H.-T.; Yang, Y.-C.; Liu, T.-H.; Wu, C.-H. Recent Advances in 850 nm VCSELs for High-Speed Interconnects. Photonics 2022, 9, 107. https://doi.org/10.3390/photonics9020107

[18] J. Manning, R. Olshansky, “The Carrier-Induced Index Change in AlGaAs and 1.3 um InGaAsP Diode Lasers, IEEE Journal of Quantum Electronics, VOL. QE-19, NO. 10, October 1983

[19] Fadaly, E.M.T., Dijkstra, A., Suckert, J.R, “Direct-bandgap emission from hexagonal Ge and SiGe alloys”, Nature 580, 205–209 (2020)

[20] Ben G. Streetman, Sanjay K. Banerjee, Solid State Electronic Devices, Third Edition, Pearson, 2015

[21] E.F Schubert Light-Emitting Diodes, Cambridge University Press, 1988

[22] G. A. Evans and J. M. Hammer, Surface Emitting Semiconductor Lasers and Arrays. New York, NY, USA: Academic, 1993.

[23] T. Numai, Fundamentals of Semiconductor Lasers, Springer, 2015

[24] P.C. Safa Kasap, Springer Handbook of Electronics and Photonics, Springer, 2006

[25] D.S. Chemla, “Quantum Wells for Photonics” Physics Today, vol. 38, no 5, pp. 56-64, 1985

[26] J. Clerk-Maxwell, "A Treatise on Electricity and Magnetism," Nature, pp. 478-480, 1873

[27] J. Huang, K. Liu, J. K. Butler, N.-H. Sun, and G. A. Evans, ``First order grating coupling coefficients in asymmetric three-layer waveguides for transverse electric modes," J. Lightwave Technol., vol. 35, no. 11,1509 pp. 2200 2210, Jun. 1, 2017.

[28] M. Born, E. Wolf, “Principles of optics: electromagnetic theory of propagation, interference and diffraction of light 4th ed”. New York: Pergamon Press, 1970. pp. 66-70.

[29] Winick, Kim A. "Effective-index method and coupled-mode theory for almost-periodic waveguide gratings: a comparison." Applied optics 31.6 (1992): 757-764.

[30] G. A. Evans, J. K. Butler and R.-H. H. Jay Kirk, "Enhanced Coupling Strength Gratings". US Patent 10371898, 6 August 2019.

[31] G. A. Evans, J. K. Butler, J. B. Kirk, R.-H. He, J. Yao, G. Li, X. Zheng and A. V. Krishnamoorthy, "Enhanced Coupling Strength Grating Having a Cover Layer". US Patent 10620379, 14 April 2020.

[32] M. Dezfuli, W. Zhang, F. C. II, S. McWilliams, R. H. Johnson, N.-H. Sun, J. K. Butler and G. A. Evans, "Analysis of Second-Order Enhanced Coupling Strength Grating Out-Coupler in III-V Photonic Waveguides," in preparation, 2023.

[33] G. Hadjicostas, J. Butler, G. A. Evans, N. W. Carlson, and R. Amantea, “A numerical investigation of wave interactions in dielectric waveguides with periodic surface corrugations,” IEEE J. Quantum Electron., vol. 26, no. 5, pp. 893–902, May 1990.

[34] Mary Dezfuli, “second-order enhanced coupling strength outcouplers for a monolithic laser-absorption modulator”, PhD dissertation, SMU 2022

[35] Freddie Castillo, “First order enhanced coupling strength gratings for laser-electro absorption modulator transmitters”, PhD dissertation SMU 2022

[36] J. K. Butler, N. H. Sun, G. A. Evans, L. Pang, and P. Congdon, “Grating assisted coupling of light between semiconductor and glass waveguides,” J. Lightw. Technol., vol. 16, no. 6, pp. 1038–1048, Jun. 1998.

[37] J. K. Butler, W. E. Ferguson, G. A. Evans, P. Stabile and A. Rosen, "A Boundary Element Technique Applied to the Analysis of Waveguides with Periodic Surface Corrugations," IEEE Journal of Quantum Electronics, vol. 28, no. 7, pp. 1701-1709, July 1992.

[38] H. Kogelnik and C. V. Shank, “Coupled wave theory of distributed feedback laser,” J. Appl. Phys., vol. 43, no. 5, pp. 2327–2335, May 1972.

[39] A. Hardy, D. Welch and W. Streifer, "Analysis of Second-Order Gratings," IEEE Journal of Quantum Electronics, vol. 25, no. 10, 1989.

[40] J. K. Butler, N.-H. Sun and G. A. Evans, "Waveguide Characteristics Near the Second Bragg Condition," IEEE Access, 3 October 2022

[41] S. McWilliams, N. Stelmakh, G. Evans, “High-brightness 1064-nm grating-outcoupled surface-emitting semiconductor lasers”, Proceedings of SPIE , Volume 6287 (1) – Aug 31, 2006

[42] R. Pelzel, “A Comparison of MOVPE and MBE Growth Technologies for III-V Structures, 2013, Materials Science

[43] University of Michigan LNF Wiki https://lnf-wiki.eecs.umich.edu/wiki/Growth

[44] B. Zhao and A. Yariv, "Quantum Well Semiconductor Lasers," in Semiconductor Lasers Academic P, 1999, pp. 1-121.

[45] Sandra R. Zivanovic et al. IEEE J. Quantum Electron., vol. 7, no. 2, pp. 340-349, March, April 2001

[46] S. R. Selmic, T. Chou, J. Sih, J. B. Kirk, A. Mantie, J. K. Butler, D. Bour, and G. A. Evans, “Design and Characterization of 1.3-μm AlGaInAs-InP Multiple-Quantum-Well Lasers,” IEEE J. Quantum Electron., vol. 7, no. 2, pp. 340-349, March/April 200

[47] M. Lee, S. Cho, “Design for high reliability of CMOS IC with tolerance on total ionizing radiation dose effect” IEEE Transactions on Device and Materials Reliability, Vol 20, June 2020

[48] H. Johnston, T. F. Miyahira and B. G. Rax, “Proton Damage in Advanced Laser Diodes,” IEEE Trans. Nucl. Sci., 48(6), pp. 1764-1772 (2001)

[49] K. Gill, G. Cervelli, R. Grabit, F. Jensen, and F. Vasey, Radiation Damage and Annealing in 1310 nm InGaAsP/InP Lasers for the CMS Tracker, 2001

[50] R.K Mohhaev, Research of Quantum Well Laser Diode’s and Heterostructural P-I-N Photodiode’s of Fiber-Optic Modules Radiation Hardness to Gamma-ray and Neutron Irradiation, National Research Nuclear University MEPhI (Moscow Engineering Physics Institute), Kashirskoe shosse 31, Moscow, 115409, Russia 2018

[51] Sandia Report SAND2004-4725 “Effects of Radiation on Laser Diodes”, 2004

[52] JollyA.,Vicrey, J. “Modelling threshold shift of power laser diodes under neutronic and photonic irradiation, “IEEE Trans. Nucl. Sci 1994, 41 (3), 503-509

[53] J. Hopwood, Plasma Sources Sci. Technol. A 1, 109 (1992)

[54] T.J. Sommerer, M.J. Kushner, J. Appl. Phys. 70 (1991) 1240

[55] J. Hopwood, Plasma Sources Sci. Technol. 1 (1992) 109

[56] S.A. Cohen, in: D.M. Manos, D.L. Flamm (Eds.), Plasma Etching: An Introduction, Academic Press, San Diego, CA, 1989

[57] J. Lin, “Smooth and vertical-sidewall InP etching using Cl2/N2 inductively coupled plasma”, Journal of Vacuum Science & Technology B: Microelectronics and Nanometer Structures Processing, Measurement, and Phenomena 22, 510 (2004)

[58] Ion Implantation in III–V Semiconductor International Journal of Modern Physics B, Vol. 07, No. 28, pp. 4687-4761 (1993), S.J. Pearson

[59] J.H. March, “Quantum well intermixing”, Semiconductor Science and Technology, Volume 8, 1136, 1993

[60] B. Ooi, K. McIlvaney, M. Street, “Selective Quantum-Well Intermixing in GaAs-AlGaAs Structures Using Impurity-Free Vacancy Diffusion, IEEE Journal of Quantum Electronics, Vol. 33, No. 10, October 1997

Process Traveler for Tranmitter

Lot ID:							**Epi Source:**		
							Wafer No.		
Customer:		NASA					**Rev.**		
Step #	**Tool**	**Process**	**Procedure/Parameters**	**Qty In**	**Qty Out**	**Operator**	**Date**	**Data/Comments**	
PHOTO PATTERN RIDGE MASK									
		Silicon Nitride	UCSB PECVD Silicon Nitride (could be oxide)			**Index Spec: 1.98 to 2.01**		Target Thickness (Å)	**2000 or whatever is appropriate.**
								Process	
								Time:	
								Actual Thicknes (Å)	
								Actual n Value	
	UCSB/Stepper 2 Autostep	UCSB Photoresist Process	SPR955CM-1.8, 4KRPM for 30", Bake 90 C for 90", exp = 2.3", focus offset = 0, PEB = 110 C for 90", AZ300MIF dev for 60"					**Mask ID: Ridge** **Align 90 degree rotation so ridges have dovetail.**	
	UCSB/Technics	UCSB Technics prestrip							
	ICP2 Panasonic	Dielectric Etch	20 % overetch Nitride					Laser endpoint system is available on this tool.	
	UCSB	optical microscope inspection and measure height with profilometer	Inspect for complete Nitride etch and measure profilometer height.						
	UCSB								
	UCSB/Technics	UCSB Technics Ash	20" 300W Oxygen, 200 mT, Inspect					Step height =	
DRY ETCH RIDGE PATTERN									
	UCSB	Partial Dry Etch Cladding InP	pressure= (1.5 mT), bias/ICP powers=75/900 W, Cl2/N2 flow rate=20/10 sccm (etch rate is about 0.6 µm/min.).						**Etch 80% of depth of layers 28-22,= 80% x 12798 A = 10238 A. Possible laser endpoint system. Measure SiNitride etch rate prior to ridge etch for more accurate depth determination.**
	UCSB/Technics	UCSB Technics Ash	20" 300W Oxygen, 200 mT						
Wet Etch Ridge									
	UCSB	Wet Etch Cladding InP Leftover	1) DI water for 30 sec to ensure the wafer is wetting ok 2) BOE (10:1) dip for 1 sec 3) Etch InP cladding in HCl: DI water: H3PO4 (12:3:5) etchant in Ice bath, or 3:1 Phosphoric/HCL room temp.			**Etch to etch stop 2560 A**		1. etch remaining InP of layer 22 and layer 21, target use 25% OE. Height _____ ,	
	UCSB/Technics	UCSB Technics Ash	20" 300W Oxygen, 200 mT						
	UCSB	Inspect and Measure Final Depth and Width of Ridge						**Depth_____ Width of 4 um Rdge_____**	

Ion Implant								
		1000 A SiNx dep	**Consider Thinner Reduces step at Ebeam**					
	UCSB	UCSB Litho Process	**SPR220-3.0, 2.5 krpm/30", bake 115°C/90", exp 0.72", focus offest 10, PEB 115°C/90", Dev AZ300MIF 60"**			**Target 3 micron resist**		Mask ID: **Implant Mask**
	Implant shop in Southern California	Ion Implant, Kroko Brothers	40 KEV He, 1e14/cm^2, 7 degrees					
		Strip resist	May take iterations of solvent and ashing, NMP					Note: This is very modest implant in terms of resist hardening, Didn't have issues stripping resist last time
Pedestel/Window								
	UCSB/Stepper 2 Autostep	UCSB Photoresist Process	Dehydration bake: 115C Coat HMDS: 4000rpm Bake: 100C Coat SPR955CM-1.8: 3000rpm Bake: 90C					Mask ID: **"Protective" Mask**
	UCSB	Etch 1st Etch Stop InGaAsP	H2SO4 : H2O2 : DI water (1:2:10) etchant at Ice 15 sec, 5C. DI water rinse for 30 sec., N2 dry.					Etch the 100 A thick layer 20, perform height measurement Height _____
	UCSB	Wet etch	1)Etch layers 19-17 InP = 700 Angstroms with HCl: DI water: H3PO4 (12:3:5) etchant in Ice bath, (will stop on etch stop layer 16)					Measure step height change of 700 A with profilometer. Etch until layer 16 (InAlGaAs)
	PECVD 2 Vision 310	SiO2, "STD SiO2"	Deposit SiO2 **400** A to serve as etch mask for ebeam gratings. 800 mT, 30 W RF, 300 sccm SiH4, 1420 sccm N20, Get optimal from Ebeam team.			**Ash prior to SiO2????**		**Dep rate is 287 A/min**
Ebeam Process								
	UCSB	Heard back from UCSB today, they need to know our depth of etch and the material composition of the material to be etched, needs to be hardmask, we can use the CL2/N2 etch process for gratings. Do we get trained on gratings or have UCSB do it for us, need to find out cost difference. (May need to do ash before opening SiO2)						
	UCSB	Gratings Etch	**Open SiO2 first**, then **400** A+ overetch grating dry etch, UCSB recommends we use the MHA grating for this, wasn't available last year during our trip. (Lee Sawyer is contact for MHA) (Remove ZEP resist after opening SiO2)					Get grating dimensions from Freddie. Etch 0.13 um+/- .025 um into semiconductor. We would like tighter than +/- 0.025. Duty Cycle 50% +5-10%
	UCSB	Wet Etch SiO2	6:1 BOE Etch - remove remaining SiO2 form ridge tops, top of grating,s and SiO2 from window layer.			**Etch all SiO2**		**Etch SiO2 Selectivly**
	UCSB	Etch all nitride						

Gratings Index Engineering + Confinement ridge								
	UCSB	Fill grating teeth with SOG	Use Futurrex IC1-100, ~1000 A "cured" for 5000 RPM 40". Scott to provide data sheet Point of Interest: Slower SOG spin for planarization after etching. See next tab			**Prepare Pilot wafers at the same time, and cure them**		Target: fill grating teeth to top of grating, gratings are 1300 A deep. Measure index after bake on test samples, should be around 1.36-1.4 index
	UCSB		Follow Futurrex recommended Cure					Measure annealed film thickness on test sample and index
	UCSB	SOG Etch back	SF6 plasma process for etch back, need to etch back so SOG is planarized on the top of the grating teeth (Futurrex seems to prefer CF4/O2)			**Etch depth from top of teeth to 400 A below top of teeth.**		Index 1.35@1550 for laser endpointer. Check for index for proper wavelength.
	UCSB/Stepper 2 Autostep	UCSB Photoresist Process	Residual SOG removal. (remove from edges of ridge at front and back) Overexpose with classic negative resist to overfill window with resist.					Mask ID: **Window Mask (DBR Nitride 3)**
	UCSB/Technics	UCSB Technics prestrip						
		BOE Etch	Etch remaining SOG, assume about 2000 A of SOG to remove because of possible thick areas near ridges.			**Need suitable(SEM) inspection on at least 1 wafer to make sure it is clear against ridges.**		SOG etch rate is very dependend on BOE concentration, best to measure BOE etch rate
		Strip/Ash	Strip and ash photoresist					
	UCSB	Titania Chemical barrier and SOG over etch fill	Atomic Layer Deposition (Oxford FlexAL) TiO2 400 Å					n = 2.43 @ 1.57 µm
	UCSB	Deposit Armorphous Silicon Cover layer	Deposit Silicon - Use Ebeam 1 system, silicon recipe on WIKI Point of Interest: Use evaporated a-Si instead of sputtering. See next tab					1300Å ±8% Critical, do not put all wafers in the same run. Check monitor vs step height.
	UCSB/Stepper 2 Autostep	UCSB Photoresist Process	SPR955CM-1.8, 4KRPM for 30", Bake 90 C for 90", exp = 2.3", focus offset = 0, PEB = 110 C for 90", AZ300MIF dev for 60"					Mask ID: **DBR Si Etch**

	UCSB/Technics	UCSB Technics prestrip						
	UCSB	Etch Silicon	**Overetch to clear Si from sidewalls using isotropic etch** **TiO2 can be etched from the fields as well.**					Etch **All** Angstroms of Silicon + TiO2, sidewall of ridge must be clear of silicon. Must do large OverEtch, preferrably isotropic to clear ridge sidewalls

Ridge Dielectric									
		SiN Deposition	UCSB Nitride process, index should be between 1.9 and 2.2 **(note: we already have some left over nitride on top of the ridges before this deposition)**					Thickness Spec.	2200 Angstroms +/- 200 A
	UCSB							n Value Spec.	
								Actual Thickness (Å)	
								Actual n Value	
	BCB	2.1 um final thickness	+					Mask ID: **BCB (negative polarity)**	
	Cure BCB		Cure and Descum (must avoid oxygen plasma)??? Do not know what this means.						
	SiN BCB encapsulation	1000 A nitride deposition							

P-Via										
111	UCSB	HMDS	HMDS (Always with positive resist)							
112		Stepper	SPR955CM-1.8, 4KRPM for 30", Bake 90 C for 90", exp = 2.3", focus offset = 0, PEB = 110 C for 90", AZ300MIF dev for 60"					Expose Time (sec)		
	UCSB							Mask: **P-ViA7** Mask Polarity _____B_____		
								Lamp Power (mW/cm^2)		
113	UCSB	PEB	UCSB PEB process							
114	UCSB	Develop	UCSB Develop process							Inspect for complete removal of BCB in P-Via
	UCSB	Etch Nitride	UCSB Nitride wet etch ~ 3300 A, BOE or other HF solution (Sloped Dry etch OK)					Do 30% OE to insure nitride is gone. Ensure any residual TiO2 is removed also.		
	UCSB	Etch InP protection layer	HCl: H3PO4 1:3, etches InP about 1000 A/min, highly selective to InGaAs. Etches layer 27 that is 500 A thick.					Wet etch: Highly selective between InP and InGaAs		
		To insure InP layer removed etch slightly into InGaAs	Etch depth?? Etch Method??							
117	UCSB	Photoresist strip								

P metal pattern - P-metal Deposition + Lift Off									
	UCSB	UCSB Lift off process	Use Lift off process - Last time we used LOR resist, look up notes for which one. We intended to use LOR 2000, but decided on a thicker LOR because we deposited >10K thickness of metal.						Mask ID: **P-metal**
	UCSB	Ebeam P-metal	Ti + Pt +10,000 A Au use standard thickness for liftoff P-metal.						
	UCSB	Lift-off	Solvent Spray lift - off process						
	UCSB/Technics	UCSB Technics Ash	20" 300W Oxygen, 200 mT						

Wafer Thinning Process/N-metal/Anneal									
	UCSB or.. ?	UCSB wafer mounting process	Wafer mounting using wax is available for the CMP at UCSB using the Wafer Bonder; however, detailed specifications indicate use for substrate sizes of 4" - 6", which needs to be addressed with Bill (tool supervisor)						
	UCSB or.. ?	Lapping	Logitech Orbis CMP at UCSB. Lap wafer down to 130 - 150 µm						Target Lapping thickness (µm):
									Actual Wafer thickness (µm):
	UCSB or.. ?	Polishing	Lap wafer down to 120 - 140 µm						Target Polishing thickness (µm):
									Actual Wafer thickness (µm):
		Solvent Clean							
	UCSB or.. ?	Ebeam N-metal	Ni = 60Å Ge = 80Å Au = 800Å Ge = 150Å Ni = 300Å Au = 5000Å						

	UCSB or.. ?	Anneal	RTA 390 C for 1 min			
		Cleaving	See cleaving map on next Sheet. Complete devices have 350 µm pitch. Discrete devices have 175 nm pitch.			Diamond Tip Scribe ok. Due to the wafer orientation, start of scribe on backside is recommended but not required..
		HR coating	Every 3rd column of 3rd cell in each reticle contains complete devices without back DBRs. Intended for HR coating. See below cleaving map			

Appendix B 16XX nm EPI Stack

	Comment	Material	x-start	x-end	xend for all layers	y-start	y-end	z-start	z-end	Repeat	Thickness (Å)	Strain (%)	Dopant	Type	Doping Start (cm-3)	Doping End (cm-3)	Subtotal Thickness (Å)	Layer start depth um for	Layer end Depth um for	Index start	Index End	Changes			
27	Sacrific	InP									500				>1e19										
26		In(x)Ga(	0.5333		0.5333						1224.8		Be	P	3E+19		1224.8	2.5727	2.6952	3.5042	3.5042				
25	InGaAsI	In(x)Ga(	0.8631		0.8631			0.7			612.4		Be	P	2.00E+19		612.4	2.5115	2.5727	3.2317	3.2317	Mod doping			
24		InP									1000		Be	P	1E+19	2.00E+19	1000	2.4115	2.5115	3.1411	3.1214	Mod doping			
23		InP									5124		Be	P	2E+18		5124	1.8991	2.4115	3.1585	3.1585				
22		InP									4286.8		Be	P	5E+17		4286.8	1.4704	1.8991	3.1616	3.1616				
21		InP									50		Be	P	2.00E+18	2.00E+18	50	1.4654	1.4704	3.1585	3.1585	new layer, Mod composition and doping			
20	Etch sto	In(x)Ga(	0.8631		0.8631			0.7		Etch sto	100		Be	P	**5.00E+17**		100	1.4554	1.4654	3.2713	3.2713	Mod thickness and doping			
19		InP									**50**		Be	P	**2.00E+18**	**2.00E+18**	50	1.4504	1.4554	3.1585	3.1585	new layer Mod composition and doping			
18		InP								Etch usi	**600**		Be	P	**5.00E+17**	5E+17	600	1.3904	1.4504	3.1616	3.1616	Mod doping reduced thickness			
17		InP									**50**		Be	P	**3.00E+18**	**3.00E+18**	50	1.3854	1.3904	3.1564	3.1564	New layer			
16	3 InAlGa	In(x)Al(y	0.5251	0.5263	0.5263	0.4749	0.4065			etch 13(	122.5		Be	P	1E+18		122.5	1.3731	1.3854	3.2499	3.2702				
15	3 InAlGa	In(x)Al(y	0.5299	0.5251	0.5251	0.1994	0.4749				122.5		Be	P	5E+17	1E+18	122.5	1.3609	1.3731	3.3706	3.2837				
14	2 InAlGa	In(x)Al(y	0.5299		0.5299	0.1994					898.8		Be	P	1E+18	8E+17	898.8	1.271	1.3609	3.413	3.4134				
13	2 InAlGa	In(x)Al(y	0.5299		0.5299	0.1994				Stop in t	269.5		Be	P	5E+16	1E+18	269.5	1.2441	1.271	3.4148	3.4133				
12	2 InAlGa	In(x)Al(y	0.5299		0.5299	0.1994					36.7		n/a	UID	n/a	n/a	36.7	1.2404	1.2441	3.415	3.415				
11	3 InAlGa	In(x)Al(y	0.5325	0.5299	0.5299	0.0468	0.1994				100		n/a	UID	n/a	n/a	100	1.2304	1.2404	3.5065	3.4512				Implant depth
10	Barrier	In(x)Al(y	0.4341		0.4341	0.2036					49.9	0.665 T	n/a	UID	n/a	n/a	49.9	1.0755	1.0805	3.3858	3.3858				0.2213
9	QW	In(x)Al(y	0.5968		0.5968	0.0442				11	100	0.441 C	n/a	UID	n/a	n/a	1100	1.0655	1.0755	3.581	3.581				
8	Barrier	In(x)Al(y	0.4341		0.4341	0.2036					49.9	0.665 T	n/a	UID	n/a	n/a	548.9	1.0605	1.0655	3.3858	3.3858				
7	3 InAlGa	In(x)Al(y	0.5287	0.5325	0.5325	0.2681	0.0468				150		n/a	UID	n/a	n/a	150	1.0455	1.0605	3.3962	3.5028				
6	2 InAlGa	In(x)Al(y	0.5287		0.5287	0.2683					55		n/a	UID	n/a	n/a	55	1.04	1.0455	3.3682	3.3682				
5	2 InAlGa	In(x)Al(y	0.5287		0.5287	0.2683					100		Si	N	2E+18	5E+16	100	1.03	1.04	3.3604	3.3648				
4	3 InAlGa	In(x)Al(y	0.5251	0.5287	0.5287	0.4749	0.2683				100		Si	N	2E+18		100	1.02	1.03	3.2685	3.3177				
3		In(x)Al(y	0.5251		0.5251	0.4749					100		Si	N	2E+18		100	1.01	1.02	3.2336	3.2336				
2	3 InAlGa	In(x)Al(y	0.5263	0.5251	0.5251	0.4065	0.4749				100		Si	N	2E+18		100	1	1.01	3.2614	3.2456				
1		InP									10000		Si	N	5E+17		10000	0	1	3.1604	3.1604				

Appendix C 16XX nm process traveler

PS20230301

W1: 020552P3FL04

PS20230301

W	W1	W	W	W	W	W			Step	Layer	Process	Details	
2/28	x	x	x	x	x	x	x	x	0	Ridge	Info	Starting material - (1) InP epi wafer	
2/28 NJ-611	x	x	x	x	x	x	x	x	1	Ridge	Drop Gage	Measure the thickness with the drop gage	
2/28 NJ	x	x	x	x	x	x	x	x	2	Ridge	Inspect	Inspect surface for defects. Take photos of any large defects	
3/1 NJ	x	x	x	x	x	x	x	x	3	Ridge	Solvent Clean	1. Acetone - NO ultrasonic 2. ISO - NO ultrasonic 3. N2 Dry	3 min3 min
3/1 NJ-368	x	x	x	x	x	x	x	x	4	Ridge	PECVD2	Recipe: STD Nitride2 Run 10min coat before deposition. Desired thickness = 400 nm	46 min
3/1 NJ	x	x	x	x	x	x	x	x	5	Ridge	Cleave	Cleave wafer into four quarters. Take phone image of cleaved quarters.	
x	3/1 LS	3/1 LS	3/1 LS	3/1 LS	x	x	x	x	6	Ridge	Solvent Clean	1. Acetone - NO ultrasonic 2. ISO - NO ultrasonic	1 min1 min
x	3/1 LS	3/1 LS	3/1 LS	3/1 LS	x	x	x	x	7	Ridge	PR-coat Mesa	Dehydration bake: 115C Coat HMDS: 4000rpm	5 min 30 sec
x	3/1 LS	3/1 LS	3/1 LS	3/1 LS	x	x	x	x	8	Ridge	Inspect	Inspect backside of all wafers. Ensure no PR residue or particles. Repeat Acetone spray as needed. Remove particles with razor blade	
x	3/1 LS	3/1 LS	3/1 LS	3/1 LS	x	x	x	x	9	Ridge	Photo Mesa	Mask Title = NASA project Ridge 1	*Orient wafers as
x	3/1 LS	3/1 LS	3/1 LS	3/1 LS	x	x	x	x	10	Ridge	Develop Mesa	Post exposure bake: 110C 300MIF	90 sec 60 sec
x	3/1 LS	3/1 LS	3/1 LS	3/1 LS	x	x	x	x	11	Ridge	Inspect	Inspect pattern, ensure all PR is fully developed Take pictures of each wafer	
x	3/1 LS	3/1 LS	3/1 LS	3/3 LS	x	x	x	x	12	Ridge	ICP2	Mount wafers with ample oil and bake at 80C 1 min	
x	3/1 LS	3/1 LS	3/1 LS	3/3 LS	x	x	x	x	13	Ridge	Inspect	Inspect for fully etched SiN. Hold if additional etching is needed	
x	3/1 LS	3/1 LS	3/1 LS	3/3 LS	x	x	x	x	14	Ridge	PR strip	NMP @ 80C with NO ultrasonic - clean beaker ISO with NO ultrasonic	2 hr 5 min
x	3/1 LS	3/1 LS	3/1 LS	3/3 LS	x	x	x	x	15	Ridge	Technics	O2 300mT 100W	1 min
x	3/1 LS	3/1 LS	3/1 LS	3/3 LS	x	x	x	x	16	Ridge	Inspect	Inspect pattern, ensure all PR is fully stripped Take pictures of each wafer	
x	3/6 LS 3'42"	3/6 LS 3'4	3/6 LS 3'4		x	x	x	x	17	Ridge	Oxford Cobra	Chamber conditioning required - load a piece of InP material Recipe: InP Ridge	4 min 45 sec, 8 peaks
x	3/6 LS	3/6 LS	3/6 LS		x	x	x	x	18	Ridge	Inspect	Inspect wafer for clean etching	
x	3/7 NJ	3/7 NJ	3/7 NJ		x	x	x	x	19	Ridge	LEXT	Measure etch depth	1.1-1.2 um
x	3/7 NJ	3/7 LS	3/7 LS		x	x	x	x	20	Ridge	Technics	O2 300mT 100W	2 min
x	3/7 LS	3/7 LS	3/7 LS		x	x	x	x	20	Ridge	Acid Etch 1	DI Water - dip to wet surface BHF:DI (1:10) HCl:H3PO4 (1:3)	10 sec1 sec10 sec2 min

28	x	3/7 LS	3/7 LS	3/7 LS		x	x	x	x	21	Ridge	Inspect	Inspect pattern, ensure all PR is fully stripped ~~Take pictures of each wafer~~				
29	x	3/7 NJ	SR 3	SR 3/8		x	x	x	x	22	Ridge	LEXT	Measure etch depth				
30	x	SR 3/8	SR 3	SR 3/8	10	x	x	x	x	23	Implan	PECVD2	Recipe: STD Nitride2	12min45sec			
31	x	3/9 LS	3/9 LS	3/9 LS		x	x	x	x	24	Implan	~~PR-coat Implant~~	Dehydration bake: 115C	5 min	Need 2.5-3um		
32	x	3/9 LS	3/9 LS	3/9 LS		x	x	x	x	25	Implan	~~Photo Develop Implant~~	Mask Title = NASA project Implant 2				
33	x	3/9 LS	3/9 LS	3/9 LS		x	x	x	x	26	Implan		Post exposure bake: 115C	90 sec			
34	x	3/9 LS	3/9 LS	3/9 LS		x	x	x	x	27	Implan	Inspect	Inspect pattern, ensure all PR is fully developed				
35	x	3/9 LS	3/9 LS	3/9 LS		x	x	x	x	28	Implan	Dektak	Dektak features to ensure sufficient PR thickness. Should be >2.5um				
36	x	3/9 N	3/9	3/9 NJ		x	x	x	x	29	Implant	Shipping	Package carefully for shipping for ion implant				
37	x	3/20 NJ	3/20 NJ	3/20 NJ		x	x	x	x	30	Implant	Shipping	Recieve from implant				
38	x	3/20 NJ (in AZ300T)	3/20 NJ (in AZ300	3/20 NJ (in AZ300		x	x	x	x	31	Implant	Solvent Clean	AZ300T @ 80C with NO ultrasonic ISO with NO ultrasonic DI rinse N2 Dry	1hr+ 3 min 2 min			
39	x	3/20 LS	3/20	3/20		x	x	x	x	32	Implan	Inspect	Inspect pattern, ensure all PR is fully developed				
40	x	SR 4/3	5/17 LS			x	x	x	x	33	Window	PR-coat Mesa	Dehydration bake: 115C Coat HMDS: 4000rpm Bake: 100C Coat SPR955CM-1.8: 3000rpm Bake: 90C	5 min 30 sec 1 min 30 sec 90 sec			
41	x	SR 4/3	5/17			x	x	x	x	34	Window	Inspect	Inspect backside of all wafers. Ensure no PR residue or particles. Repeat				
42	x	SR 4/3	5/17			x	x	x	x	35	Window	~~Photo Develop~~ Mesa	Mask Title = Protective				
43	x	SR 4/3	5/17			x	x	x	x	36	Window		Post exposure bake: 110C	90 sec			
44	x	SR 4/3	5/17			x	x	x	x	37	Window	Inspect	Inspect pattern, ensure all PR is fully developed				
45	x	SR 4/7	SR 5/1			x	x	x	x	38	Window	ICP2	Mount wafers with ample oil and bake at 80C 1 min				
46	x	NJ 4/7	5/18			x	x	x	x	39	Window	Inspect	Inspect for fully etched SiN. Hold if additional etching is needed				
47		SR 4/11	5/18			x	x	x	x	40	Window	PR strip	NMP @ 80C with NO ultrasonic - clean beaker	2 hr			
48	x	LS 4/14	LS 5/23			x	x	x	x	41	Window	Tencor/Dektak	Measure and record step from top of ridge to open epi area.				
49		LS 4/14	LS 5/2			x	x	x	x	41	Window	Technics	O2 descum 300mT 100W. Repeat as necessary to remove residue.	1min			
50	x	NJ 4/14	LS 5/23			x	x	x	x	42	Window	LEXT	Take 100x scan of ridge.				
51	x	LS 4/14	LS 5/2			x	x	x	x	42	Window	Etch	DI Water - dip to wet surface	10 sec1 sec2 min			
	x	LS 4/14	LS 5/23			x	x	x	x	43	Window						

52	x	LS 4/14	LS 5/23			x	x	x	x	43	Window	Etch	etch InGaAsP 100 AWet transferH3PO4: H2O2 : H2O (3:1:5)DI Rinse	40 sec2 min			
53	x	LS 4/14	LS 5/23			x	x	x	x	44	Window	InP Etch	InP = 700 A wet transfer H3PO4:HCl (3:1) DI rinse	10 sec20sec2 min			
54	x	LS 4/14 1.728	LS 5/23 Tencor 1.7 33um			x	x	x	x	43	Window	Tencor/Dektak	Measure and record step from top of ridge to open epi area. Should have increase by ~80nm				
55	x	SR 4/17	SR 5/25			x	x	x	x	44	Grating	Solvent Clean	1. Acetone - NO ultrasonic 2. ISO - NO ultrasonic 3. N2 Dry	2 min2 min			
56	x	SR 4/17	SR 5/25			x	x	x	x	45	Grating	PECVD2	Recipe: STD SiO2	1 min 21 sec			
57	x	NJ				x	x	x	x	46	Grating	HOLD	Give to Bill for coat, write and develop				
58	x	5/17 HI				x	x	x	x	47	Grating	Inspect	Take photos of gratings				
59	x	5/17 HI				x	x	x	x	48	Grating	SLR	CF4 SiO2 grating Etch FlowCHF3/CF4 flow= 20/60, RF1=50, RF2=500, Pressure = 5	12 sec	0.8 selectivity		
60	x	5/17 HI				x	x	x	x	49	Grating	Inspect	Take photos of gratings				
61	x	5/17 LS				x	x	x	x	50	Grating	Acid Etch	HCl:DI 1:10 for 20s, Rinse in DI 60s, Blow Dry. Load immediately into Cobra				
62	x	5/17 LS				x	x	x	x	51	Grating	Cobra etch	PS Std InP Grating Etch - Cl2/CH4/H2/Ar 20C20 C: 2mT, Bias/ICP power=150/100W, H2/	4 min			
63	x	5/17 LS				x	x	x	x	52	Grating	Technics	O2 descum 300mT 100W	1 min			
64	x	5/18 MJM				x	x	x	x	53	Grating	AFM	Measure etch depth - target = 130 nm into epi		35 nm		
65	x	5/22 NJ	x	x	x	x	x	x	x	54	Grating	Acid Etch	HCl:DI 1:10 for 40s, Rinse in DI 60s, Blow Dry. Load immediately into Cobra				
66	x	5/22 LS	x	x	x	x	x	x	x	55	Grating	Cobra etch	PS Std InP Grating Etch - Cl2/CH4/H2/Ar 20C20 C: 2mT, Bias/ICP power=150/100W, H2/	2 min			
67	x		x	x	x	x	x	x	x	56	Grating	AFM	Measure etch depth - target = 130 nm into epi				
68	x		x	x	x	x	x	x	x	54	Grating	SLR	CF4 SiO2 grating Etch FlowCHF3/CF4 flow= 20/60, RF1=50, RF2=500, Pressure = 5	12 sec	0.8 selectivity		
69	x		x	x	x	x	x	x	x	55	Grating	PR strip	NMP @ 80C with NO ultrasonic - clean beaker ISO with NO ultrasonic DI rinse N2 Dry	15min 5 min 2 min			
70										56	Grating	Technics	O2 descum 300mT 100W	1 min			
71	x		x	x	x	x	x	x	x	57	Grating	PECVD2	Recipe: STD SiO2	1 min 21 sec			
72	x		x	x	x	x	x	x	x	58	Grating	HOLD	Give to Bill for coat, write and develop				

73	x		x	x	x	x	x	x	x	59	Gratin	SLR	CF4 SiO2 grating Etch FlowCHF3/CF4 flow= 20/60, RF1=50, RF2=500, Pressure = 5	12 sec	
74	x		x	x	x	x	x	x	x	60	Gratin	SEM	Inspect gratings in SEM to confirm dimesions		
75	x		x	x	x	x	x	x	x	61	Gratin	Cobra etch	Recipe: PS Std InP Grating Etch - Cl2/CH4/H2/Ar 20C20 C: 2mT, Bias/ICP power=150/10	4'48"	
76	x		x	x	x	x	x	x	x	62	Gratin	AFM	Measure etch depth		
77	x	x	2/20	x	x	x	x	x	x	63	Gratin	Wet Etch	Buffered HF: DI 1:10 - etch until all SiN/SiO2 hardmask material is removedDI Rinse	~~24 sec1 min~~	
78	x	x	2/21	x	x	x	x	x	x	64	Gratin	AFM	Measure etch depth - target = 130 nm into epi	100 nm deep w/o SiO2 mask	
79	x	x	x	x	x	x	x	x	x	64	~~SOG~~	~~Coat~~	~~Spin SOG 4000rpmBake 200 deg C~~	~~30 sec1min~~	
80	x	x	x	x	x	x	x	x	x	65	~~SOG~~	~~RTA~~	~~Anneal 400 C~~		
81	x	x	x	x	x	x	x	x	x	66	~~SOG~~	~~Woolam~~	~~Measure SOG thickness and index on Si monitor piece. Save raw data scan~~		
82	x	x	x	x	x	x	x	x	x	67	~~SOG~~	~~SLR~~	~~Insert SOG etch recipe. Use laser monitor~~		
83	x		x	x	x	x	x	x	x	67	Si	Solvent Clean	NMP @ 80C with NO ultrasonic - clean beaker	15min	
84			x	x	x	x	x	x	x	68	Si	Technics	O2 descum 300mT 100W	3min	
85	x		x	x	x	x	x	x	x	68	Si	ALD	Recipe: CH3-TDMAT+H2O-300C		
86	x		x	x	x	x	x	x	x	69	Si	Woolam	Measure thickness and index of TiO2. Save raw data scan		
87	x		x	x	x	x	x	x	x	70	Si	Si	Dehydration bake: 115C	5 min	
88	x		x	x	x	x	x	x	x	71	Si	Inspect	Inspect backside of all wafers. Ensure no PR residue or particles. Repeat		
89	x		x	x	x	x	x	x	x	72	Si	Photo Si	Mask Title = NASA project DBR Silicon Etched4		
90	x		x	x	x	x	x	x	x	73	Si	Si	Post exposure bake: 110C	1 min	
91	x		x	x	x	x	x	x	x	74	Si	Inspect	Inspect pattern, ensure all PR is fully developed		
92			x							75	Si	Technics	300mT/100W	30 sec	
93	x		x	x	x	x	x	x	x	76	Si	#1	Include a glass slide with deposition.		
94	x		x	x	x	x	x	x	x	77	Si	Liftoff	NMP @ 80C with NO ultrasonic	1+hr/Overni	
95	x		x	x	x	x	x	x	x	78	Si	Technics	300mT/100W	4min	
96	x	x	x	x	x	x	x	x	x	78	Si	Inspect	Ensure all PR is fully removed		
97	x	x	x	x	x	x	x	x	x	79	Si	Inspect	Inspect pattern, ensure all PR is fully removed		
98	x	x	x	x	x	x		x	x	80	BCB	PECVD2	Recipe: STD Nitride		
99	x	x	x	x	x	x		x	x	81	BCB	Woolam	Measure thickness and index of SiN. Save raw data scan		
100	x	x	x	x	x			x	x	82	BCB	Coat	Dehydration bake: 115C	5 min	
101	x	x	x	x	x			x	x	83	BCB	Inspect	Inspect backside of all wafers. Ensure no PR residue or particles. Repeat		
102	x	x	x	x	x			x	x	84	BCB	BCB	Mask Title = BCB		
103	x	x	x	x	x			x	x	85	BCB	BCB	Post exposure bake: 50 C	30 sec	
104	x	x	x	x	x			x	x	86	BCB	Inspect	Inspect pattern, ensure all PR is fully developed		
105	x	x	x	x	x			x	x	87	BCB	PR Strip	NMP 80C, 2hr+, Sonicate on high for 10min		
106	x	x	x	x	x			x	x	88	BCB	PEII	O2 plasma, 300mTorr/100W for 20"		
107	x	x	x	x	x			x	x	89	BCB	Acid dip	HCl:DI 1:10 for 60s, Rinse in DI 60s, Blow Dry		
108	x	x	x	x	x	x		x	x	90	BCB	Coat	Dehydration bake: 115C	5 min	
109	x	x	x	x	x	x		x	x	91	BCB	Inspect	Inspect backside of all wafers. Ensure no PR residue or particles. Repeat		
110	x	x	x	x	x	x		x	x	92	BCB	BCB	Mask Title = BCB		
111	x	x	x	x	x	x		x	x	93	BCB	BCB	Post exposure bake: 55 C	30 sec	

111	x	x	x	x	x	x		x	x	93	BCB	BCB	Post exposure bake: 55 C	30 sec	
112	x	x	x	x	x	x		x	x	94	BCB	Inspect	Inspect pattern, ensure all PR is fully developed		
113	x	x	x	x	x			x	x	95	BCB	PR Strip	NMP 80C, 2hr+, Sonicate on high for 10min		
114	x	x	x	x	x			x	x	96	BCB	PEII	O2 plasma, 300mTorr/100W for 20"		
115	x	x	x	x	x			x	x	97	BCB	Acid dip	HCl:DI 1:10 for 60s, Rinse in DI 60s, Blow Dry		
116	x	x	x	x	x	x		x	x	98	BCB	Coat	Dehydration bake: 115C	5 min	
117	x	x	x	x	x	x		x	x	99	BCB	Inspect	Inspect backside of all wafers. Ensure no PR residue or particles. Repeat		
118	x	x	x	x	x	x		x	x	100	BCB	BCB	Mask Title = BCB		
119	x	x	x	x	x	x		x	x	101	BCB	Develop BCB	Post exposure bake: 55 C DS2100 (BCB developer) T1100 rinse N2 Dry	30 sec 60 sec 30sec	
120	x	x	x	x	x	x		x	x	102	BCB	Inspect	Inspect pattern, ensure all PR is fully developed		
121	x	x	x	x	x			x	x	103	BCB	PR Strip	NMP 80C, 2hr+, Sonicate on high for 10min		
122	x	x	x	x	x			x	x	104	BCB	PEII	O2 plasma, 300mTorr/100W for 20"		
123	x	x	x	x	x			x	x	105	BCB	Acid dip	HCl:DI 1:10 for 60s, Rinse in DI 60s, Blow Dry		
124	x	x	x	x	x	x		x	x	106	BCB	Coat	Dehydration bake: 115C	5 min	
125	x	x	x	x	x	x		x	x	107	BCB	Inspect	Inspect backside of all wafers. Ensure no PR residue or particles. Repeat		
126	x	x	x	x	x	x		x	x	108	BCB	BCB	Mask Title = BCB		
127	x	x	x	x	x	x		x	x	109	BCB	Develop BCB	Post exposure bake: 55 C, 30sec Immediately do puddle development using POLOS spinner program "7" (step1: 500rpm-10sec; step2:4000rpm-400rpm/s-60sec): Apply DS2100 BCB developer on quarter, wait 60sec, then run program "7" While it is spinning @500rpm/10sec gently apply DS2100 (drop by drop in the center of the quarter)-Rinsing step (first part of recipe 7 described above) Spin dry at 4000rpm/60sec (second part of recipe 7)	30 sec	
128	x	x	x	x	x	x		x	x	110	BCB	Inspect	Inspect pattern, ensure all PR is fully developed		
129	x	x	x	x	x	x	x	x	x	###	BCB	Bake/Cure Oven	Cure BCB - need recipe		
130	x	x	x	x	x	x	x	x	x	95	BCB	PECVD2	Recipe: STD Nitride		
131	x	x	x	x	x	x	x	x	x	96	BCB	Woolam	Measure thickness and index of SiN. Save raw data scan		
132	x	x	x	x	x	x	x	x	x	97	P	Solvent Clean	1. Acetone - NO ultrasonic	10 min10 min	
133	x	x	x	x	x	x	x	x	x	98	P	PR Coat P Cont	Dehydration bake: 115C	5 min	Update?
134	x	x	x	x	x	x	x	x	x	99	P	Inspect	Inspect backside of all wafers. Ensure no PR residue or particles. Repeat		
135	x	x	x	x	x	x	x	x	x	100	P	Photo P Cont	Mask Title = NASA project DBR Nitride 3		name
136	x	x	x	x	x	x	x	x	x	101	P	Develop P Cont	Post exposure bake: 110C	90 sec	
137	x	x	x	x	x	x	x	x	x	102	P	Inspect	Inspect pattern, ensure all PR is fully developed		
138	x	x	x	x	x	x	x	x	x	103	P	SLR	Insert SiN etch recipe. Use laser monitor if possible		
139	x	x	x	x	x	x	x	x	x	104	P	Inspect	Inspect pattern, ensure all SiN is fully etched		
140	x	x	x	x	x	x	x	x	x	105	P	InP Etch	InP = 500 A	10 sec30 sec2 min	

141	x	x	x	x	x	x	x	x	x	106	P	Inspect	Inspect pattern, ensure all InP is fully etched		
142	x	x	x	x	x	x	x	x	x	107	P	Solvent Clean	1. Acetone - NO ultrasonic	10 min10 min	
143	x	x	x	x	x	x	x	x	x	108	P	Inspect	Inspect pattern, take photos of every wafer.		
144	x	x	x	x	x	x	x	x	x	109	Pads	Solvent Clean	1. Acetone - NO ultrasonic	10 min10 min	
145	x	x	x	x	x	x	x	x	x	110	Pads	PR Coat P Cont	Dehydration bake: 115C	5 min	Update?
146	x	x	x	x	x	x	x	x	x	111	Pads	Inspect	Inspect backside of all wafers. Ensure no PR residue or particles. Repeat		
147	x	x	x	x	x	x	x	x	x	112	Pads	Photo P Cont	Mask Title = NASA project DBR Nitride 3		name
148	x	x	x	x	x	x	x	x	x	113	Pads	Develop P Cont	Post exposure bake: 110C	90 sec	
149	x	x	x	x	x	x	x	x	x	114	Pads	Inspect	Inspect pattern, ensure all PR is fully developed		
150	x	x	x	x	x	x	x	x	x	115	Pads	Technics	O2 300mT 100W	1 min	
151	x	x	x	x	x	x	x	x	x	116	Pads	EBeam #4	Pump to: 3e-6		Need stack
152	x	x	x	x	x	x	x	x	x	117	Pads	Liftoff	NMP @ 80C with NO ultrasonic - clean beaker	2 hr	
153	x	x	x	x	x	x	x	x	x	118	Pads	Inspect	Inspect pattern, ensure all PR is fully developed		
154	x	x	x	x	x	x	x	x	x	119	Pads	Shipping	Package carefully for shipping		
155															

.